

REPORT DOCUMENTATION PAGEForm Approved
OMB NO. 0704-0188

Public Reporting burden for this collection of information is estimated to average 1 hour per response, including the time for reviewing instructions, searching existing data sources, gathering and maintaining the data needed, and completing and reviewing the collection of information. Send comment regarding this burden estimate or any other aspect of this collection of information, including suggestions for reducing this burden, to Washington Headquarters Services, Directorate for Information Operations and Reports, 1215 Jefferson Davis Highway, Suite 1204, Arlington, VA 22202-4302, and to the Office of Management and Budget, Paperwork Reduction Project (0704-0188), Washington, DC 20503.

1. AGENCY USE ONLY (Leave Blank)

2. REPORT DATE

3. REPORT TYPE AND DATES COVERED
Final 22/Sept/97 - 21/Sept/00

4. TITLE AND SUBTITLE

Spin-Polarized Transport in Mesoscopic Devices

5. FUNDING NUMBERS

DAAG55-97-1-0401

6. AUTHOR(S)

Lydia L. Sohn

7. PERFORMING ORGANIZATION NAME(S) AND ADDRESS(ES)

Dept. of Physics, Princeton University
Princeton, NJ 085448. PERFORMING ORGANIZATION
REPORT NUMBER

9. SPONSORING / MONITORING AGENCY NAME(S) AND ADDRESS(ES)

U. S. Army Research Office
P.O. Box 12211
Research Triangle Park, NC 27709-221110. SPONSORING / MONITORING
AGENCY REPORT NUMBER37270-EL-YIP
.2

11. SUPPLEMENTARY NOTES

The views, opinions and/or findings contained in this report are those of the author(s) and should not be construed as an official Department of the Army position, policy or decision, unless so designated by other documentation.

12 a. DISTRIBUTION / AVAILABILITY STATEMENT

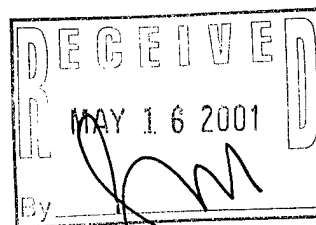
Approved for public release; distribution unlimited.

12 b. DISTRIBUTION CODE

13. ABSTRACT (Maximum 200 words)

We have fabricated 2-3 nm radius aluminum nanoparticles as evidenced by distinct Coulomb Blockade steps in the linear conductance. We have fit these Coulomb Blockade steps to a theoretical model based on the Orthodox Theory of single electron tunneling in order to determine the size and junction characteristics of these nanoparticles. Using the same fabrication technique, we have produced 2-3 nm radius 0.01% iron in copper nanoparticles. By investigating these dilute magnetic alloy nanoparticles, we intended to verify the results of Thimm et al. concerning the complex interplay between spin-polarized tunneling and finite-size effects in a "Kondo box."

20010607 060



14. SUBJECT TERMS

15. NUMBER OF PAGES

16. PRICE CODE

FINAL REPORT
Spin-Polarized Transport in Mesoscopic Devices
DAAG55-97-1-0401

Lydia L. Sohn
Dept. of Physics, Princeton University

TABLE OF CONTENTS

	SECTION/PAGE NUMBER
Table of Contents	A-1
Statement of Disclosure Preference (ARO Form 52 or 52A)	NA
Project Abstract	C-1
Project Description (Technical Proposal)	D-1 - D-13
Biographical Sketch	E-1 - E-2
Bibliography	D - 8
Current and Pending Support	NA
Facilities, Equipment, and Other Resources	NA
Proposal Budget	NA
Contract Facilities Capital Cost of Money (DD Form 1861)(Commercial Organizations only)	NA
Appendices	K-1
List Appendix Items: H. J. Lynch's Princeton University Senior Thesis	

PROJECT ABSTRACT

The Project Abstract shall include a statement of objectives, methods to be employed, and the significance of the proposed activity to the advancement of knowledge or education. Avoid use of the first person to complete this summary. DO NOT EXCEED ONE PAGE. The abstract should be suitable for release under the Freedom of Information Act, 5 U.S.C. 552, as amended.

We have fabricated 2-3 nm radius aluminum nanoparticles as evidenced by distinct Coulomb Blockade steps in the linear conductance. We have fit these Coulomb Blockade steps to a theoretical model based on the Orthodox Theory of single electron tunneling in order to determine the size and junction characteristics of these nanoparticles. Using the same fabrication technique, we have produced 2-3 nm radius 0.01% iron in copper nanoparticles. By investigating these dilute magnetic alloy nanoparticles, we intended to verify the results of Thimm et al. concerning the complex interplay between spin-polarized tunneling and finite-size effects in a "Kondo box."

PROJECT DESCRIPTION

Although the electron-transport properties of metals have been well known and studied for nearly a century, it is only recently that technological advances in nanostructures have allowed researchers to investigate the breakdown of the bulk properties of metals at the mesoscopic length scale (≤ 100 nm). In fact, advances in both atomic-scale imaging and nanofabrication now permit experimentalists to fabricate and, in turn, investigate systems in which discrete electronic states may be distinguished and single electrons counted. One such system of recent interest is that of ultrasmall metallic grains (size ~ 10 nm in diameter). This particular system has discrete, observable energy levels at low temperatures which lend to dramatic consequences for the superconducting, magnetic, and optical properties of the metallic grains [1]. These effects are exemplified in the work of Ralph *et al.* [1,3 - 5] in which the superconducting properties of ultrasmall grains of aluminum (Al) were examined and were shown to display even-odd effects due to superconducting pairing interactions. Here we extend the technology developed by Ralph *et al.* by doping copper nanoparticles with iron atoms in order to investigate the Kondo effect. By scaling down the sample size to the nanometer regime, several unprobed questions may be answered, such as how the Kondo effect is affected by discrete energy levels and what role interimpurity interactions play in conduction through doped metallic grains. The work described below was performed by Heather J. Lynch, a Princeton physics undergraduate (Class of 2000), and has won *the American Physical Society LeRoy Apker Award 2001* for the best undergraduate thesis in the nation. A copy of Lynch's thesis is enclosed.

Recently, Thimm *et. al.* [2] have theoretically investigated the Kondo effect in a doped ultrasmall metallic grain. As is well known, the Kondo effect arises in dilute magnetic alloys and involves the interaction between the magnetic moment of the impurity and the conduction band electrons of the host metal [6, 7]. Although the Kondo effect in bulk samples has been studied experimentally for over sixty years, Thimm *et. al.* answer the question: What happens to the Kondo effect if the impurity resides in an ultrasmall metallic grain? In the case of this Kondo box system, the unpaired spin of the magnetic impurity couples to conduction band electrons with a discrete density of states. Thimm *et. al.* have predicted that for grains with mean level spacing $\Delta > k_B T_K$, where T_K is the characteristic Kondo temperature for the alloy, the temperature dependence of the differential conductance will be measurably affected in a way that will show evidence of the interplay between the Kondo effect and the finite size effects in the grain [2].

Our experiment is most easily described by the circuit diagram in Figure 1. Using fabrication steps discussed below we fabricate a metallic nanoparticle with a radius r (2-5 nm) and self-capacitance C_{self} . On each side of the nanoparticle is an oxide tunnel junction with capacitance C and resistance R . On the other side of these oxide tunnel junctions are two thick metallic layers which serve as electrical leads to the nanoparticle.

The Kondo system we have chosen to investigate is a 0.01% iron in copper alloy. This iron-copper system is ideal because the Kondo temperature is ~ 10 K. A spherical nanoparticle with mean level spacing $\Delta = 10k_B$ has a 3 nm radius, which is approximately the size nanoparticle we expect to fabricate using the steps outlined below. Using a 0.01% alloy, we expect to get 1-10 magnetic atoms in each nanoparticle. Unlike

most other nanoparticle systems of this kind, we have a mixed metal system in which we have aluminum leads and a copper-iron nanoparticle. We use the aluminum leads in order to have aluminum oxide tunnel junctions which have been well characterized in similar nanoparticle systems [1].

The fabrication of the samples follows closely the technique employed by Ralph *et. al.* [1,2-5] to do single-electron tunneling spectroscopy on metallic nanoparticles. The steps involved in the fabrication are illustrated in Figures 2 and 3. The first stage of the process is to create a low-stress, free standing membrane which serves as the substrate for the nanoparticle fabrication (see Figure 2). As a first step, a 50 nm thick layer of LPCVD low-stress Si_3N_4 is deposited on both sides of a standard 3" diameter, 15 mil thick, Si[111] wafer. A $5\text{ mm} \times 5\text{ mm}$ square window is defined on the Si_3N_4 wafer using photolithography. The native silicon oxide layer and the Si_3N_4 layers on the silicon wafer is removed using a CHF_3 reactive ion etch (RIE) so as to expose the silicon wafer within the photolithographically-defined square. The wafer is then etched in a 30% KOH solution at 80-85° C for approximately 2.5 hours. The anisotropic chemical etch leaves $500\text{ }\mu\text{m} \times 500\text{ }\mu\text{m}$ free-standing silicon nitride membrane windows. We next prepare a bilayer of electron-beam resist (PMMA/MMA 10% by weight and 1.5% 950K PMMA). Using electron-beam lithography, a hole ~40 nm in diameter is created in the bilayer of resist. Using another CHF_3 RIE etch, this 40 nm diameter hole is transformed into a bowl-shaped formation which just breaks through the bottom of the membrane, leaving an opening in the membrane which is ~ 4 nm in diameter. The device is fabricated in this bowl-shaped structure using a series of metal evaporations (see Figure 3). Onto the bowl side of the wafer we evaporate 1000 Å of aluminum; which fills the bowl and

provides some stability to the sample. The sample is then oxidized in 50 mT of pure O₂ for 2 minutes. This creates a thin oxide layer at the opening of the bowl. On the other side of the sample, we evaporate ~20 Å of a 0.01% iron in copper alloy. This layer forms islands on the surface of the membrane. The device is successful if one of the islands forms under the opening in the membrane. In the next step we deposit a very thin 15 Å layer of aluminum onto the islands and oxidize in 50 mT of pure O₂ for 2 minutes as before. Ideally, the oxidation is timed precisely so that all the aluminum, and none of the copper nanoparticle, has been oxidized. We have, in effect, deposited a 15 Å layer of insulating Al₂O₃. Finally, we evaporate another 1000 Å of aluminum to form the second lead of the nanoparticle.

The two 1000 Å aluminum layers serve as macroscopic contact pads for measurement of the samples. The 5 mm × 5 mm × 0.4 mm device is sandwiched between two copper plates that are affixed to two teflon triangles screwed together. Using two wires attached to each copper plate we make a standard four-point measurement across our sample. To sweep over a range of voltages, we use a synthesized function generator (Stanford Research Systems Model DS345) which produces a 250 mV amplitude triangle wave. The voltage across the sample is measured using a preamplifier (Princeton Applied Research Model 113) via a multimeter (Hewlett Packard 34401A). The current through the sample is passed through a current preamplifier (Ithaco 1211) and on to another Hewlett Packard multimeter for measurement.

To gain an understanding of the nanoparticle sizes, we fabricated a series of pure aluminum particles. The I-V curve, taken at 4.2 K, of one of these nanoparticle samples

is shown in Figure 4. As shown, there are a series of steps — representing the Coulomb Staircase — in the I-V characteristics. The steps are 57 ± 8 mV in width and show characteristic thermal roundoff. The abrupt dip in current at the end of each step does not appear in the other data; we believe it is an artifact of the data and not our measurement process. For comparison, a computer simulation based on the orthodox theory of single-electron tunneling has been fit to the data [8]. The nanoparticle parameters of the fit are included in the figure. We estimate the nanoparticle radius for this sample to be 2.4 ± 0.2 nm.

While the I-V curve shown in Figure 4 is promising, most of the samples we have fabricated are high-resistance devices ($R > 500$ M Ω). Resistances of this magnitude are too large to be attributed to single charge tunneling. This may be due to a number of problems in the fabrication process. For example, it is possible that we are not etching completely through the nitride window, or that our oxide layers are significantly too thick. It is also likely that many of our high-resistance devices were those in which an island did not form under the opening in the nitride membrane. Other groups have estimated that this will happen only about 20% of the time [9].

Despite these problems, we have fabricated copper-iron nanoparticle devices. Unfortunately, none of the devices fabricated to date have displayed the Coulomb Staircase behavior that is indicative of the single charge tunneling we hope to study. All of the devices fabricated thus far have shown very linear, high resistance, conductance behavior. One example of such behavior is illustrated in Figure 5. In this sample, the resistance is 830 M Ω . There is no obvious nonlinearity, such as a Coulomb Staircase, to indicate that this device is in fact a single nanoparticle. The copper-iron nanoparticles are

much more complicated than the pure aluminum nanoparticles due to the fabrication of the second tunnel junction. In addition to the reasons listed above for the aluminum high resistance devices, it is possible that in making the copper-iron nanoparticles, the thin aluminum layer is not being deposited properly. If the temperature of the sample is not low enough at the time we deposit the 15 Å aluminum layer, the aluminum may form small islands on the surface. This would lead to a very irregular tunnel junction between the nanoparticle and the second lead. If, however, the aluminum is forming islands on the surface, it is possible that no aluminum covers the nanoparticle. Because copper oxidizes more quickly than aluminum, when we oxidize the sample, we may oxidize a very thick copper layer which may lead to the high resistances which we see demonstrated in Figure 5.

In conclusion, we have successfully fabricated 2-3 nm radius nanoparticles of aluminum and are currently in the process of fabricating and measuring 0.01% iron-copper alloy nanoparticles. We believe the mixed system of aluminum leads and a copper-iron nanoparticle is a viable system for the study of the Kondo effect in an ultrasmall metallic grain. In addition to verifying the results of Thimm *et. al.*, this system will allow for the study of other interesting questions. For example, by controllably increasing the iron concentration in the alloy, we may be able to study the effect of interimpurity interactions, and use these interactions to estimate the size dependence of the Kondo effect.

References

1. D. C. Ralph, C. T. Black, and M. Tinkham. Phys. Rev. Lett. **74**, 3241 (1995).
2. W.B. Thimm, J. Kroha, and J. von Delft. Phys. Rev. Lett. **82**, 2143 (1999).
3. D.C. Ralph, C.T. Black, and M. Tinkham. Phys. Rev. Lett. **78**, 4087 (1997).
4. D.G. Salinas, S. Gueron, D.C. Ralph, C.T. Black, and M. Tinkham. Phys. Rev. B **60**, 6137 (1999).
5. D.C. Ralph, C.T. Black, J.M. Hergenrother, J.G. Lu, and M. Tinkham, in *Mesoscopic Phenomena in Solids*, edited by Lydia L. Sohn, Leo P. Kouwenhoven, and Gerd Sch n (Kluwer, Boston, 1997), p. 454.
6. Jun Kondo. Prog. Theo. Phy. **32**, 37 (1964).
7. P.W. Anderson. Phys. Rev. **124**, 41 (1961).
8. D.V. Averin, and K.K. Likharev. *Mesoscopic Phenomena in Solids*, edited by B.L. Al tshuler, P.A. Lee, and R.A. Webb (Elsevier, Amsterdam, 1991).
9. Charles Black. Ph.D. Thesis. Harvard University.

Figure Captions

Figure 1: Voltage-biased double tunnel junction circuit. The two junctions each have a small (~ 1 aF) capacitance, C_1 and C_2 , and a large (~ 20 m Ω) resistance, R_1 and R_2 . The nanoparticle itself has a radius r and a capacitance C_{self} as shown.

Figure 2: Electron-beam lithography stage of nanoparticle fabrication.

Figure 3: Evaporation stage of nanoparticle fabrication.

Figure 4: Linear conductance from an aluminum nanoparticle. Also plotted is a computer simulation of the system (see H. J. Lynch, thesis). The simulation parameters are: $C_1 = 1$ aF, $C_2 = 2.8$ aF, $R_1 = 6$ M Ω , $R_2 = 143$ M Ω , and $T = 4.2$ K.

Figure 5: Linear conductance at $T = 4.2$ K of a copper-iron nanoparticle.

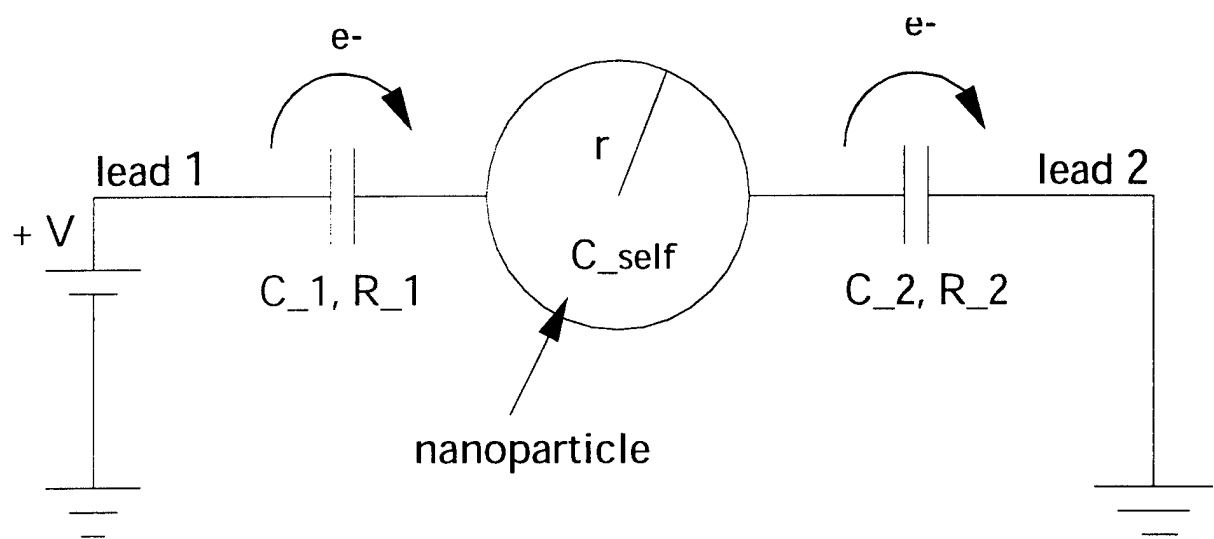


Figure 1

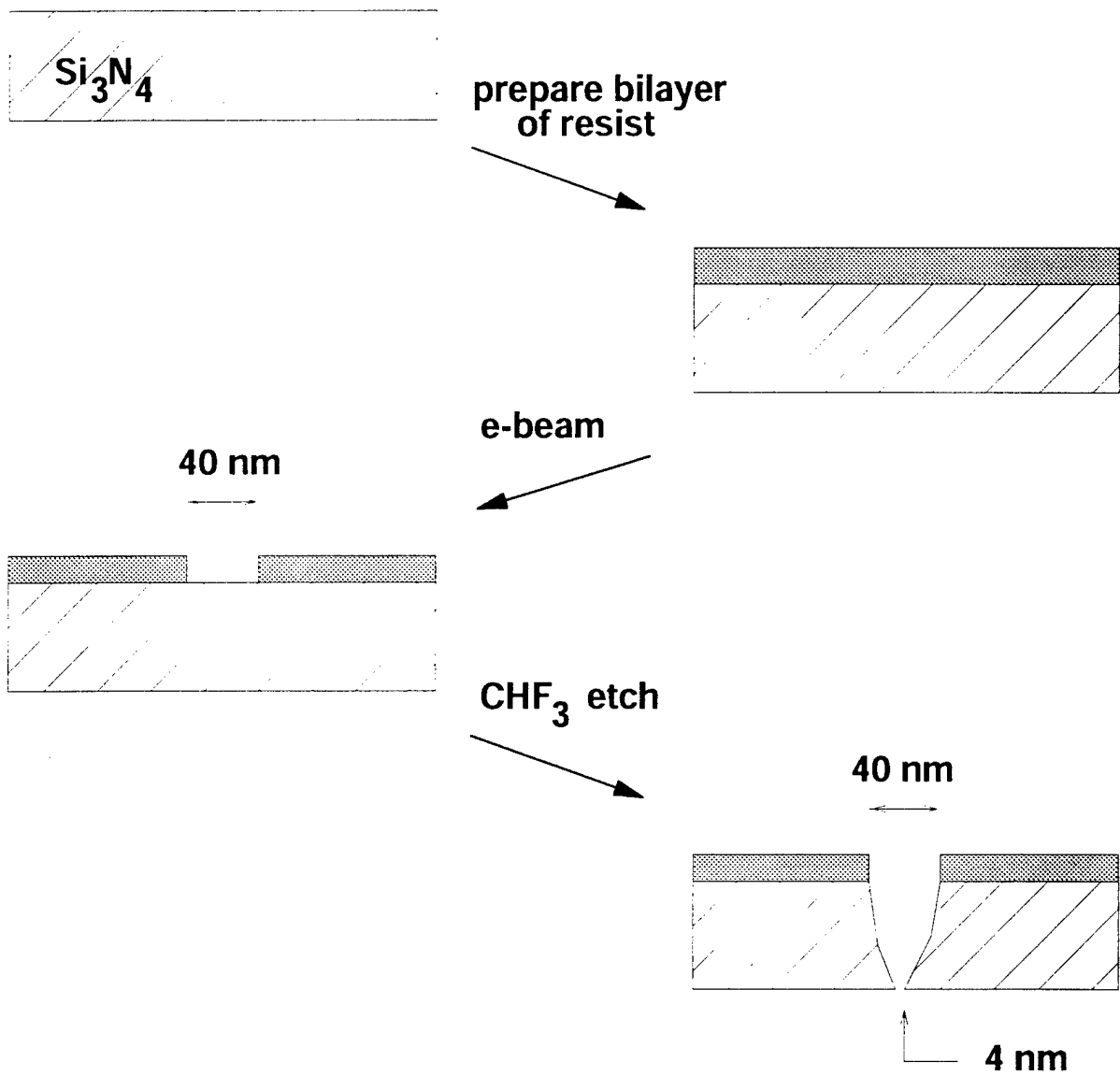
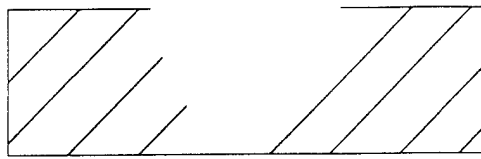
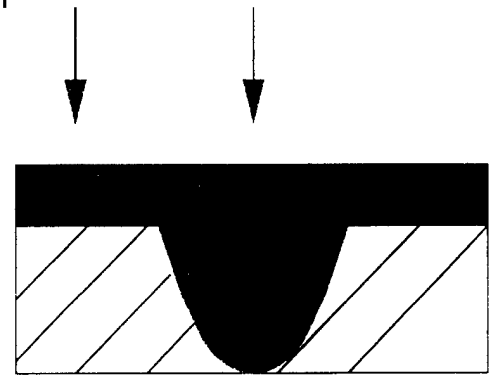
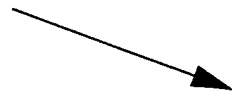


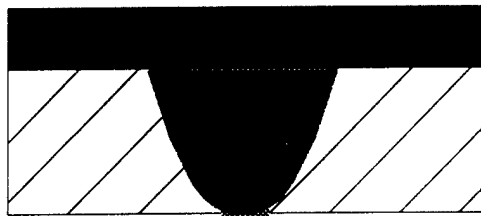
Figure 2



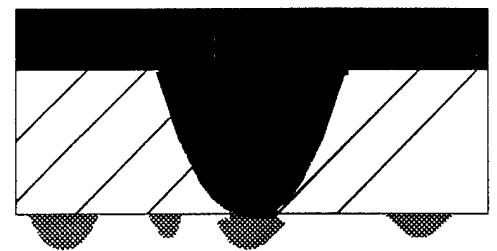
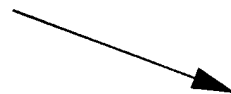
deposit 1000 Å Al



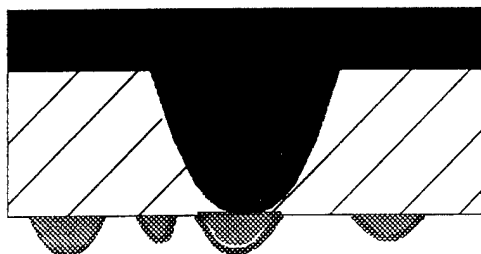
oxidize in O₂



deposit 20 Å Cu[Fe] alloy



oxidize in O₂



deposit 1000 Å Al

Figure 3

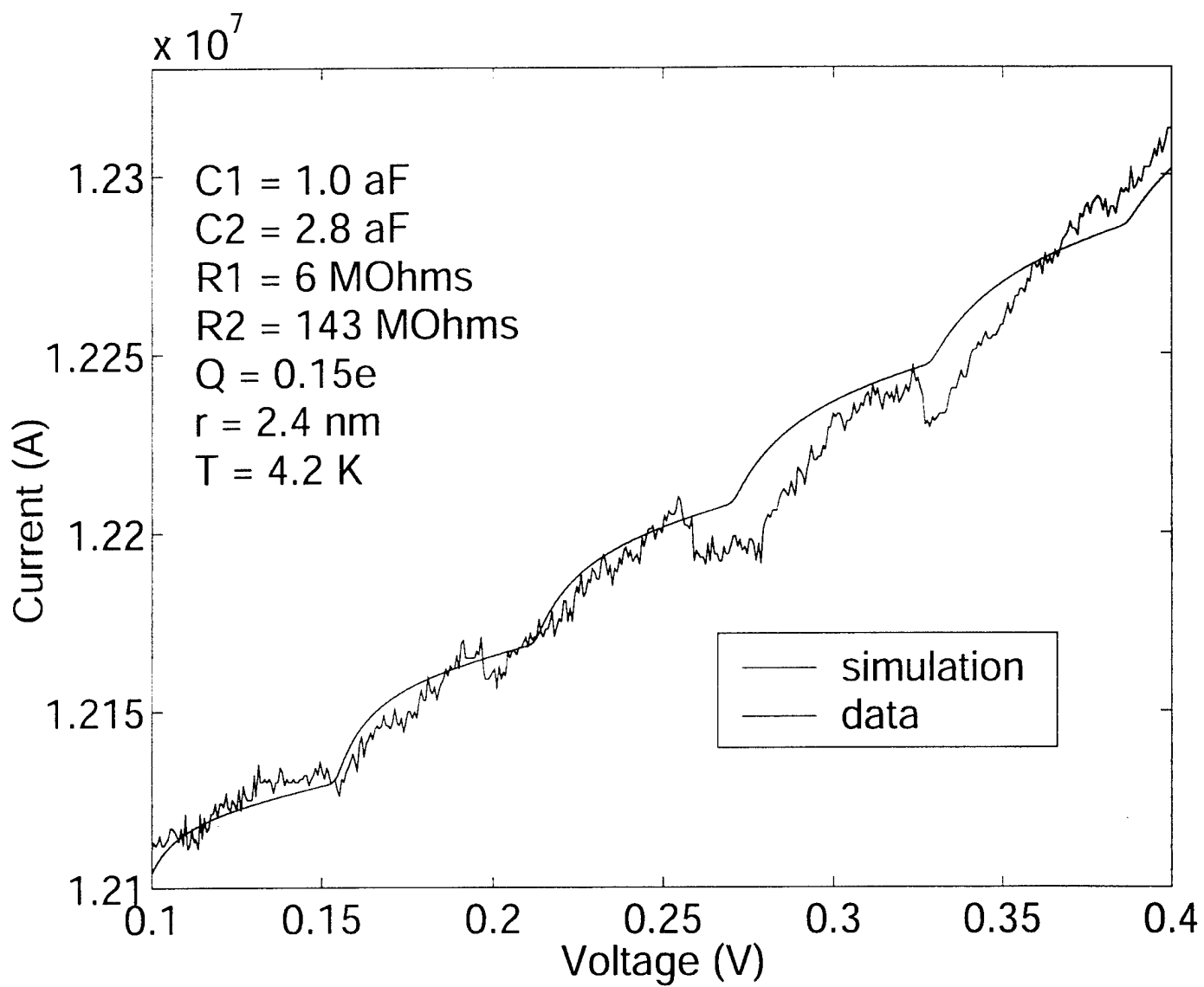
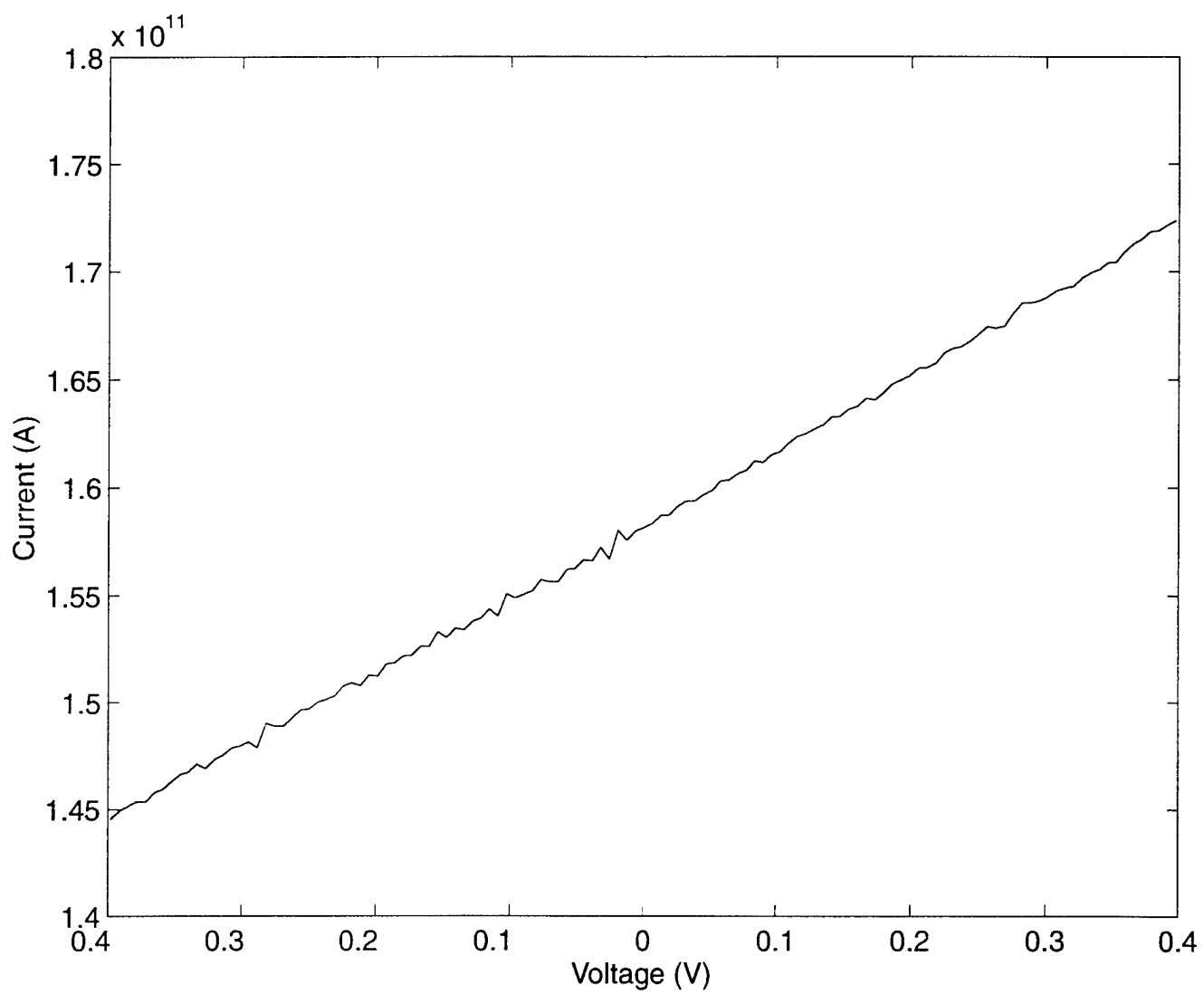


Figure 4



BIOGRAPHICAL SKETCH

Provide the following information for the senior personnel on the project. Begin with the Principal Investigator/Project Director.

DO NOT EXCEED THREE PAGES PER PERSON

NAME: Lydia Lee Sohn

POSITION TITLE: Assistant Professor

RESEARCH AND PROFESSIONAL EXPERIENCE:

Education

- 1988-1992 Ph.D., Dept. of Physics, Harvard University, Cambridge, MA (M. Tinkham, Ph.D. advisor)
1988-1990 A.M., Dept. of Physics, Harvard University, Cambridge, MA
1. A.B., Chemistry & Physics (*magna cum laude*), Harvard University, Cambridge, MA

Positions

- 1995-present Assistant Professor, Dept. of Physics, Princeton University, Princeton, NJ
1993-1995 AT&T Postdoctoral Research Fellow, Semiconductor Physics Research Dept., AT&T Bell Laboratories, Murray Hill, NJ
1. NSF/NATO Postdoctoral Fellow in the group of Prof. dr. J. E. Mooij, Dept. of Applied Physics, Delft University of Technology, Delft, The Netherlands

Honors and Awards

- ☞ American Physical Society Le Roy Apker Award (2001): awarded to Heather J. Lynch for Senior Thesis work performed in the Sohn laboratory at Princeton University
☞ Army Research Office Young Investigator Award (1997-2000)
☞ National Science Foundation Faculty Career Early Development Award (1996-2000)
☞ DuPont Young Professor Award (1996-1999)
☞ AT&T and Lucent Technologies Foundation Award (1996)
☞ Wu Foundation Award (1996)
☞ National Science Foundation-NATO Postdoctoral Fellowship (1992-1993)
☞ Office of Naval Research Predoctoral Fellowship (1988-1991)
☞ Phi Beta Kappa
☞ Rowland Foundation Physics Research Award (1986-1988)
☞ Francis Lee Friedman Physics Award, Harvard-Radcliffe Colleges (1987)
☞ Thomas S. Monfried Scholar, New Jersey Harvard Alumni Assoc. (1985)
☞ Westinghouse Science Talent Search, Honors group (1984)

Patents

- ☞ Nano- and Micro-Electronic Sensors, L. L. Sohn & O. A. Saleh filed for a US Letters Patent, Sept. 2000.
☞ Co-planar Waveguide Used to Determine the Electrical Properties of Biological Solutions, L. Sohn, G. R. Facer, and D. A. Notterman filed for a US Letters Patent Nov. 2000.
☞ Single-Molecule Sequencing, L. L. Sohn and L. F. Landweber filed for a US Letters Patent, Sept. 2000.
☞ Protein & Macromolecular Identification & Separation on a Chip, L. L. Sohn and O. A. Saleh filed for a US Letters Patent, Jan. 2001

THE FOLLOWING ADDITIONAL INFORMATION IS REQUIRED:

- A. List up to 5 publications most closely related to the proposed project and up to 5 other significant publications, including those being printed. Patents, copyrights, or software systems developed may be substituted for publications. Do not include additional list of publications, invited lectures, etc.
 - B. List of persons, other than those cited in the publication list, who have collaborated on a project or a book, article, report or paper within the last 4 years. Negative reports should be indicated.
 - C. Names of graduate and post graduate advisors and advisees.
- The information in B. and C. is used to help identify potential conflicts or bias in the selection of reviewers.

Publications & Patents

1. M. W. Wu, L. P. Kouwenhoven, and L. L. Sohn, *A Single-Molecule DNA Transistor*, in preparation.
2. O. A. Saleh and L. L. Sohn, *Quantitative Sensing of Nanoscale Colloids Using a Microchip Coulter Counter*, submitted to Appl. Phys. Lett. (2001).
3. D. C. G. Klein, L. Gurevich, J. W. Janssen, L. P. Kouwenhoven, J. D. Carbeck, and L. L. Sohn, *Ordered Stretching of Single Molecules of DNA between Microfabricated Polystyrene Lines*, Appl. Phys. Lett. **78**, 2396 (2001).
4. G. R. Facer, D. A. Notterman, and L. L. Sohn, *Dielectric Spectroscopy for Bioanalysis: 40 Hz to 26.5 GHz in a Microfabricated Waveguide*, Appl. Phys. Lett. **78**, 996 (2001).
5. L. L. Sohn, O. A. Saleh, G. R. Facer, A. Beavis, R. S. Allan, and D. A. Notterman, *Capacitance Cytometry: Measuring Biological Cells One-by-One*, Proc. Nat. Acad. Sci. **97**, 10687-10690 (2000).
6. Mingshaw W. Wu and Lydia L. Sohn, *Nanometer-scale Copper Electrodeposition from an On-Chip Source*, IEEE Electron Device Letters **21**, 277-279 (2000).
7. L. L. Sohn, *Quantum Leap for Electronics*, Nature **394**, 131-132 (1998).
8. *Mesoscopic Electron Transport*, NATO ASI Series, Vol. E 345, eds. L. L. Sohn, L. P. Kouwenhoven, and G. Schön (Boston, Kluwer Academic Publishers 1997).
9. Y. Xia, J. McClelland, R. Gupta, D. Qin, X. Zhao, L. L. Sohn, R. Celotta, and G. M. Whitesides, *Replica Molding Using Polymeric Materials: A Practical Step Toward Nanomanufacturing*, Adv. Mater. **9**, 147-149 (1997).

Synergistic Activities

1. Panel reviewer for National Science Foundation: Nanoscale Science and Engineering Initiative grants in the area of "Biosystems at the Nanoscale, February 2001.
2. Panel member on Advanced Research & Experiments in Sensing II, Office of the Under- secretary of Defense for Acquisition & National Academy of Sciences and Engineering, December, 2000 and January, 2001
3. Panel member on Tools for Study of Single Molecules, NIH Bioengineering Consortium Symposium *Nanoscience and Nanotechnology: Shaping Biomedical Research*, June 25-26, 2000.
4. Co-Director, *NATO Advanced Study Institute: Mesoscopic Electron Transport*, Cura ao, The Netherlands Antilles, June 24-July 5, 1996.
5. Radcliffe College Mentor in Science Program (1995-present)

Collaborators & Other Affiliations

Collaborators

1. Dr. Daniel A. Notterman (Dept. of Molecular Biology, Princeton University)
2. Prof. dr. Leo P. Kouwenhoven (Dept. of Applied Physics, Delft University of Technology)
3. Prof. Laura F. Landweber (Dept. of Ecology and Evolutionary Biology, Princeton University)

Graduate and Postdoctoral Advisors

- ¥Prof. M. Tinkham (Dept. of Physics, Harvard University): graduate advisor
¥Prof. dr. J. E. Mooij (Dept. of Applied Physics, Delft University of Technology): postdoctoral advisor
¥Dr. R. L. Willett (Bell Laboratories, Lucent Technologies): postdoctoral advisor

A KONDO BOX: COULOMB BLOCKADE AND
THE KONDO EFFECT IN IRON-DOPED
COPPER NANOPARTICLES

Heather J. Lynch

A SENIOR THESIS SUBMITTED IN PARTIAL FULFILLMENT
OF THE REQUIREMENTS FOR THE DEGREE OF BACHELOR OF ARTS IN PHYSICS
AT PRINCETON UNIVERSITY

APRIL 2000

Princeton University Pledge

This thesis represents my own work in accordance with university regulations.

Abstract

We have fabricated 2-3 nm radius aluminum nanoparticles as evidenced by distinct Coulomb Blockade steps in the linear conductance. We have fit these Coulomb Blockade steps to a theoretical model based on the Orthodox Theory of single electron tunneling [1] in order to determine the size and junction characteristics of these nanoparticles. Using the same fabrication technique, we are in the process of producing 2-3 nm radius 0.01% iron in copper nanoparticles. By investigating these dilute magnetic alloy nanoparticles, we intend to verify the results of Thimm et. al. concerning the complex interplay between spin-polarized tunneling and finite-size effects in a “Kondo box” [2]. In this thesis, we present preliminary data in that regard.

Acknowledgments

I would like to take this opportunity to thank all of the people who have made this project possible. In particular, I would like to thank my advisor, Prof. Lydia Sohn, who has supported me in every way since I first came up with this crazy idea for an experiment. Even from the very beginning, she has trusted me to do as I please in the lab, and for that, she is a braver advisor than I will ever be. I would also like to thank Geoff Facer, who never tired of jumping up from what he was doing to show me why my electronics were not working. If it were not for Geoff, I would probably still be trying to fix some unplugged piece of equipment. Among the rest of the group, I would like to thank Omar Saleh for keeping me an almost well-balanced individual and Mingshaw Wu, who never seemed annoyed when I woke him up at his desk to ask a question.

There have been a number of individuals outside my own group who have been indispensable for advice on this project. I would like to thank Prof. Duncan Haldane, who kindly served as mentor to my understanding of the theory behind this experiment. Also, I would like to thank Prof. Dan Ralph at Cornell University who generously gave of his experience in this field of research.

Finally, I would like to thank my parents for understanding why I never came home on breaks and Matthew Eisaman, for always being there to convince me that switching to theory was not the answer to my experimental difficulties.

Contents

Princeton University Pledge	ii
Abstract	iii
Acknowledgments	iv
List of Figures	1
List of Tables	4
1 Introduction	5
2 Single Electron Tunneling and the Kondo Effect	7
2.1 Calculation of Tunneling Rates	12
2.2 The Kondo Effect	16
2.2.1 The Anderson Zero-Band Width Model	18
2.2.2 The Kondo Effect in a Metallic Grain: A Kondo Box	22
2.2.3 Finding a Kondo System	25
3 Computer Simulation of Single Electron Tunneling	27
3.1 Calculation of Junction Parameters	28
3.2 Simulation of Single Electron Tunneling	30
4 Fabrication and Measurement	36
4.1 Fabrication of Cu[Fe] Nanoparticles	36
4.2 Electron-Transport Measurement	40
4.2.1 Linear Conductance Measurements at 4 K	42
4.2.2 Differential Conductance Measurements at 10-50 K	45

4.3	Data Analysis	45
5	Data and Analysis	47
5.1	Al Nanoparticles	47
5.2	The Cu[Fe] Nanoparticle Kondo Experiment	64
5.2.1	The Cu[Fe] System	64
5.2.2	Thin Film Growth	64
5.2.3	Experimental Data for the Cu[Fe] System	66
6	Conclusion	69
A	CALCULATION OF INTEGRAL BETWEEN EQUATIONS 2.13 AND 2.14	72
B	DERIVATION OF EIGENVALUES FOR THE ZERO-BAND WIDTH MODEL	74
C	COMPUTER SIMULATION CODE	77
D	FABRICATION RECIPES	86
	Bibliography	89

List of Figures

2.1	Voltage-biased double tunnel junction circuit. The two junctions each have a small (~ 1 aF) capacitance, C_1 and C_2 , and a large (~ 20 M Ω) resistance, R_1 and R_2 . The nanoparticle itself has a radius r and a capacitance C_{self} as shown.	9
2.2	Energy schematic of Coulomb Blockade.	11
2.3	The Anderson Zero-Band Width Model. The conduction band electrons have been condensed into a single orbital with wavevector k and the d-orbital electrons of the impurity atom are represented as belonging to orbital d . The two orbitals are related through a mixing term $V_{d,k}$. Adding a second electron to the impurity orbital costs an energy U which arises due to Coulomb repulsion. In our analysis, we consider $U \rightarrow \infty$	19
2.4	Energy schematic illustrating the Kondo singlet and Kondo triplet states.	22
2.5	Energy level diagrams illustrating the difference between the Kondo effect in bulk metal vs. a nanoparticle.	23
2.6	Sketch of a predicted differential conductance measurement for the Kondo box system. The weights W_1 and W_2 are indicated by the shaded areas.	24
2.7	Temperature dependence of weights W_1 and W_2 predicted by Thimm et. al.. The large figure indicates the temperature dependence when the mean level spacing on the nanoparticle $\Delta = 3T_K$. The inset indicates the predicted temperature dependence for $\Delta = T_K$. This figure has been reproduced from Reference [2].	25
3.1	Voltage-biased double tunnel junction circuit,	28

3.2	Plot of I vs. V using both the exact solution (in blue) and the approximate solution (in red) for a nanoparticle with the following parameters: $C_1 = 1$ aF, $C_2 = 3$ aF, $R_1 = 2$ M Ω , $R_2 = 50$ M Ω , $Q_0 = 0.0e$, $r = 3$ nm, $T = 0$	31
3.3	Plot of dI/dV vs. V using both the exact solution (in blue) and the approximate solution (in red) for a nanoparticle with the following parameters: $C_1 = 1$ aF, $C_2 = 3$ aF, $R_1 = 2$ M Ω , $R_2 = 50$ M Ω , $Q_0 = 0.0e$, $r = 3$ nm, $T = 0$. Note that the approximate solution has been offset by 0.5×10^{-11}	31
3.4	Plot of dI/dV vs. V for 0K, 30 K, 60 K, and 90 K. Nanoparticle parameters are the same as in Figures 3.2 and 3.3.	32
3.5	Plot of dI/dV vs. V for $R_2/R_1 = 3, 5, 10$, and 15 . Remaining nanoparticle parameters are the same as in Figures 3.2 and 3.3.	33
3.6	Plot of dI/dV vs. V for $C_2/C_1 = 3, 5, 10$, and 15 . $R_2 = 30$ M Ω and remaining nanoparticle parameters are the same as in Figures 3.2 and 3.3.	34
3.7	Plot of dI/dV vs. V for $Q_0 = 0.0e, 0.1e$, and $0.2e$. Note that e is a negative quantity. Remaining nanoparticle parameters are the same as in Figures 3.2 and 3.3.	35
4.1	Steps involved in the fabrication of Si_3N_4 windows.	38
4.2	Mask design for photolithography.	39
4.3	Electron-beam lithography stage of nanoparticle fabrication.	40
4.4	Evaporation stage of nanoparticle fabrication.	41
4.5	Schematic of sample holder and four-point measurement.	42
4.6	Schematic of insertable cryogenic probe.	43
4.7	Schematic of electronics for the linear conductance measurements. Elements in the primary circuit are connected with solid lines, while the elements used for measurement are connected to the primary circuit via dashed lines.	44

4.8	Schematic of electronics for the differential conductance measurements. Elements in the primary circuit are connected with solid lines, while the elements used for measurement are connected to the primary circuit via dashed lines.	45
5.1	Linear conductance from an aluminum nanoparticle. Also plotted is the computer simulation discussed in Chapter 3. The simulation parameters are: $C_1 = 1.0$ aF, $C_2 = 2.8$ aF, $R_1 = 6$ M Ω , $R_2 = 143$ M Ω , and $T = 4.2$ K.	48
5.2	Linear conductance from an aluminum nanoparticle at 4.2 K. Also plotted is the computer simulation discussed in Chapter 3. The simulation parameters are: $C_1 = 1.0 \times 10^{-3}$ aF, $C_2 = 0.5$ aF, $R_1 = 0.5$ M Ω , $R_2 = 1.0$ M Ω , and $T = 4.2$ K.	50
5.3	Linear conductance at 4K from a high-resistance aluminum nanoparticle.	51
5.4	Linear conductance from an aluminum nanoparticle as the sample warms from 4 K to room temperature. The lowest current curve is the 4 K curve, and the highest current curve is the room temperature curve. All other curves lie linearly between these two temperatures. .	54
5.5	Linear conductance from an aluminum nanoparticle for a range of temperatures from 290 K to 11 K.	55
5.6	$\ln R$ vs. $1/T$ for the data in Table 5.1. The equation of the best-fit line is: $\ln R = 9.52 + 686.6 \frac{1}{T}$	58
5.7	Energy schematic of variable range hopping. The solid and the dashed arrows indicate two possible tunneling events. W and X are the energy difference and spatial distance, respectively, involved in the tunneling event represented by the solid line.	59
5.8	Plot of $\ln(\ln R)$ vs. $\ln T$. The equation of the best-fit line is: $\ln(\ln R) = 4.77 - 0.42 \ln T$	61
5.9	Linear conductance from an aluminum nanoparticle at 4 K.	63
5.10	Typical I-V curve of a Schottky diode.	63
5.11	Island growth on a substrate.	65
5.12	Layer growth on a substrate.	65
5.13	Linear conductance for a copper-iron nanoparticle at 4 K.	67

List of Tables

5.1	Temperature vs. resistance for aluminum nanoparticle sample. The error in the resistance measurement is negligible compared to the error in the temperature.	56
-----	--	----

Introduction

Although the electron-transport properties of metals have been well known and studied for nearly a century, it is only recently that technological advances in nanostructures have allowed researchers to investigate the breakdown of the bulk properties of metals at the mesoscopic length scale (≤ 100 nm). Advances in both atomic-scale imaging and nanofabrication now permit experimentalists to fabricate and, in turn, to investigate systems in which discrete electronic states may be distinguished and single electrons counted. One such system of recent interest is that of ultrasmall metallic grains (size ~ 10 nm in diameter). This particular system has discrete, observable energy levels at low temperatures which lead to dramatic consequences for the superconducting, magnetic, and optical properties of the magnetic grains. Current research into these effects is exemplified in the work of Ralph et. al. [3] [4] [5] [6] [7] [8]. Here we extend the technology developed by Ralph et. al. by doping copper (Cu) nanoparticles with iron (Fe) atoms in order to investigate the Kondo effect. By scaling down the sample size to the nanometer regime, several unprobed questions may be answered, such as how the Kondo effect is affected by discrete energy levels and what role interimpurity interactions play in conduction through doped metallic grains.

Recently, Thimm et. al. [2] have theoretically investigated the Kondo effect in a doped ultrasmall metallic grain. As is well known, the Kondo effect arises in dilute magnetic alloys and involves the interaction between the magnetic moment of the impurity and the conduction band electrons of the host metal [9] [10]. Although the Kondo effect in bulk samples has been studied experimentally for over sixty years, Thimm et. al. investigate what happens to the Kondo effect if the impurity resides in an ultrasmall metallic grain. In the case of this “Kondo box” system, the

unpaired spin of the magnetic impurity couples to conduction band electrons with a discrete density of states. Thimm et. al. have predicted that for grains with mean level spacing $\Delta > k_B T$, where T_K is the characteristic Kondo temperature for the alloy, the temperature dependence of the differential conductance will be measurably affected in a way that will show evidence of the interplay between the Kondo effect and the finite-size effects in the grain [2].

There are a number of different phenomena which interact when a magnetic impurity is introduced into a nanometer-sized metallic grain, including single electron tunneling/Coulomb Blockade, the Kondo effect, and finite-size effects. Each of these phenomena deserve, and have received, careful study¹. The following experiment proposes to investigate the electronic transport properties of an iron-doped copper nanoparticle at low temperatures, a system which requires that all three phenomena be accounted for. In Chapter 2, each of these phenomena will be discussed in the context of this experiment.

In Chapter 3, we present a computer simulation based on the Orthodox Theory of single electron tunneling [1] which calculates the linear conductance of our nanoparticle devices as a function of the relevant parameters of the system. The purpose of this computer simulation is two-fold. First, we use the simulation to understand how the parameters of the devices affect the linear conductance behavior of our samples. Second, we can match our simulation to experimental data in order to extract information about our samples which is inaccessible to direct measurement. In Chapter 4 we discuss the fabrication and the measurement of our nanoparticle devices. In Chapter 5, we present and analyze the data obtained from these nanoparticle devices. Finally, in Chapter 6, we draw conclusions about this experiment and discuss avenues for future research.

¹For single electron tunneling, see References [11] [12]; for the Kondo effect see References [9] [10] [13].

Single Electron Tunneling and the Kondo Effect

In order to understand the theory of single electron tunneling, it is necessary to review the size and temperature regimes that delineate the behavior of tunneling through metallic particles. As the temperature of a metal particle is decreased, the behavior of the current as a function of the applied voltage passes through three distinct regimes depending on both the size and temperature of the particle: These regimes are *bulk metallic*, *charge quantization*, and *energy-level quantization*. For the purpose of this discussion, given our nanoparticle fabrication techniques, we will consider a typical nanoparticle to be 5 nm in radius. The bulk metallic regime ($k_B T > 100$ meV) is most familiar and refers to a system in which current I and voltage V are related through Ohm's law $V = IR$, where R is the resistance of the metal. In the regime of charge quantization ($k_B T \sim 1$ meV), the energy required to overcome Coulomb repulsion in adding a single electron to a nanoparticle is on the order of $k_B T$. When this is the case, the number of electrons on the particle is fixed, or quantized, according to the thermal energy available to it. The last regime, energy-level quantization ($k_B T \sim 0.1$ meV), occurs when the energy difference between adjacent energy levels is on the order of $k_B T$. This can be understood using a simple "particle-in-a-box" picture; as the size of the nanoparticle "box" gets smaller, the energy level spacings become larger. At some point, virtually all of the electrons exist in their ground state because the energy to promote an electron to any higher state is not available.

How small and at what temperatures does a metal particle have to be before it ceases to behave like a bulk metal? To answer this question, we need to calculate the

energy level spacings at the Fermi level. Treating the electrons in the particle as a Fermi gas, we know that the number of electrons with energy $\varepsilon \leq \varepsilon_F$ is given by

$$N(\varepsilon_F) = \left(\frac{V}{3\pi^2} \right) \left(\frac{2m}{\hbar^2} \right)^{3/2} \varepsilon_F^{3/2} \quad (2.1)$$

where ε_F is the Fermi energy, V is the volume of the particle, and m is the mass of the electron.

Differentiating with respect to energy, we obtain the density of states at the Fermi level to be

$$\frac{dN}{d\varepsilon_F} = \frac{3}{2} \left(\frac{V}{3\pi^2} \right) \left(\frac{2m}{\hbar^2} \right)^{3/2} \varepsilon_F^{1/2} \quad (2.2)$$

$$= \frac{3N}{2\varepsilon_F} \quad (2.3)$$

which may be rearranged to give the energy difference δ between two, two-fold degenerate, states at the Fermi energy

$$d\varepsilon \equiv \delta = \left(\frac{2\varepsilon_F}{3N} dN \right) \quad (2.4)$$

$$= \frac{4\varepsilon_F}{3N}. \quad (2.5)$$

The number of electrons, N , on a 5 nm radius particle of Cu is $\sim 6 \times 10^4$. Given this and the Fermi energy of Cu (8.47 eV), we calculate $\delta = 1.9 \times 10^{-4}$ eV or $T \sim 2$ K. Thus, for a 5 nm particle of Cu, the thermal energy $k_B T$ below 2 K is less than the energy level spacing and, therefore, the energy levels must be considered discrete. In this regime of energy-level quantization, current flow through the nanoparticle is no longer Ohmic but is instead dominated by the discreteness of the energy levels.

Between the bulk properties observed at high temperatures and energy-level quantization observed at very low temperatures, a third, unique temperature regime exists in which we observe a phenomenon known as Coulomb Blockade. Coulomb Blockade is best understood by considering the circuit representation of nanoparticle tunneling in Figure 2.1. In Figure 2.1, we have an approximately spherical nanoparticle with radius r connected to metallic leads via two tunnel junctions¹. The voltage difference

¹A tunnel junction is a thin insulating layer (in our experiment, a metal oxide) separating two non-insulating regions which acts like a quantum mechanical tunnel barrier. Electrons cannot conduct through the insulating region, but can pass through the insulating layer via quantum mechanical tunneling.

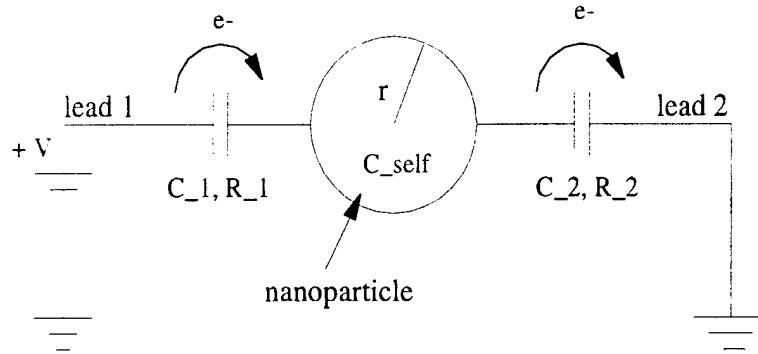


Figure 2.1: Voltage-biased double tunnel junction circuit. The two junctions each have a small (~ 1 aF) capacitance, C_1 and C_2 , and a large (~ 20 M Ω) resistance, R_1 and R_2 . The nanoparticle itself has a radius r and a capacitance C_{self} as shown.

$+V$ between the two leads is one which we apply externally to drive charges across our nanoparticle. The two tunnel junctions and the nanoparticle can be thought of as three capacitors with capacitances C_1 , C_2 , and C_{self} respectively. The two tunnel junctions each have their own resistance R_1 and R_2 .

Despite the quantum mechanical intricacies of tunneling through nanoparticles, the basic features of Coulomb Blockade may be understood in the context of this simple circuit. Basic electrostatics² allows us to write the energy it would take to add a single electron with charge e to an isolated particle with capacitance C (such as the one in Figure 2.1) as

$$E_C = \frac{e^2}{2C} \quad (2.6)$$

where E_C is called the Coulomb Blockade energy. Note that C is the dominant capacitance relating the particle to its environment and is given by

$$\frac{1}{C} = \frac{1}{C_1 + C_2} + \frac{1}{C_{\text{self}}} \quad (2.7)$$

where C_1 and C_2 are the capacitances of lead 1 and lead 2 respectively, and C_{self} is the self-capacitance of the nanoparticle discussed below. In Equation 2.7 we add the capacitances in series, as the electron must tunnel sequentially from lead 1 to the nanoparticle to lead 2. However, we consider the electron on the nanoparticle

²The energy of a capacitor with charge Q is given by $Q^2/2C$.

to couple to the entire environment (in this case, the two leads) simultaneously, and therefore, we add the two junction capacitances in parallel.

The self-capacitance of the nanoparticle may be understood by considering a classical spherical capacitor. If an electron is added to a metallic sphere, the electrons rearrange themselves to reduce the Coulomb repulsion and the capacitance relates the potential of the sphere to the charge placed on it. As the sphere gets smaller, the electrons cannot rearrange themselves as well, and a greater repulsion is felt between the charged sphere and the new electron. At some point, the voltage required to add a single electron to the sphere is measurable, and below this minimum voltage, the tunneling electrons are blocked by Coulomb repulsion - hence “Coulomb Blockade”. In our experiment, the self-capacitance C_{self} of the nanoparticle is defined to be the capacitance of a simple electrostatic capacitor of the same geometry.

We see from Equation 2.7 that if either the junction capacitances or the self-capacitance predominates, the expression for the capacitance of the device may be simplified considerably. In order to do this, we will estimate these two capacitance contributions. If the particles are spherical³ the self-capacitance is simply $C_{self} = 4\pi\epsilon_0 r$, where ϵ_0 is the permittivity of free space and r is the radius of the particle. For a 5 nm radius particle, $C_{self} \sim 0.1$ pF. Using larger tunnel-junctions, the tunnel-junction capacitance per unit area has been estimated at 7.5×10^{-5} fF/nm² [4]. Assuming a spherical nanoparticle with a 5 nm radius⁴, the tunnel-junction capacitances are found to be

$$C_1 = C_2 = 7.5 \times 10^{-5} \frac{1}{2} 4\pi r^2 \quad (2.8)$$

$$= 11.8 \text{ aF} \quad (2.9)$$

where we have taken the area of each tunnel-junction to be that of one hemisphere. We see that the capacitances of the tunnel-junctions are approximately five orders of magnitude smaller than the self-capacitance of the particle. For the purposes of calculating the Coulomb Blockade energy, therefore, we can neglect the self-capacitance of the particle and consider C in Equation 2.6 to be given by

³As seen in Section 4.1, the nanoparticles are actually hemispherical in shape.

⁴As seen in Figure 4.4, the tunnel junctions are formed by oxidizing the outer layer of the nanoparticle, hence, the dependence of the tunnel junction capacitance on the nanoparticle geometry.

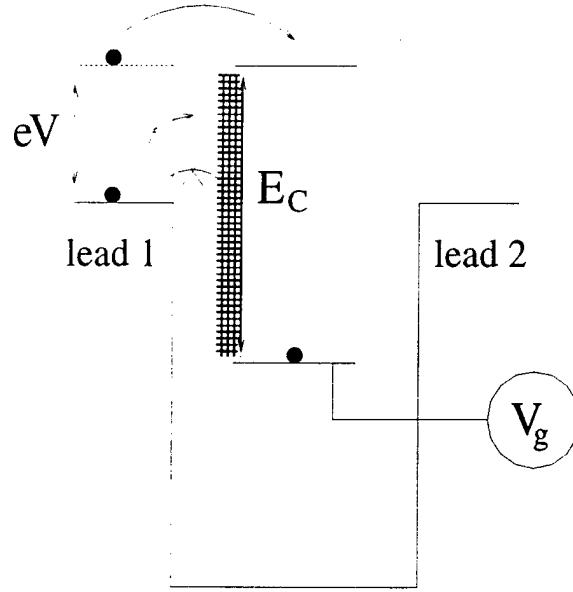


Figure 2.2: Energy schematic of Coulomb Blockade.

$$C = C_1 + C_2. \quad (2.10)$$

Using Equation 2.6, we can calculate the temperature regime in which we expect to see Coulomb Blockade. Plugging $C_1 = C_2 = 11.8$ aF into Equation 2.10, we get that $C = 23.6$ aF, which, plugged into Equation 2.6, yields a Coulomb Blockade energy of 3.4 meV or 39 K. For temperatures below ~ 40 K the energy needed to add a single electron onto the particle⁵ is on the order of $k_B T$. This Coulomb Blockade energy must be accounted for when calculating the tunneling rates through the nanoparticle.

Another way to understand Coulomb Blockade is illustrated in Figure 2.2 in which we schematically represent the energies involved in this experiment. An electron on lead 1 can neither tunnel into the full states that are lower in energy nor into unoccupied states due to the Coulomb Blockade energy E_C . There are two ways in which this Coulomb Blockade may be overcome. First, we can apply a voltage bias across our sample and raise the energy of lead 1 as shown in Figure 2.2 to coincide with the first unoccupied energy level. Electrons in lead 1 are then free to tunnel onto the nanoparticle and off again to lead 2. The second possibility is to change

⁵Local environmental issues, including parasitic capacitances and quantum mechanical fluctuations, drive the effective Coulomb Blockade temperature to much below what is theoretically predicted.

the energy levels of the nanoparticle using a third, gate electrode so that either the electrons in the highest occupied state can tunnel off or so electrons may tunnel into the first unoccupied state. This gate voltage is shown as V_g in Figure 2.2. For our experiments, we do not include a third electrode in our nanoparticle design and instead apply a voltage bias across the leads to overcome Coulomb Blockade.

2.1 Calculation of Tunneling Rates

The tunneling of electrons through the two tunnel-junctions, and hence the current through the nanoparticle, can be calculated as follows [1].

In general, the transition rate $\Gamma_{i \rightarrow f}$ between a discrete initial state i and a final state f lying in a continuum with energy ε is given by Fermi's golden rule,

$$\Gamma_{i \rightarrow f} = \frac{2\pi}{\hbar} |T(\varepsilon)|^2 \rho_f(\varepsilon), \quad (2.11)$$

where $T(\varepsilon)$ is the matrix element coupling the initial and final states and $\rho_f(\varepsilon)$ is the density of states at the energy of the final state ε . In the double-junction system, the expression for the tunneling rate must be modified slightly for two reasons. First, the expression for tunneling must express the fact that both the initial and the final states lie in a continuum. Second, we must account for the occupation probability given by Fermi-Dirac statistics. Before the electron has tunneled, the initial states must be occupied while the final state must be unoccupied. The transition rate $\Gamma_{1 \rightarrow n}$ for the tunneling of electrons from lead 1 with energy ε (as indicated in Figure 2.1) to the nanoparticle with energy $\varepsilon + eV$ is given by

$$\Gamma_{1 \rightarrow n} = \frac{4\pi}{\hbar} \int_{-\infty}^{\infty} |T(\varepsilon)|^2 \rho_1(\varepsilon) f(\varepsilon) \rho_n(\varepsilon + eV) [1 - f(\varepsilon + eV)] d\varepsilon \quad (2.12)$$

where $f(\varepsilon)$ accounts for the occupancy of the initial state at energy ε and $[1 - f(\varepsilon + eV)]$ ensures that the final state at energy $\varepsilon + eV$ is vacant [14]. Over the range of eV (which is very small compared to ε) $\rho_1(\varepsilon)$, $\rho_n(\varepsilon + eV)$ and $|T(\varepsilon)|^2$ may be considered constant, transforming Equation 2.12 into

$$\Gamma_{1 \rightarrow n} = \frac{4\pi}{\hbar} |T(\varepsilon)|^2 \rho_1(\varepsilon) \rho_n(\varepsilon + eV) \int_{-\infty}^{\infty} f(\varepsilon) [1 - f(\varepsilon + eV)] d\varepsilon. \quad (2.13)$$

The integral is evaluated in Appendix A but the solution

$$\Gamma_{1 \rightarrow n} = \frac{4\pi}{\hbar} |T(\varepsilon)|^2 \rho_1(\varepsilon) \rho_n(\varepsilon + eV) \left[\frac{eV}{1 - e^{-eV/kT}} \right] \quad (2.14)$$

yields the tunneling rate for an electron in a lead with energy ε to the nanoparticle with energy $\varepsilon + eV$. In fact, Equation 2.14 is much more general. Let ΔE be the energy difference between the initial and final state, and define a tunneling resistance R , where R is given by $\hbar/(4\pi e^2 \rho_1 \rho_n |T(\varepsilon)|^2)$. The more general expression becomes

$$\Gamma_{1 \rightarrow n}(\Delta E) = \frac{1}{e^2 R} \frac{-\Delta E}{1 - e^{\Delta E/kT}}. \quad (2.15)$$

Note that the change in system energy due to tunneling across the junction in the direction of decreasing bias voltage is $-eV$, and therefore, that the sign in Equation 2.15 corresponds correctly to Equation 2.14.

The definition of the tunneling resistance is motivated by an analogy to Ohm's Law. The total current through the nanoparticle is given by

$$I = e(\Gamma_{1 \rightarrow n} - \Gamma_{n \rightarrow 1}) \quad (2.16)$$

$$= \frac{4\pi e}{\hbar} \rho_1(\varepsilon) \rho_n(\varepsilon + eV) |T(\varepsilon)|^2 \left[\frac{eV}{1 - e^{-eV/kT}} - \frac{eV}{e^{eV/kT} - 1} \right] \quad (2.17)$$

$$= \frac{4\pi}{\hbar} |T(\varepsilon)|^2 \rho_1(\varepsilon) \rho_n(\varepsilon + eV) e^2 V \quad (2.18)$$

which may be rearranged to give the familiar $V = IR$.

Clearly, in order to calculate actual tunneling rates for electrons through a nanoparticle, it is necessary to determine the change in energy ΔE of the system as an electron tunnels on or off the nanoparticle through one of the two leads. The total change in energy involves two terms - one accounts for the increase in energy due to Coulomb repulsion among the electrons and the second accounts for the decrease in energy due to the work done by the voltage source. Using Equation 2.6, we see that the electrostatic energy W_1^+ needed to add an electron to the particle via forward tunneling⁶ through lead 1 is given by

⁶An electron may also be added to the particle via backwards tunneling through lead 2. However, as the temperature $T \rightarrow 0$, tunneling opposite the voltage bias becomes increasingly improbable, and for simplicity, will not be considered in the analysis.

$$W_1^+ = \frac{[(n+1)e + Q_0]^2}{2C_1} - \frac{(ne + Q_0)^2}{2C_1} \quad (2.19)$$

$$= \frac{e^2}{2C_1} \left[(2n+1) + \frac{2Q_0}{e} \right] \quad (2.20)$$

$$= E_C \left[(2n+1) + \frac{2Q_0}{e} \right] \quad (2.21)$$

where the forward tunneling increases the number of electrons on the nanoparticle from $n \rightarrow n+1$, Q_0 is the particle offset charge⁷, C_1 is the capacitance of lead 1, and E_C is the Coulomb blockade energy. The second energy term E_V accounts for the work done by the voltage source and is given by⁸

$$E_V = -e \frac{C_2}{C_\Sigma} V \quad (2.22)$$

where C_2 is the capacitance of lead 2, $C_\Sigma = C_1 + C_2$, and V is the voltage drop between lead 1 and lead 2.

The total energy change ΔE_1^+ due to forward tunneling of a single electron across junction 1 is given by

$$\Delta E_1^+(n \rightarrow n+1) = E_C \left[(2n+1) + \frac{2Q_0}{e} \right] - e \frac{C_2}{C_\Sigma} V. \quad (2.23)$$

Similar reasoning will show that the energy change due to tunneling off of the nanoparticle through lead 2 is given by

$$\Delta E_2^-(n \rightarrow n-1) = E_C \left[(-2n+1) - \frac{2Q_0}{e} \right] - e \frac{C_1}{C_\Sigma} V. \quad (2.24)$$

The general expression for the rate of tunneling either onto (+) or off (-) the particle across either junction (1 or 2) may finally be expressed as

$$\Gamma_{1,2}^\pm(\Delta E_{1,2}^\pm) = \frac{1}{e^2 R} \left[\frac{-\Delta E_{1,2}^\pm}{1 - e^{\Delta E_{1,2}^\pm/kT}} \right]. \quad (2.25)$$

⁷The particle offset charge, which is always some fraction of the electron charge e , arises when the chemical potentials of the nanoparticle and the leads are slightly offset.

⁸When an electron tunnels through junction 1, the potential on the nanoparticle changes. In response to this change in potential, a polarization charge flows in from the voltage source through junction 2. This explains why the energy for current flow through junction 1 depends on C_2 and not C_1 .

Equation 2.25 expresses the tunneling rate for all possible tunneling events for the nanoparticle. The regime under investigation in this experiment is steady-state tunneling, whereby electrons are neither piling up nor being depleted from the nanoparticle. Mathematically, this may be expressed as a set of linear equations

$$\sigma(n-1)\Gamma_{n-1 \rightarrow n} = \sigma(n)\Gamma_{n \rightarrow n-1} \quad (2.26)$$

where $\sigma(n)$ is the probability that the nanoparticle will be occupied by n electrons, and $\Gamma_{n_1 \rightarrow n_2}$ is the tunneling rate between an occupancy of n_1 and n_2 electrons. Equation 2.26 may be rearranged to yield the following recursive relation

$$\sigma(n) = \sigma(n-1) \left(\frac{\Gamma_{n-1 \rightarrow n}}{\Gamma_{n \rightarrow n-1}} \right). \quad (2.27)$$

Finally, we can derive an expression for the current as

$$I = e \sum_n \sigma(n) \left[\Gamma_1^+(n \rightarrow n+1) - \Gamma_1^-(n \rightarrow n-1) \right] \quad (2.28)$$

$$= e \sum_n \sigma(n) \left[\Gamma_2^-(n \rightarrow n-1) - \Gamma_2^+(n \rightarrow n+1) \right] \quad (2.29)$$

where the two equations must be equivalent in steady-state. Using Equations 2.28 and 2.29, along with Equations 2.25 and 2.27, one can theoretically predict the current as a function of the voltage applied across a double-junction nanoparticle device. In order to model our nanoparticle devices, we have written a computer simulation which calculates the linear conductance (I vs. V) through a nanoparticle given the relevant parameters of the device. The results of this simulation are presented in Chapter 3, and in Chapter 5 we compare our simulation to our experimental data in order to calculate key parameters about our fabricated nanoparticles.

The above treatment of tunneling through double-junction nanoparticle devices, in addition to ignoring electron-electron interactions, has failed to mention the most interesting aspect of tunneling through an Fe-doped Cu nanoparticle - the magnetic moment of Fe. Previous experiments involving these nanoparticles have involved pure aluminum (Al) [3] [4] [7] [8] or cobalt (Co) [5] nanoparticles. Although ferromagnetism in nanoparticles has been investigated [5], there have been no published experiments on alloy nanoparticles, in particular, dilute magnetic alloy nanoparticles. The interaction of conduction-band electrons, such as those in the Cu, with the magnetic

moment of the Fe impurity will have a dramatic effect, called the Kondo effect, on the conduction of electrons through the nanoparticle. A brief introduction into the Kondo effect will be presented in order to put the ongoing experiment in the context of its larger goals, that is, observing the Kondo effect in the conduction of electrons through an Fe-doped Cu nanoparticle.

2.2 The Kondo Effect

In order to understand the Kondo effect, which involves the scattering of electrons off a magnetic impurity in a nonmagnetic metal, it is beneficial to take a step back and consider the simplest of all scattering problems, hard sphere scattering. For example, in the scattering of a small marble from a large marble, the potential U at a radius r governing the interaction is a step function, i.e. $U(r < R) = \infty$, $U(r > R) = 0$ where R is the sum of the marble radii. The scattering particles do not interact except at the moment of the collision and neither of the particles are fundamentally changed by the interaction. A more complicated case involves the scattering between two charged particles interacting through a Coulomb potential, for example, Rutherford scattering. The Hamiltonian governing such an interaction is given by

$$H = \frac{1}{2}m\frac{d^2|\vec{r}|}{dt^2} + \frac{zZe^2}{r} \quad (2.30)$$

where ze and Ze are the scattering particle and target charges respectively, m is the mass of the scattering particle and r is the distance between the particles. We see from Equation 2.30 that the interaction depends only on the radial distance between the scattering particles and their charges. Just as in the previous case, neither of the charged particles involved in the interaction are fundamentally changed by the interaction, i.e. each particle retains its charge and mass.

Consider, finally, the case in which the scattering particle and target interact not only through their charge but also through their spin. Allow also the possibility that these spins may actually be flipped by the scattering process such that the outgoing particles are fundamentally changed by the scattering process. This fairly simple extension of the canonical scattering problem results in some very interesting physics. Since the target particle is changed in a given scattering process, the nature

of the *next* scattering event will depend on the previous one. This results in a truly many-bodied problem in which all the scattering particles are coupled through their spin interaction with the target particle. It should be noted that spin has been chosen as just one example through which the particles may couple. A more fundamental statement is that the internal degree of freedom possessed by the scattering center leads to a many-bodied problem, and, as we shall see, to some very interesting and complicated phenomena.

The Kondo effect, one example of such a many-bodied problem, results from the scattering of conduction-band electrons by a magnetic impurity in a nonmagnetic metal. Although there are several ways to understand this problem, the interaction Hamiltonian which most easily relates the Kondo effect with our previous discussion is given by

$$H_{int} = -J \sum_{\alpha, \alpha', k, k'} (\sigma_{\alpha' \alpha} \cdot \mathbf{S}) c_{k' \alpha'}^\dagger c_{k \alpha} \quad (2.31)$$

where $c_{k \alpha}^\dagger$ and $c_{k \alpha}$ are the usual creation and annihilation operators which create and annihilate (respectively) a conduction band electron with wavevector k and spin α [9]. The exchange interaction is mediated through spin, as can be seen by the dot product between $\sigma_{\alpha' \alpha}$, the Pauli spin matrix for the conduction band electrons, and \mathbf{S} , the impurity spin operator. The magnitude of this spin exchange interaction is governed by J , which is the (antiferromagnetic) interaction constant. Physically, the interaction portion of the Kondo Hamiltonian in Equation 2.31 states: The incoming electron with wavevector k and spin α scatters off the magnetic impurity into a state with *different* wavevector k' and spin α' . This interaction depends on both the dot product between the spins of the electron and the impurity and the magnitude of the interaction constant J .

The full solution to this many-bodied problem evaded theorists for almost three decades and will not be discussed here⁹. There is hope, however, for a fairly simple way to understand the essence of the Kondo problem, i.e. an antiferromagnetic interaction between the conduction band electrons and a magnetic impurity will result in a very weakly bound singlet state in which the conduction band electrons condense around the magnetic impurity in the form of a spin-polarized cloud.

⁹For a full review see Reference [13].

2.2.1 The Anderson Zero-Band Width Model

There are several different ways to account for the interactions between a localized moment and delocalized electrons. The Kondo Hamiltonian (part of which is Equation 2.31) is one way of understanding such an interaction. Another, and perhaps more intuitive, representation is given by the Anderson Hamiltonian [10]

$$H = \sum_{\mathbf{k},\sigma} \epsilon_{\mathbf{k}} c_{\mathbf{k},\sigma}^\dagger c_{\mathbf{k},\sigma} + U n_{d,\uparrow} n_{d,\downarrow} + \sum_{\sigma} \epsilon_d c_{d,\sigma}^\dagger c_{d,\sigma} + \sum_{\mathbf{k},\sigma} V_{d,\mathbf{k}} (c_{\mathbf{k},\sigma}^\dagger c_{d,\sigma} + c_{d,\sigma}^\dagger c_{\mathbf{k},\sigma}). \quad (2.32)$$

In the above equation, $c_{\mathbf{k},\sigma}^\dagger$ ($c_{\mathbf{k},\sigma}$) is the creation (annihilation) operator which creates (annihilates) a plane wave in the conduction band with wavevector \mathbf{k} and spin σ . Likewise, $c_{d,\sigma}^\dagger$ ($c_{d,\sigma}$) creates (annihilates) an electron in the d-level of the impurity with spin σ in such a way that $c_{d,\sigma}^\dagger c_{d,\sigma} = n_{d,\sigma}$, the number operator that accounts for the number of electrons in the d-level of the impurity with spin σ . The energy of an electron in the conduction band with wavevector \mathbf{k} and spin σ is $\epsilon_{\mathbf{k},\sigma}$ and the first term in the Hamiltonian sums over all wavevectors \mathbf{k} and spins σ to account for all of the electrons in the conduction band. The energy of an electron in the d-level of the impurity is ϵ_d and the third term in the Hamiltonian sums over all spins σ to account for all the electrons in the impurity orbital. The second term accounts for the Coulomb repulsion that exists between two electrons in the d-orbital of the impurity. The last term is responsible for much of the interesting physics in the system and accounts for the mixing between the magnetic impurity and the conduction band electrons.

Even a very simple model such as the one we will use, the Anderson Zero-Band Width Model, illustrates the basic features of a Kondo system. We consider the conduction band electrons as a single state at the Fermi level. By reducing the conduction band electrons in this way, we map a very complicated many-bodied problem to one with only two orbitals - one orbital for the impurity and one orbital to represent the conduction band electrons of the host metal. For completeness it should be noted that this analysis is predicated on a few physically-motivated assumptions. First, we will assume that $\epsilon_d < \epsilon_{\mathbf{k}}$ but $(\epsilon_d + U) \gg (\epsilon_{\mathbf{k}} - \epsilon_d)$, i.e. although the impurity energy is less than the conduction band energy, the Coulomb repulsion U between two electrons in the impurity orbital prevents, for all practical purposes,

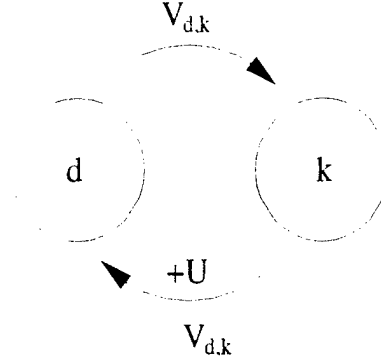


Figure 2.3: The Anderson Zero-Band Width Model. The conduction band electrons have been condensed into a single orbital with wavevector k and the d -orbital electrons of the impurity atom are represented as belonging to orbital d . The two orbitals are related through a mixing term $V_{d,k}$. Adding a second electron to the impurity orbital costs an energy U which arises due to Coulomb repulsion. In our analysis, we consider $U \rightarrow \infty$.

double occupancy of the impurity. Secondly, we will assume that the two orbitals being considered are related through a mixing term $V_{d,k}$ in the Hamiltonian, where $V_{d,k} \ll (\epsilon_k - \epsilon_d)$. The Anderson Zero-Band Width Model is illustrated in Figure 2.3.

Because the Kondo effect arises out of the mixing term $V_{d,k}$, it will be helpful to discuss what the energy level scheme looks like with no mixing term, i.e. $V_{d,k} = 0$. With no interaction between the two orbitals, the ground state system has one electron in each orbital giving a total energy of $\epsilon_k + \epsilon_d$. This ground state is four-fold degenerate due to spin with a spin singlet state

$$|\Phi_S\rangle = (1/\sqrt{2})(c_{k\uparrow}^\dagger c_{d\downarrow}^\dagger - c_{k\downarrow}^\dagger c_{d\uparrow}^\dagger) \quad (2.33)$$

and a spin triplet state

$$|\Phi_T\rangle = \begin{cases} c_{k\uparrow}^\dagger c_{d\uparrow}^\dagger, \\ (1/\sqrt{2})(c_{k\uparrow}^\dagger c_{d\downarrow}^\dagger + c_{k\downarrow}^\dagger c_{d\uparrow}^\dagger), \\ c_{k\downarrow}^\dagger c_{d\downarrow}^\dagger. \end{cases} \quad (2.34)$$

Assuming Coulomb repulsion prevents double occupancy of the impurity orbital, i.e. $U \rightarrow \infty$, the first excited state is one in which both electrons are on the metal orbital. The energy of the first excited state is $2\epsilon_k$ and the wavefunction is

$$|\Phi_{exc}\rangle = c_{k\uparrow}^\dagger c_{k\downarrow}^\dagger. \quad (2.35)$$

The more interesting, and physically realistic, case is one in which $V_{d,\mathbf{k}} \neq 0$. Inspection of Equations 2.33, 2.34, and 2.35 and the Anderson Hamiltonian 2.32 reveals that the first three terms of the Hamiltonian¹⁰ are diagonal with respect to the five possible states. The first and third terms simply add up the contributions to the energies in the conduction band and impurity respectively. These terms in the Hamiltonian do not “mix” the two states, and therefore, they do not have any off-diagonal terms. In order to complete the matrix that will account for the interactions between the five states, we must determine the effect of the fourth term with the mixing potential $V_{d,\mathbf{k}}$ which *does* “mix” states and *will* have off diagonal elements. For clarity, the fourth term is written out explicitly as

$$V_{d,\mathbf{k}}(c_{\mathbf{k},\uparrow}^\dagger c_{d,\uparrow} + c_{d,\uparrow}^\dagger c_{\mathbf{k},\uparrow}) + V_{d,\mathbf{k}}(c_{\mathbf{k},\downarrow}^\dagger c_{d,\downarrow} + c_{d,\downarrow}^\dagger c_{\mathbf{k},\downarrow}). \quad (2.36)$$

The first grouped term can be seen to “move” an electron with spin \uparrow from the impurity to the metal and vice versa, whereas the second grouped term “moves” an electron with spin \downarrow from the impurity to the metal and vice versa. The net effect of the mixing term is to “swap” an electron between the impurity and the metal. Since the three spin triplet states are symmetric under exchange, the mixing potential has no effect on these states. Therefore, the entire Hamiltonian is diagonal with respect to these three states. However, the ground state singlet and the excited states are *not* symmetric under exchange between the impurity and the metal, and these states are affected by the mixing potential. Our 5×5 matrix involving the spin singlet, triplet, and excited state can now be reduced to the following 2×2 matrix

$$\begin{bmatrix} \epsilon_d + \epsilon_{\mathbf{k}} & V\sqrt{2} \\ V\sqrt{2} & 2\epsilon_{\mathbf{k}} \end{bmatrix}. \quad (2.37)$$

The diagonal elements represent the energies of the ground state singlet, with one electron in each orbital, and the excited state, with both electrons on the metal orbital. The off-diagonal terms represent the coupling between the two states by the mixing potential $V_{d,\mathbf{k}}$ and are derived in Appendix B.

¹⁰Actually, the repulsive term is being ignored in the analysis altogether because, in the $U \rightarrow \infty$ limit, we discount the possibility of double occupancy on the impurity.

To determine the effect that this coupling element has on the energies and wavefunctions of the two states under consideration, the above matrix is diagonalized. The eigenvalues of the above matrix are calculated in Appendix B and are found to be $(\epsilon_{exc} + 2V^2/\Delta\epsilon)$ and $(\epsilon_{sing} - 2V^2/\Delta\epsilon)$ where $\epsilon_{exc} = 2\epsilon_k$ and $\epsilon_{sing} = \epsilon_k + \epsilon_d$ and $\Delta\epsilon = \epsilon_k - \epsilon_d$. The eigenvalues represent the new energies of the excited and singlet states respectively. The singlet state has been lowered in energy as a result of its mixing with the excited state, and the excited state has been raised in energy. The singlet state is now no longer degenerate with the triplet state and exists at an energy $2V^2/\Delta\epsilon$ below that of the triplet state.

It is clear that since the singlet state is now of lower energy than the triplet state, if $T \ll T_K$ where $T_K = \left(\frac{2V^2}{k_B\Delta\epsilon}\right)$, only the singlet state will be populated and, since the singlet state has no magnetic moment ($s = 0$), the magnetic impurity will no longer have any magnetic moment¹¹. The magnetic moment is said to be “screened” by the conduction band electrons in the metal. As $T \rightarrow T_K$, the triplet states ($s = 1$) become thermally populated, and a magnetic moment begins to appear on the impurity.

Even with a simple model such as the one used above, it is shown that the mixing between the magnetic moment of the impurity and the conduction band electrons result in the signature features of a Kondo system. As shown in Figure 2.4, there exists a ground state singlet with $s = 0$ that lies some small energy below a low lying triplet state with $s = 1$. The characteristics of the impurity clearly depend on the temperature of the system.

The simple picture of the Kondo effect just presented may be summarized as follows. The Hamiltonian (Equation 2.32) that accounts for interactions between a localized magnetic moment and conduction band electrons contains a mixing potential $V_{d,k}$. This mixing potential splits the four-fold degeneracy of the ground state of the system, resulting in a ground state singlet state and a low-lying triplet state. At appropriately low temperatures, only the ground state is occupied. Physically, the conduction band electrons have condensed into a spin-polarized electron cloud that screens the magnetic moment of the impurity.

¹¹A full analysis will give a Kondo temperature given by $T_K = \frac{D}{k_B} \exp\left(\frac{-\pi|\epsilon_f|}{\nu_f\Gamma}\right)$ where D is half the conduction band width when the band is half full, k_B is the Boltzmann constant, ϵ_f is the Fermi energy, ν_f is the impurity electron degeneracy, and Γ is the width of the impurity electron level due to its coupling with the conduction electrons [15].

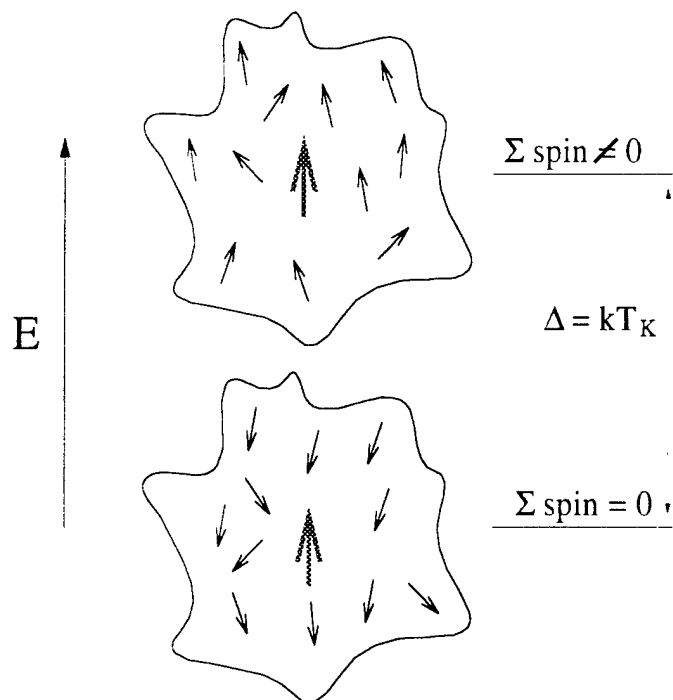


Figure 2.4: Energy schematic illustrating the Kondo singlet and Kondo triplet states.

Unfortunately, the relatively straightforward analysis made possible by the Anderson Zero-Band Width Model stops short of explaining how a ground state “screened” magnetic impurity affects conduction through the metal, or in our experiment, conduction through the Cu[Fe] nanoparticle. There are a number of different ways in which the Kondo effect may manifest itself experimentally, including unusual behavior in the resistivity, conductivity or thermoelectric power. For brevity, we will depart from our more general discussion of the Kondo effect to understand specifically how the Kondo effect may be changed in the confines of a nanoparticle, and how these effects may be probed experimentally.

2.2.2 The Kondo Effect in a Metallic Grain: A Kondo Box

With the introduction and proliferation of nanotechnology in the last few years, one major trend in condensed matter physics has been to contemplate what happens to unusual, but well understood, bulk phenomena on the nanoscale. It is both nontrivial and very interesting to investigate how quantum “particle-in-a-box” confinement interacts with phenomena such as superconductivity and charging effects. In recent

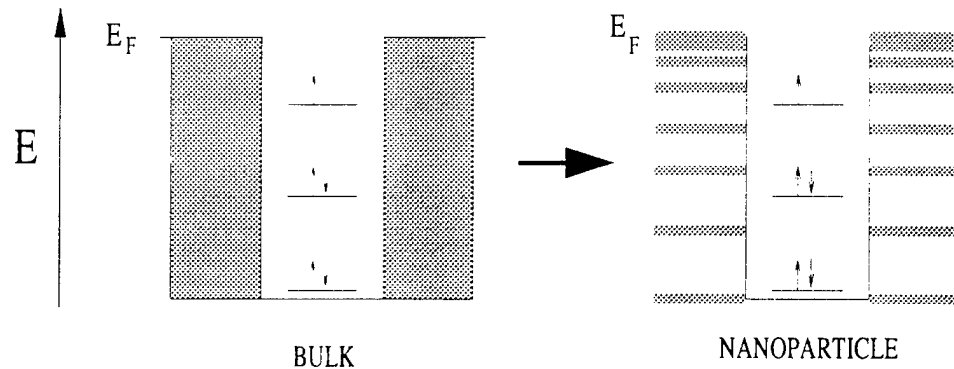


Figure 2.5: Energy level diagrams illustrating the difference between the Kondo effect in bulk metal vs. a nanoparticle.

theoretical work by Thimm, Kroha, and von Delft [2], this work has been extended to the Kondo effect where it is predicted that quantum confinement may affect the conduction of electrons through a doped metallic grain to a degree that is experimentally measurable. The experimental work presented in this thesis seeks to find this predicted effect by investigating the electron transport properties of an iron-doped copper nanoparticle.

Before the results of Reference [2] are discussed, it helps to understand why, in very general terms, the Kondo effect would be different in a nanoparticle as compared to in a bulk sample. Consider the energy diagrams of Figure 2.5. In the left figure we see that the magnetic moment of the impurity (represented as an unpaired electron in the figure) couples to a continuous density-of-states (DOS) in the host metal. In the right figure we see that the DOS in the nanoparticle is discrete, as we would expect from standard “particle-in-a-box” considerations, and therefore the magnetic moment of the impurity couples to a discrete DOS.

The theoretical work of Thimm et. al. [2] may be understood by stepping back and considering the phenomenon of a Fano resonance. Fano calculated that in transitions from an arbitrary initial state to a non-interacting discrete state in resonance with a continuum of states, one sees a distinctively asymmetric peak in the natural line shape due to interference between tunneling to the discrete state and tunneling to the continuum. Madhavan et. al. [16] calculated that for the case of tunneling from an STM tip to a cobalt (Co) atom (which has *interacting* discrete states) on

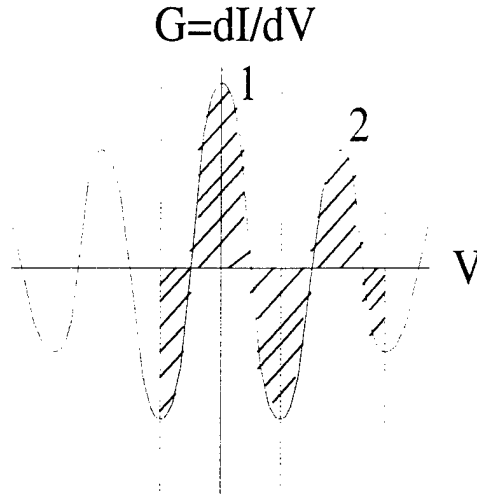


Figure 2.6: Sketch of a predicted differential conductance measurement for the Kondo box system. The weights W_1 and W_2 are indicated by the shaded areas.

a Cu surface (which has a continuum of states), the Fano resonance line shape persists with a width proportional to the Kondo temperature of the system. Thimm et. al. expand this to consider the case where the discrete state is interacting *and* the continuum is actually discrete. This is exactly the case for a magnetic impurity in a nanoparticle. The electrons on the magnetic impurity, which forms the discrete state, interact and the nanoparticle states, which form the “continuum”, are actually discrete. The interference between these two channels of conduction, i.e. from the lead to the nanoparticle and from the lead directly to the impurity, results in the unusual conductance behavior we seek to measure as evidence of the Kondo effect in a nanoparticle. Experimentally, we seek to detect this interference effect by looking at the temperature dependence of the weights, W_1 and W_2 , of the first two conductance peaks. A sketch of the differential conductance (dI/dV vs. V) measurement is illustrated in Figure 2.6. The weights W_1 and W_2 are the areas shaded in Figure 2.6 where the first and second conduction peaks have been indicated with dashed lines. Note that the shaded areas are signed, i.e. the shaded area below the axis must be subtracted from the shaded area above the axis.

We see in Figure 2.7 that for very small nanoparticles, when the mean level spacing $\Delta > k_B T_K$, the weights W_1 and W_2 do not monotonically decrease with decreasing temperature. Instead, W_1 and W_2 bifurcate at $T \sim 0.75 T_K$, with W_1 decreasing sharply and W_2 increasingly sharply. It is this divergence from $T > T_K$ behavior

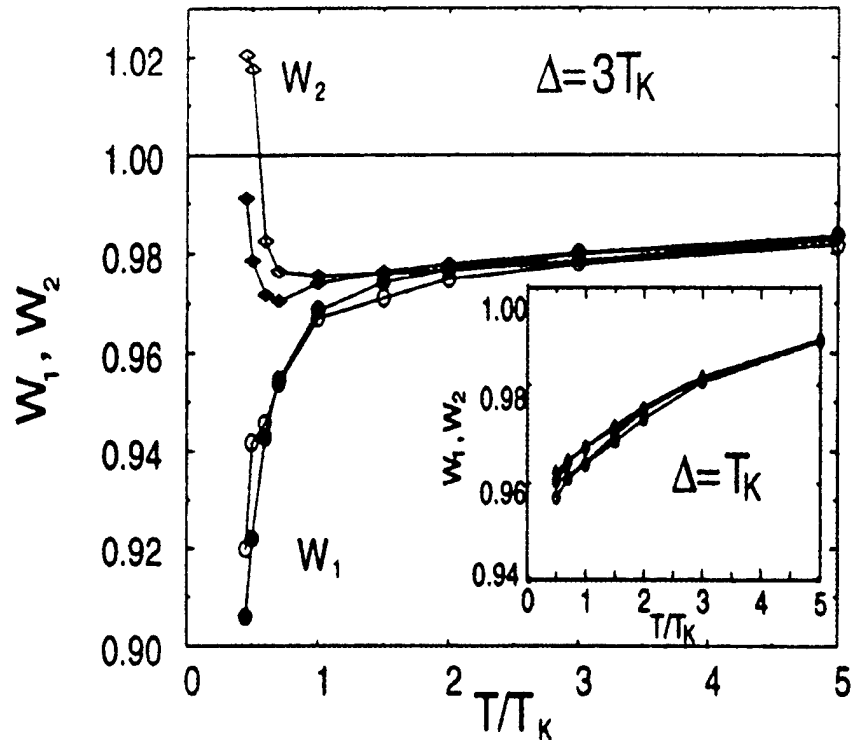


Figure 2.7: Temperature dependence of weights W_1 and W_2 predicted by Thimm et. al.. The large figure indicates the temperature dependence when the mean level spacing on the nanoparticle $\Delta = 3T_K$. The inset indicates the predicted temperature dependence for $\Delta = T_K$. This figure has been reproduced from Reference [2].

that we intend to measure in this experiment.

2.2.3 Finding a Kondo System

We see from the above discussion that the effects we intend to verify experimentally require that the mean level spacing $\Delta > k_B T_K$, where T_K is the Kondo temperature of the system. As each Kondo system has its own characteristic Kondo temperature, it is imperative that the metals chosen for the experiment have a Kondo temperature in the appropriate range for the experiment. As discussed in Section 5.1, we calibrated this experiment by fabricating undoped aluminum nanoparticles, and hence, hoped to find an aluminum alloy to use in the Kondo experiment. We originally considered aluminum doped with chromium atoms. Unfortunately, the resulting aluminum-chromium alloy has an anomalously high Kondo temperature of 1200 K [17]; in fact,

all aluminum alloys have high Kondo temperatures. In order to investigate the Kondo effect in an aluminum-chromium nanoparticle with $\Delta = k_B T_K$, we would have to fabricate a nanoparticle which was 0.7 nm in radius. With our fabrication techniques, we cannot reliably make < 1 nm radius nanoparticles, and hence, could not use the aluminum-chromium system for our experiment.

Instead of an aluminum-chromium alloy, we chose to investigate the Kondo effect using a 0.01% iron in copper alloy. This particular system has two major advantages. The first is that the copper-iron alloy has a Kondo temperature of ~ 10 K [17]. For this system, the appropriate nanoparticle size such that $\Delta = k_B T_K$ is ~ 3 nm, which is well within the capabilities of our fabrication method. Second, the theoretical work discussed in Reference [2] upon which this experiment is based calculates the Kondo effect using the copper-iron system. Although the basic behavior illustrated in Figure 2.7 will appear in any Kondo system, it is convenient to be able to make quantitative, as well as qualitative, comparison with theory.

With a 0.01% concentration of iron atoms in the copper nanoparticle, we estimate that a typical 3 nm radius nanoparticle will have 1-2 magnetic impurities. Ideally, we would like to dope our copper so as to include only a single magnetic impurity on each nanoparticle. In doing so, we eliminate interimpurity interactions. Also, by controllably increasing the number of magnetic impurities per nanoparticle from unity, we can then study the effect of those interimpurity interactions on the transport through the nanoparticle. Unfortunately, with our fabrication techniques, we cannot control the exact number of impurity atoms in each nanoparticle. Nevertheless, at iron concentrations of 0.01%, we can safely ignore interimpurity effects, and by controllably increasing the concentration of iron in our alloy, we can study the role of interimpurity interactions in our experiment.

Computer Simulation of Single Electron Tunneling

From the discussion in Section 2.2.2, we see that the success of this experiment depends on our ability to fabricate nanoparticles in the correct size range. One of the most sensitive electrical methods for determining the size of the nanoparticle is the size and shape of the Coulomb “staircase” that results when charges conduct through a nanoparticle in the charge quantization regime discussed in Chapter 2. In fact, the Coulomb staircase that results from single electron tunneling through a nanoparticle can yield almost all of the important parameters of the nanoparticle system. Referring to Figure 2.1, these are C_1 , R_1 , C_2 , R_2 , and the offset charge Q_0 . Using the junction capacitances and the experimentally determined oxide capacitance of 7.5×10^{-5} fF/nm², we can calculate the nanoparticle size.

The computer simulation discussed in this chapter is beneficial for two distinct reasons. First, it is useful as a tool for understanding how various changes in the junction parameters (i.e. thicker oxide layers, larger particles etc.) will affect the Coulomb Blockade. This will be the topic of this chapter. Second, the simulation provides a way to extract fairly subtle information from experimental data. For instance, in many cases, the data is too noisy to resolve the finer details of the spectra, and therefore most of the junction parameters cannot be determined directly. However, by fitting a simulated curve to the data, one can extract rough estimates of the remaining parameters, leading to a better understanding of the nanoparticles being investigated in this experiment. This will be demonstrated in Chapter 5. It is important to keep in mind that the discussion which follows is a general argument

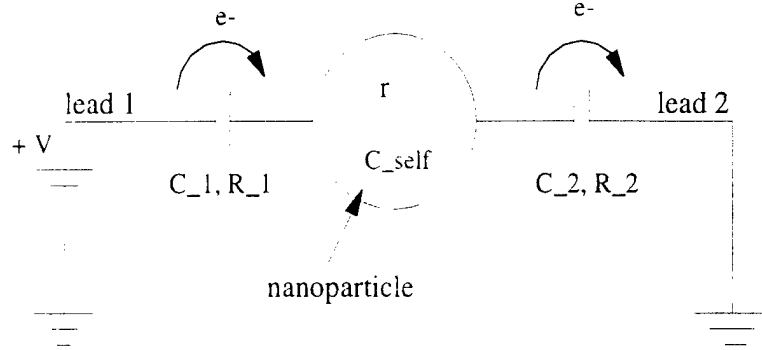


Figure 3.1: Voltage-biased double tunnel junction circuit.

based on single electron tunneling and does not touch upon our primary goal - the Kondo Effect. As we will see, Coulomb Blockade is a useful tool for extracting information about the nanoparticles to be employed in the Kondo effect experiment.

3.1 Calculation of Junction Parameters

Before we can calculate the junction parameters, it will help to review the important quantities in this experiment. Figure 3.1, the circuit diagram introduced in Chapter 2, illustrates the parameters we wish to investigate.

There are seven parameters in this simulation - the tunnel capacitances C_1 and C_2 , the tunnel resistances R_1 and R_2 , the nanoparticle offset charge Q_0 (discussed below), the nanoparticle radius r and the temperature T . Because we disregard the self-capacitance C_{self} relative to the junction capacitances C_1 and C_2 (see the discussion in Chapter 2), the nanoparticle radius does not directly enter into the simulation but is instead extracted using the junction capacitances and Equation 2.8.

Given a plot of I vs. V for a metallic nanoparticle (or simulation), the junction parameters may be determined using the following rules [14] [18]:

1. The mostly easily determined parameter is the capacitance of the larger capacitor, $C_{R>}$, which may be either C_1 or C_2 depending on the geometry of the nanoparticle. The Coulomb staircase can be characterized by a certain periodicity of steps. This characteristic step width, ΔV , is given by

$$\Delta V = \frac{e}{C_{R>}} \quad (3.1)$$

and may be used to calculate $C_{R>}$.

2. An offset charge Q_0 found on the nanoparticle will shift the I vs. V curve in voltage by as much as 40 mV. By measuring the position of the first positive step V_+ and the first negative step V_- in the Coulomb staircase, and using $C_{R>}$ from Rule #1, we can calculate Q_0 by

$$|V_+ - V_-| = 2 \frac{Q_0}{C_{R>}}. \quad (3.2)$$

3. The next most easily determined quantity is the capacitance of the smaller capacitor $C_{R<}$. For every large step in the Coulomb staircase corresponding to tunneling across the $C_{R>}$ junction, there is a (much smaller) step that corresponds to tunneling across the $C_{R<}$ junction. This secondary current step is much smaller than the primary step used in Rule #1, and if the junctions are very asymmetric, i.e. $R_2 C_2 \gg R_1 C_1$, it may be impossible to resolve. See Reference [18] for more complete discussion.
4. Although there is no direct way to determine the junction resistances, R_1 and R_2 , the ratio of the junction resistances is related to the rounding of the Coulomb steps¹. In the limit of $R_2/R_1 \rightarrow \infty$, the step corners are perfectly sharp and connect a perfectly vertical step with a horizontal plateau. For finite R_2/R_1 , the step is not vertical but is characterized by some (steep) slope. This slope can be related to the ratio of the resistances R_2/R_1 . Again, see Reference [18] for more complete discussion.
5. The last piece of information to be gathered from a plot of I vs. V is a rough estimate of $1/R_{>}$. By ignoring the Coulomb staircase altogether, one can obtain a rough estimate of the macroscopic slope of the I vs. V curve. This slope is $1/\Sigma R$, which, for highly asymmetric junctions, is approximately $1/R_{>}$.

¹Rounding in the steps is also related to temperature. Higher temperatures will allow electrons to tunnel through higher resistance junctions, thereby mimicking a lower resistance junction at a lower temperature.

Even a brief examination of these rules will illuminate how difficult it is to obtain nanoparticle parameters by direct examination of the data (especially if the data is less than ideal). However, if even a few of the more obvious parameters can be measured directly, the rest may be determined by fitting a simulation to the data. In Chapter 5, this is the procedure used to analyze the nanoparticles fabricated in this experiment.

Having motivated computer modeling as a tool for analysis, we will introduce the simulation and its various approximations.

3.2 Simulation of Single Electron Tunneling

The theory for single electron tunneling has already been presented in Section 2 and the simulation follows from Equations 2.25, 2.27, and 2.28. An exact solution requires that all possible tunneling events be considered. In order to consider all possible tunneling events, in which the number of electrons $n \rightarrow n \pm 1$, all integer values n from zero to the maximum number energetically allowed on the nanoparticle $\sigma(n_{max})$ must be included in the calculation. This requires that all n simultaneous equations for the occupation probability $\sigma(n)$ in Equation 2.27 be solved and that the resulting $\sigma(n)$ be normalized to a total occupation probability of unity. As we will see, it is a very good approximation to this solution to assume that only those charge states closest to σ_{max} are occupied², i.e.

$$\sigma(n_{max} - 1) + \sigma(n_{max}) = 1. \quad (3.3)$$

This not only makes the code much simpler to write, but it also decreases the computing time. The code for the exact solution is included in Appendix A. In order to compare the approximated solution with the exact solution, we plot both the linear conductance, I vs. V , and the differential conductance, dI/dV vs. V , for a given nanoparticle in Figures 3.2 and 3.3.

The approximated solution is, indeed, an excellent approximation to the exact solution. As may be seen in Figure 3.3, the approximation breaks down only at the onset of each tunneling step. As a new occupation state becomes energetically

²The case of $\sigma(n_{max}) = 1$ is considered in Reference [18].

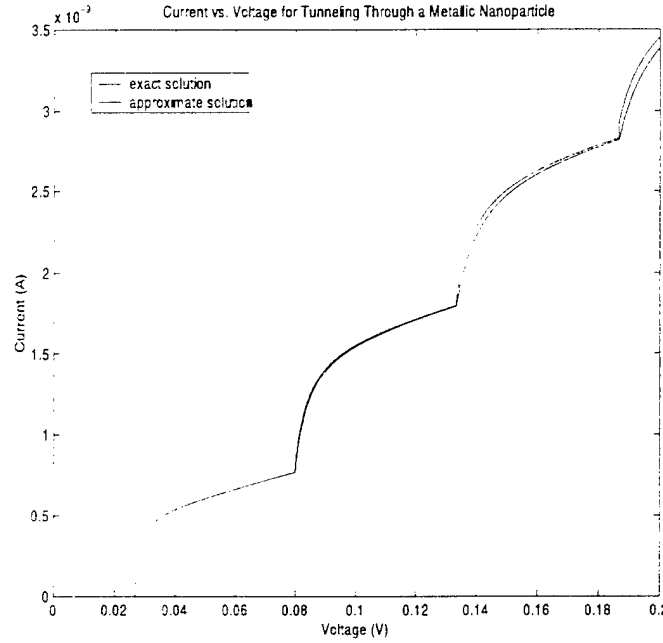


Figure 3.2: Plot of I vs. V using both the exact solution (in blue) and the approximate solution (in red) for a nanoparticle with the following parameters: $C_1 = 1$ aF, $C_2 = 3$ aF, $R_1 = 2$ M Ω , $R_2 = 50$ M Ω , $Q_0 = 0.0e$, $r = 3$ nm, $T = 0$.

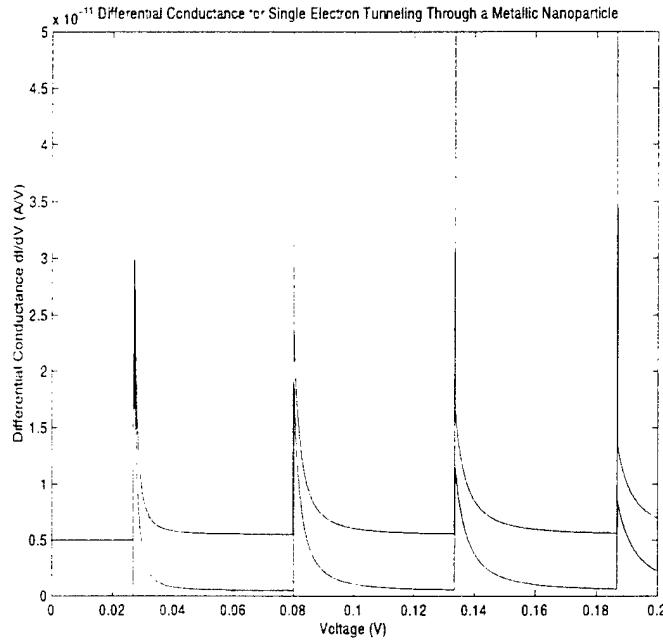


Figure 3.3: Plot of dI/dV vs. V using both the exact solution (in blue) and the approximate solution (in red) for a nanoparticle with the following parameters: $C_1 = 1$ aF, $C_2 = 3$ aF, $R_1 = 2$ M Ω , $R_2 = 50$ M Ω , $Q_0 = 0.0e$, $r = 3$ nm, $T = 0$. Note that the approximate solution has been offset by 0.5×10^{-11} .

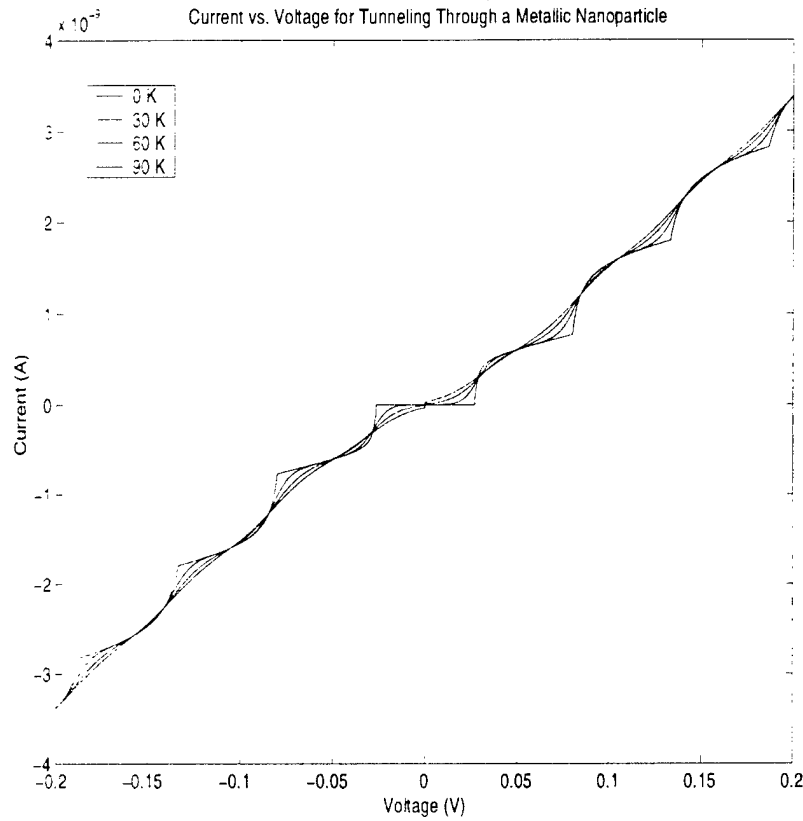


Figure 3.4: Plot of dI/dV vs. V for 0 K, 30 K, 60 K, and 90 K. Nanoparticle parameters are the same as in Figures 3.2 and 3.3.

favorable, Equation 3.3 is momentarily invalidated and the approximation deviates from the exact solution. Despite reasonable agreement between the two solutions, only the exact solution will be used through the rest of this thesis.

There are a number of different parameters of interest which may be explored using this simulation. In particular, we will demonstrate how changing temperature, the ratio of R_2/R_1 , the ratio of C_2/C_1 , and the offset charge Q_0 affect the Coulomb Blockade.

The effect of changing temperature is the easiest to understand. As the temperature is increased, the electrons tunneling on and off the nanoparticle have more energy for the tunneling process. If the temperature is raised above some critical temperature, the electrons will have enough energy to overcome the Coulomb Blockade energy and will tunnel on and off the nanoparticle unaffected by the charge quantization discussed in Chapter 2. We expect, therefore, that as temperature is increased, the

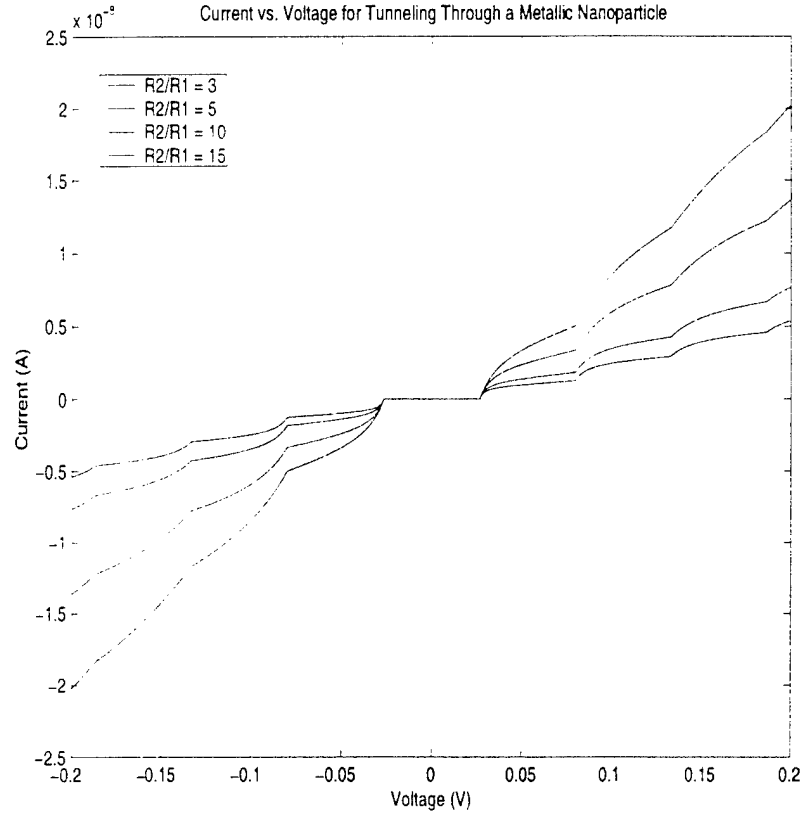


Figure 3.5: Plot of dI/dV vs. V for $R_2/R_1 = 3, 5, 10$, and 15 . Remaining nanoparticle parameters are the same as in Figures 3.2 and 3.3.

Coulomb Blockade steps will become more rounded and less well defined. Eventually, they should disappear altogether. We see that this is in fact the case in Figure 3.4 where we compare the Coulomb staircase for a range of temperatures from 0 K to 90 K.

The next most easily understood parameters in the simulation are the resistances, R_1 and R_2 , of the two tunnel junctions. Since the electron must tunnel through one junction and then through the other in succession, the two resistances add in series. The total resistance is then approximately equal to the larger resistance, R_2 . As can be seen in Figure 3.5, as the resistance of the second junction R_2 is increased relative to R_1 , the total resistance through the nanoparticle increases, and hence the slope of the I vs. V curve decreases. In Figure 3.5, we have plotted the linear conductance for R_2/R_1 ratios of 3, 5, 10, and 15. Clearly, as the ratio of R_2/R_1 increases, the slope (ignoring the Coulomb staircase) decreases.

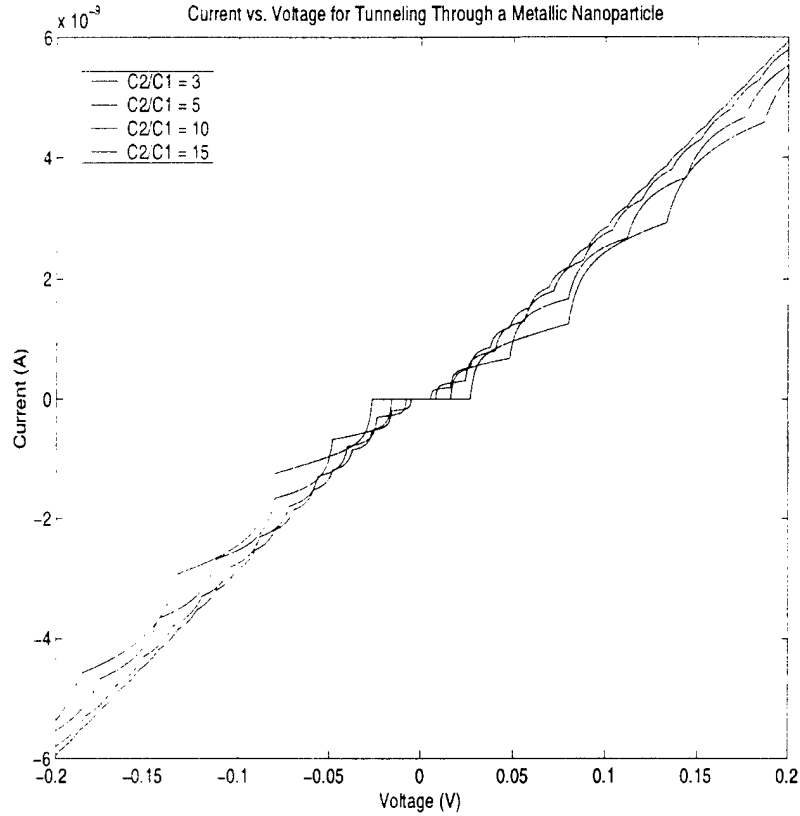


Figure 3.6: Plot of dI/dV vs. V for $C_2/C_1 = 3, 5, 10$, and 15 . $R_2 = 30 \text{ M}\Omega$ and remaining nanoparticle parameters are the same as in Figures 3.2 and 3.3.

In addition to the resistance ratio, it is also interesting to consider what happens as the capacitance ratio C_2/C_1 is varied. As can be seen in Equation 2.22, the change in energy due to the work done by the voltage source as an electron tunnels across the first junction is negative and depends linearly on the capacitance of the second junction C_2 . As C_2 increases relative to C_1 , there is a greater energy incentive for tunneling across the first junction, and as a result, the electrons tunnel onto the nanoparticle at lower voltages. This leads to narrower steps in the Coulomb staircase as the ratio of C_2/C_1 increases. In Figure 3.6, where we have plotted the linear conductance for $C_2/C_1 = 3, 5, 10$, and 15 , we see exactly that phenomenon.

The final parameter of interest is the offset charge Q_0 . The offset charge Q_0 , which was first introduced in Chapter 2, is an electrical charge which results from a slight offset in the nanoparticle and lead chemical potentials and acts like a fractional electron lying on the nanoparticle. Changing the offset charge will shift the entire

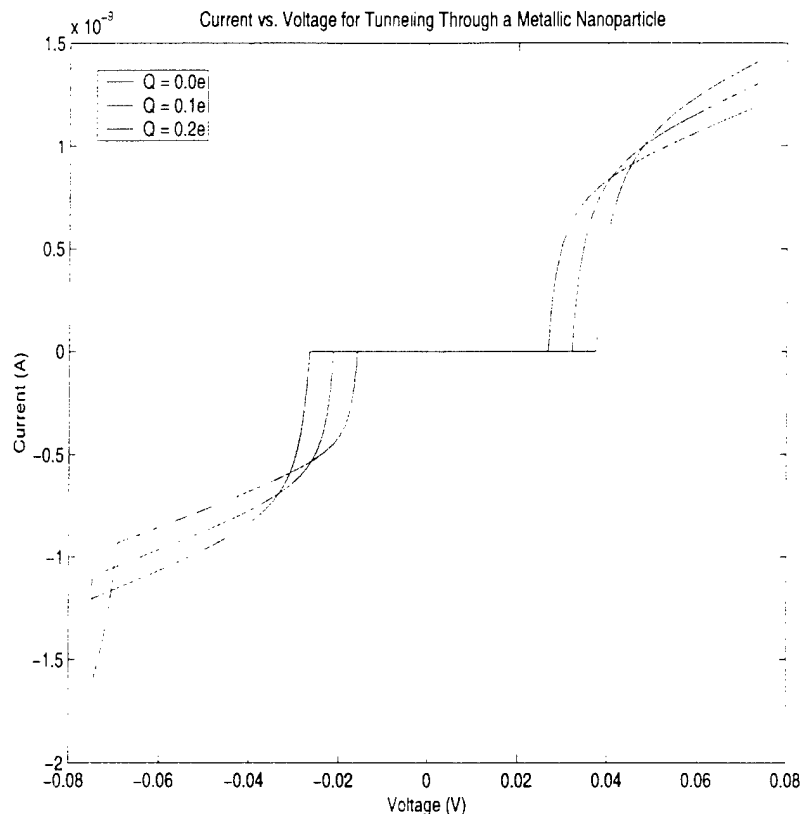


Figure 3.7: Plot of dI/dV vs. V for $Q_0 = 0.0e$, $0.1e$, and $0.2e$. Note that e is a negative quantity. Remaining nanoparticle parameters are the same as in Figures 3.2 and 3.3.

Coulomb staircase slightly to more positive or to more negative voltages depending on its sign. If the offset charge is negative, for example, the barrier for the first electron to tunnel onto the nanoparticle will be slightly greater than normal because the electron must overcome the standard Coulomb repulsion *plus* the extra Coulomb repulsion of that fractional charge. This will shift the entire Coulomb staircase to the right. This is exactly what we see in Figure 3.7 where we have plotted the linear conductance for $Q_0 = 0.0e$, $0.1e$, and $0.2e$. Without a gate electrode, there is no way to control the offset charge on the nanoparticle.

We have now closely investigated all of the parameters that affect the structure of the Coulomb staircase. Now that the theory behind single electron tunneling has been discussed both through basic principles and using a computer simulation, we can move on to a discussion concerning the fabrication of such metallic nanoparticles.

Fabrication and Measurement

There are three major stages to the fabrication of the Fe-doped Cu nanoparticles investigated in this experiment: The first stage involves a KOH etch that creates the silicon nitride membrane window which serves as the nanoparticle substrate; the second stage involves electron-beam lithography and a reactive-ion etch (RIE) to define a small (~ 4 nm in diameter) hole in the nitride window; the third stage involves evaporating a series of metallic layers on both sides of the 4 nm hole in order to create the nanoparticle and its two electrical leads. All of these steps are illustrated in Figures 4.1, 4.3 and 4.4. Although the basic method may be found in other references (see, for example, Reference [3]), the details of the nanoparticle fabrication are specific to our nanoparticle design and, therefore, have been included below. Note that other references have fabricated devices in which the leads and nanoparticle are of the same metal. For reasons discussed below, we have constructed a heterogeneous device in which the leads are aluminum and the nanoparticle is a copper/iron alloy.

4.1 Fabrication of Cu[Fe] Nanoparticles

The first stage in the process, illustrated in Figure 4.1, is to create a low-stress, free-standing membrane which serves as the substrate for the nanoparticle fabrication¹. As a first step, a 50 nm thick layer of Si_3N_4 is deposited on both sides of a standard 3" diameter, 15 mil thick, Si[111] wafer. There are two different plasma deposition systems which can deposit such a layer. A Plasma Enhanced Chemical Vapor Deposition

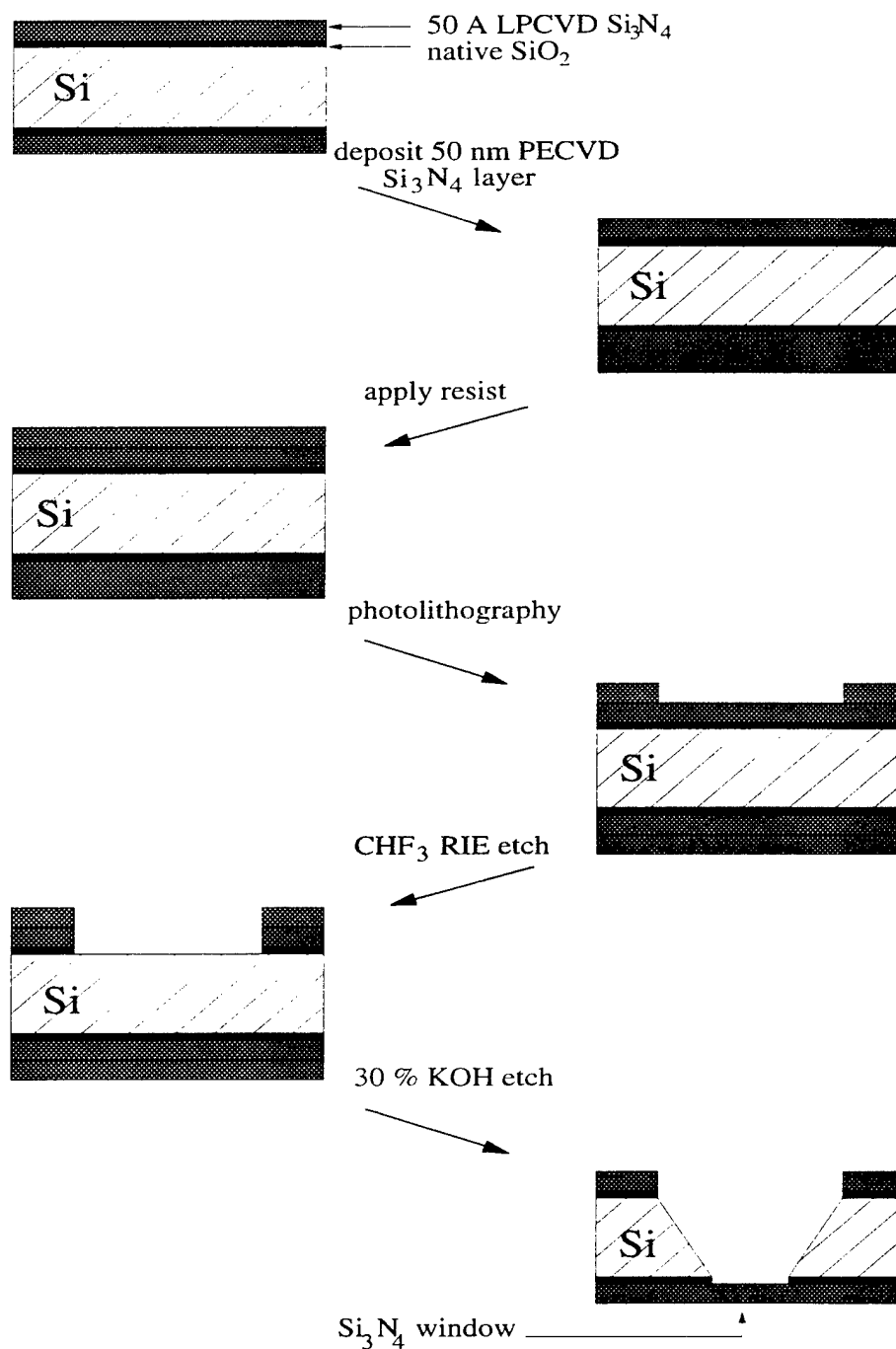
¹A detailed description of the nanoparticle fabrication process has been included in Appendix D.

(PECVD) system, such as the one in the Sohn laboratory at Princeton University, deposits Si_3N_4 layers with microscopic pinholes. These pinholes allow for a chemical etch, such as the KOH etch used to create the windows, to penetrate through the Si_3N_4 layer and destroy the silicon substrate. A second system, using Low Pressure Chemical Vapor Deposition (LPCVD), does not have this particular pinhole problem. Consequently, a 50 nm thick LPCVD Si_3N_4 layer was deposited on our Si substrates at the National Nanofabrication Users Network Facility at Cornell University. The Si_3N_4 layer deposited on the “bottom” of the wafer becomes the free standing nitride window, and the Si_3N_4 layer on the “top” serves as a mask for the chemical etch. Using the PECVD system, we deposit a second 50 nm layer of Si_3N_4 on the “window” side of the wafer. This nitride layer, while quickly etched away in KOH, protects the thin nitride layer from scratches during photolithography.

A 4×4 grid of 5×5 mm square windows is defined on the Si_3N_4 wafer using photolithography. The mask pattern used for the photolithography is shown in Figure 4.2. Next, the native silicon oxide layer and the Si_3N_4 layer on the nitride-covered silicon wafer are removed using a CHF_3 reactive-ion etch (RIE) so as to expose the silicon wafer within the photolithographically-defined squares. The wafer is then placed in a 30 % (by weight) KOH solution at 80-85° C. The KOH etch can take from 2 to 5 hours depending on the concentration and temperature of the solution. As seen in Figure 4.1, the KOH will etch the silicon wafer preferentially in the $\langle 111 \rangle$ direction at an angle of 54° from the wafer surface, and the 5 mm \times 5 mm squares defined using photolithography etch to free-standing Si_3N_4 membranes which are $500 \mu\text{m} \times 500 \mu\text{m}$ in dimension.

On the Si_3N_4 membrane, we next prepare a bilayer of electron-beam resist (PMMA/MMA 10% by weight and 1.5% 950K PMMA). Using electron-beam lithography, a hole ~ 40 nm in diameter is created in the bilayer of resist. This hole exposes a tiny dot in the silicon membrane in the same way that the photolithography exposed a portion of the original wafer for the KOH etch. Using another CHF_3 RIE etch, this 40 nm hole is transformed into a bowl-shaped formation which just breaks through the bottom of the membrane, leaving an opening in the membrane ~ 4 nm in diameter. These steps are illustrated in Figure 4.3.

Onto the “bowl” side of the wafer we evaporate 1000 Å of aluminum, which fills

Figure 4.1: Steps involved in the fabrication of Si_3N_4 windows.

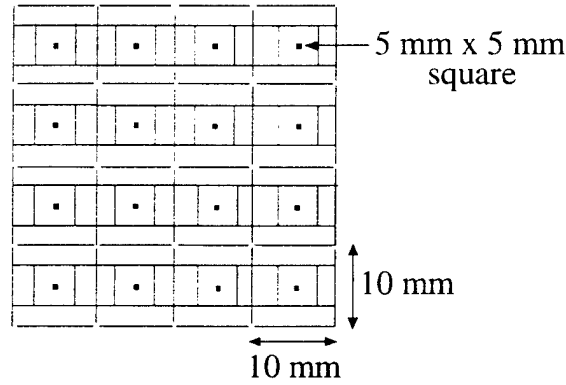


Figure 4.2: Mask design for photolithography.

the bowl and provides stability to the sample. The sample is then oxidized in 50 mT of pure O_2 for 2 minutes. This creates a thin oxide layer at the 4 nm opening in the membrane window. On the other side of the sample, we evaporate $\sim 20 \text{ \AA}$ of a 0.01% Fe in Cu alloy². This layer forms islands on the surface of the membrane. The device will only be successful if one of the islands forms under the opening in the membrane. In the next step we deposit a very thin 10-15 \AA layer of aluminum onto the islands and oxidize in 50 mT of pure O_2 for 2 minutes as before. Ideally, the oxidation is timed precisely so that all the aluminum, and none of the copper nanoparticle, has been oxidized. We have, in effect, deposited a 15 \AA layer of insulating Al_2O_3 . Finally, we evaporate another 1000 \AA of aluminum to form the second lead of the nanoparticle. These steps are illustrated in Figure 4.4.

The thin film deposition mechanism at this stage of the fabrication is not well understood. There are three mechanisms by which a thin evaporated film may form on a surface. There is layer growth, island growth, and layer followed by island growth. The first two are briefly discussed in Chapter 5; for a more in depth treatment, see References [19] and [20]. It should be noted, however, that in order to promote island growth for the Cu[Fe] layer, it is necessary to keep the sample at, or above, 300 K. This is achieved by turning off the cooling water to the sample manipulator. It is also necessary to promote layer growth for the aluminum. In order to keep the sample appropriately cold for this evaporation, the sample must be kept at 77 K by running liquid N_2 instead of cooling water through the sample manipulator. The specific

²This alloy was prepared by ACI Alloys in San Jose, CA.

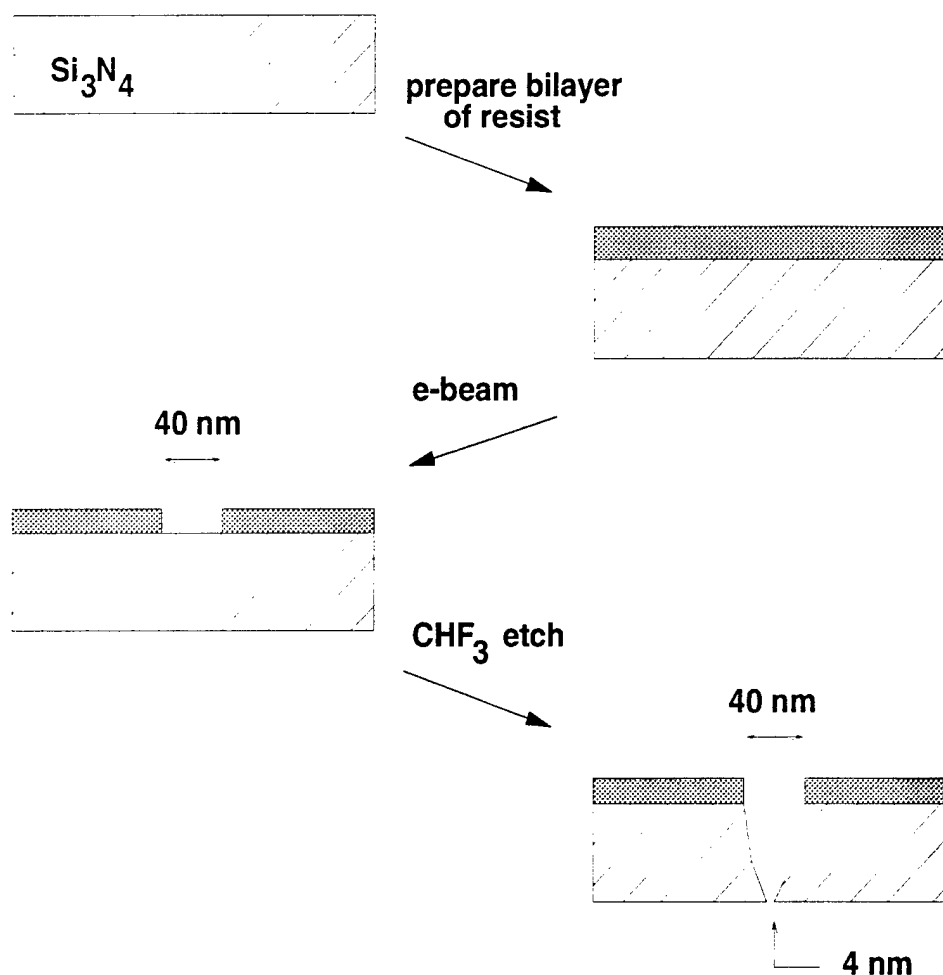


Figure 4.3: Electron-beam lithography stage of nanoparticle fabrication.

deposition parameters are discussed in depth in Chapter 5.

4.2 Electron-Transport Measurement

In our experiment, the electron-transport properties of the nanoparticles are measured using two systems. After fabrication, the linear conductance of the nanoparticles is measured at 4 K in order to select viable samples. Those samples exhibiting Coulomb Blockade are investigated more closely using differential measurements over a range of temperatures from 10 - 50 K. Both of these measurement schemes will be discussed in detail below.

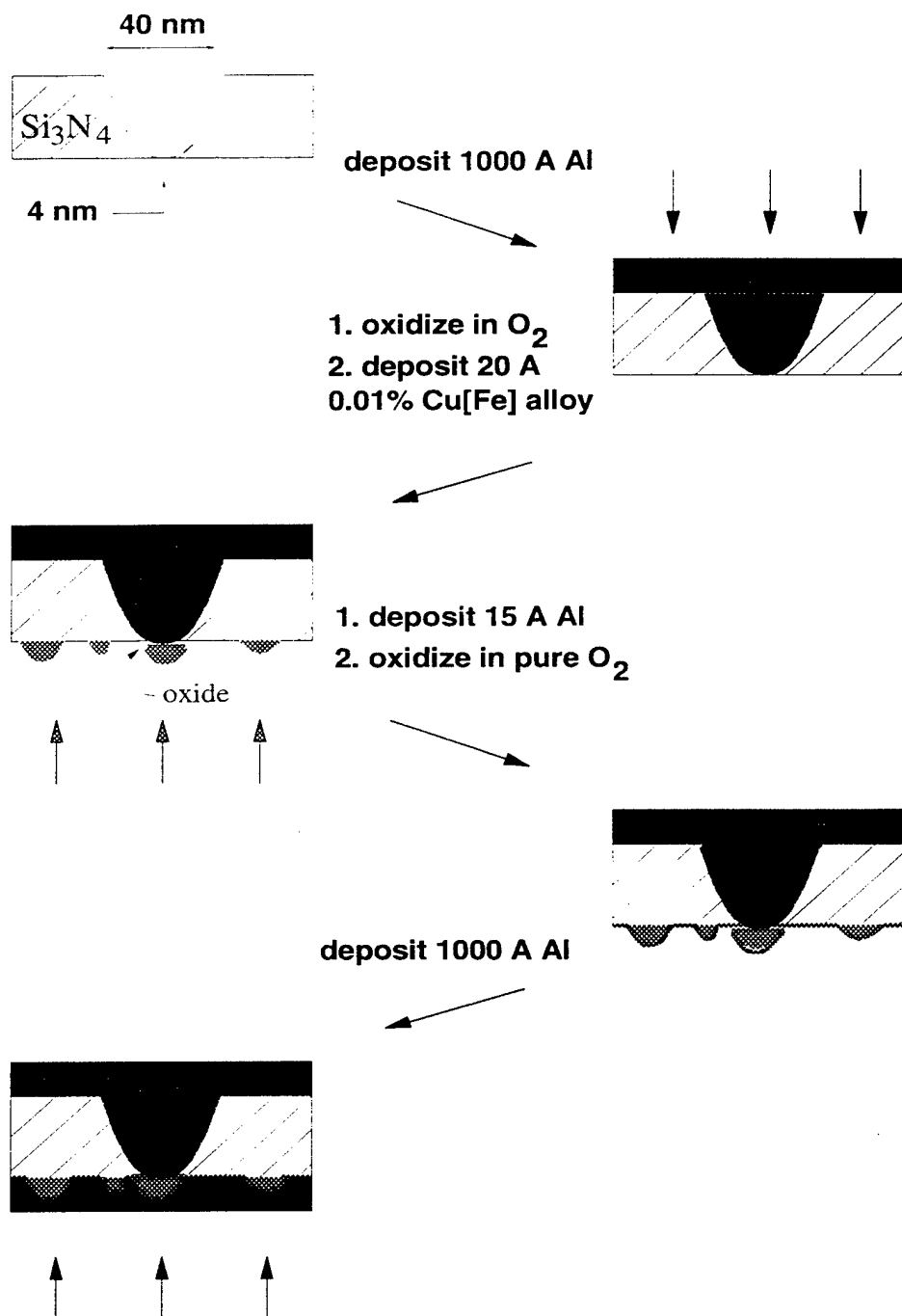


Figure 4.4: Evaporation stage of nanoparticle fabrication.

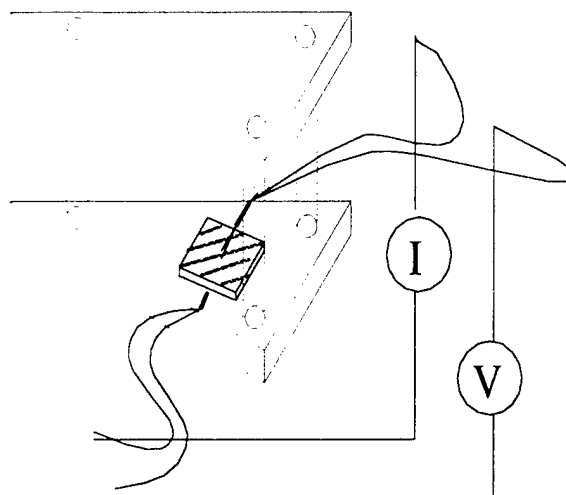


Figure 4.5: Schematic of sample holder and four-point measurement.

4.2.1 Linear Conductance Measurements at 4 K

The linear conductance measurements at 4 K are performed in a 100 L helium dewar. The sample is sandwiched between two teflon triangles which are held together by screws at the corners. As shown in Figure 4.5, there are two copper wires held below the sample and two above the sample. In a standard four-point measurement, two wires will be used to measure the current and the other two to measure the voltage across the sample. The sample holder designed for the nanoparticle samples is illustrated in Figure 4.5.

The sample holder in Figure 4.5 is screwed into a brass plate which is itself affixed to the bottom of an insertable cryogenic probe. The cryogenic probe is illustrated in Figure 4.6. The four wires are soldered to pins, which are inserted into a four pin connector at the side of the brass plate. The four pin connector is, in turn, connected to a ten pin connector at the top of the probe. This ten pin connector is used to connect the entire dewar/probe system to the electronics.

In order to take data at several different temperatures, we need to both measure the temperature at the sample and change that temperature over the correct range. In order to measure the temperature, we attached a Cernox Resistance Temperature Sensor to the brass plate on which the sample holder sits. Two wires are soldered to the temperature sensor and are connected at the top of the probe to a second ten pin

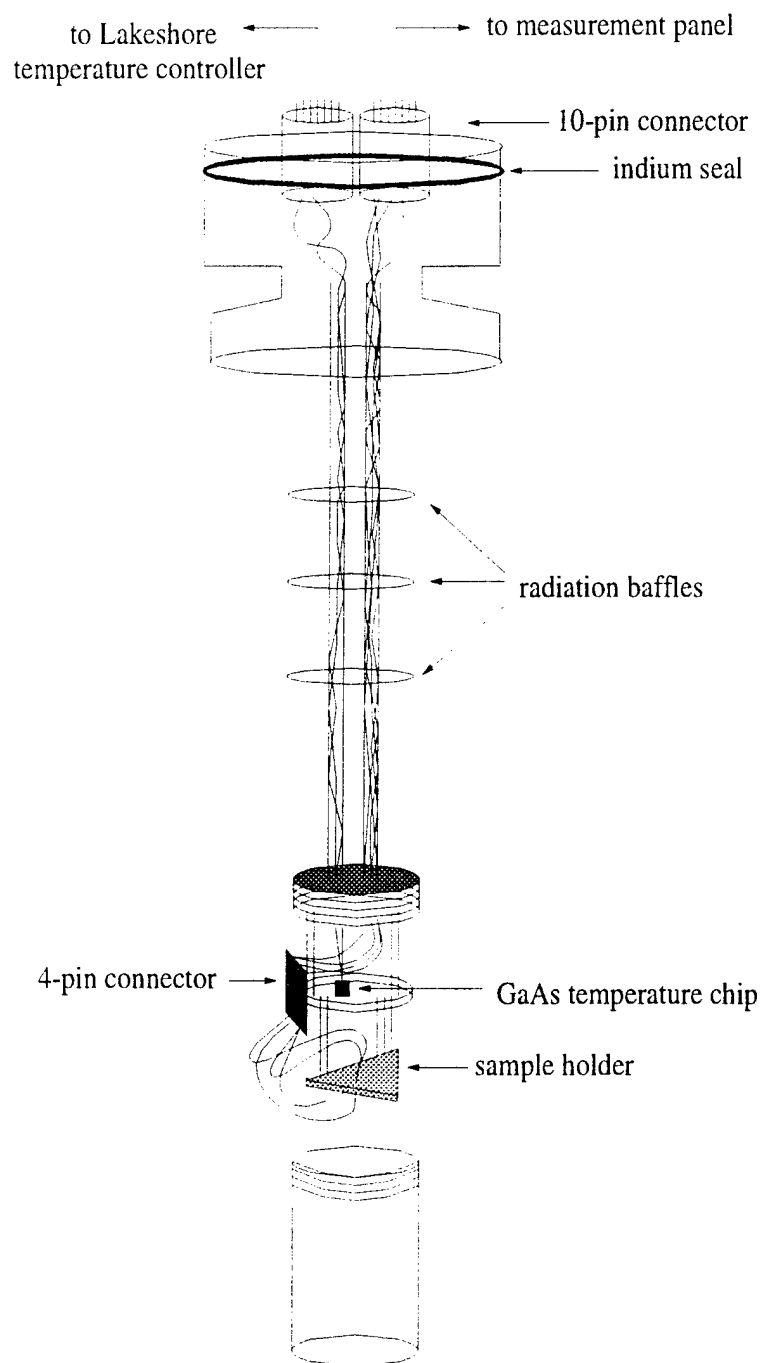


Figure 4.6: Schematic of insertable cryogenic probe.

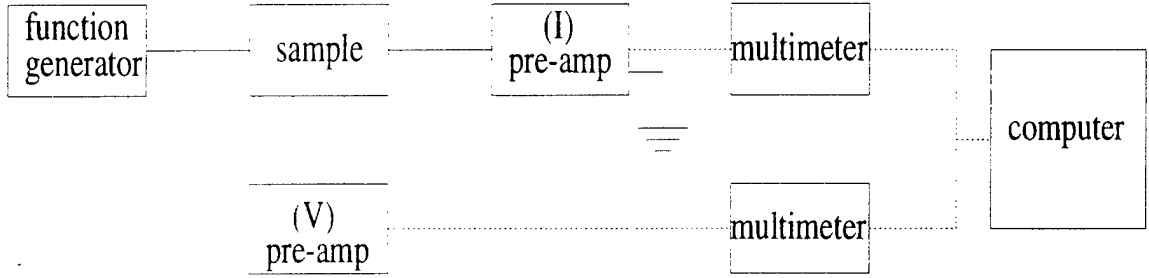


Figure 4.7: Schematic of electronics for the linear conductance measurements. Elements in the primary circuit are connected with solid lines, while the elements used for measurement are connected to the primary circuit via dashed lines.

connector. In order to reduce the noise in the data due to the temperature measurement, we isolated the two sets of wires from the sample to the ten pin connectors as shown in Figure 4.6. In order to measure the temperature, a Model 340 LakeShore Temperature Controller is connected to the ten pin connector at the top of the probe. To vary the temperature throughout the range of 10-50 K, we insert the measurement probe by incremental amounts into the helium dewar.

The probe is evacuated with a mechanical pump³ and helium gas is released into the evacuated probe as a heat-exchange gas. The insertable cryogenic probe is designed to fit through the top and into a 100 L liquid helium dewar. Submerged in liquid helium, the probe and the sample are then cooled down to 4.2 K.

To perform the four-point measurement, we apply voltage across the sample using a synthesized function generator (Stanford Research Systems Model DS345) which produces a triangle wave with some amplitude V_{max} , where V_{max} can range from 80 mV to 500 mV depending on the sample. The current is measured by passing it to ground via an Ithaco 1211 Current Preamplifier. The voltage across the sample is measured simultaneously with a Princeton Applied Research Model 113 Pre-Amplifier. The outputs from the current and voltage preamplifiers are digitized using two Hewlett Packard 34401A multimeters and sent to a computer for storage. In this way, the current across the sample may be measured through a range of voltages. A schematic of the electronics is included in Figure 4.7.

It should be noted that, although the samples are mechanically stable, they are

³Were the cryogenic probe not evacuated, water in the probe might condense and freeze on the electronics.

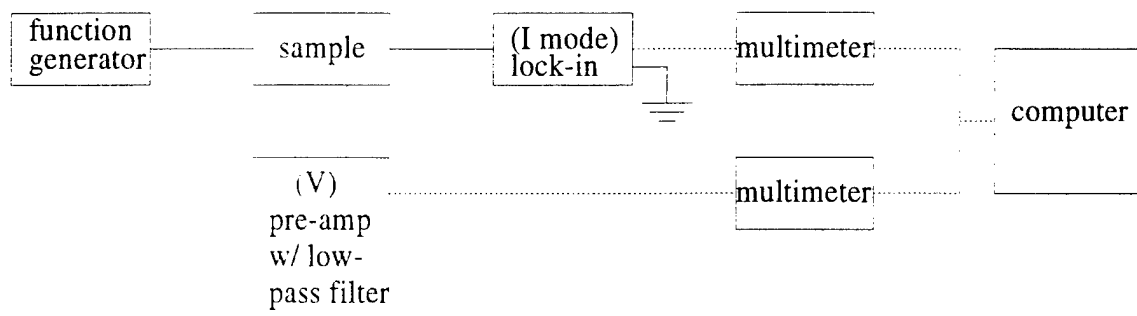


Figure 4.8: Schematic of electronics for the differential conductance measurements. Elements in the primary circuit are connected with solid lines, while the elements used for measurement are connected to the primary circuit via dashed lines.

extremely charge sensitive. We were extremely careful to avoid static electricity while handling the samples and the voltage range considered for our linear conductance measurements was limited to ± 500 mV.

4.2.2 Differential Conductance Measurements at 10-50 K

In order to measure the differential conductance of our samples, we modify our electronics from that presented in Section 4.2.1. Using the synthesized function generator, we add a small AC perturbation to the DC signal we pass through our sample. The AC component of the current signal is measured using a Stanford Research Systems Model SR830 DSP lock-in amplifier. The DC bias is measured using the Princeton Applied Research Model 113 Pre-Amplifier set up to pass only low frequency signals. Since the AC signal is small compared with the DC bias, the measurement provides a probe of the slope of the conductance curve as a function of the applied bias. As before, the outputs from the voltage preamplifier and the lock-in amplifier are digitized using two Hewlett Packard 34401A multimeters and sent to a computer for storage. A schematic of the electronics for the differential measurement is included in Figure 4.8.

4.3 Data Analysis

In Chapter 5, we present I-V curves obtained in this experiment. Ideally, the data from each device was obtained by taking several voltage sweeps of the sample. In

order to highlight large scale structure (i.e. Coulomb Blockade) and average out background noise, we use a computer program to process the data. This program inputs all of the I-V data, sorts it according to voltage, bins the data according to voltage bins (~ 1 mV in width), and averages all the data points in each bin. In this way we are able to look more sensitively at the data obtained in this experiment. In some cases, only one voltage sweep was made before the sample “died” due to electrical stress. These cases are mentioned specifically; in all other cases we have processed the data as mentioned above to average over many voltage sweeps.

Having explained the background theory, studied the parameters using computer modeling, discussed the experimental fabrication and measurement scheme, and clarified our analysis technique, we next discuss in detail the data obtained in this experiment.

Data and Analysis

There were two major stages to this experiment. In the first stage, we fabricated pure aluminum nanoparticles with aluminum leads and measured the linear conductance at 4 K. We chose this relatively simple system in order to develop the techniques for nanoparticle fabrication. By measuring the electron transport properties of aluminum nanoparticles, we were able to characterize the nanoparticles we might expect to see in the more complicated copper-iron system. This is best described as the “calibration stage” of the experiment. In the second stage, we fabricated iron-doped copper nanoparticles and studied the differential conductance as a function of temperature in order to investigate the Kondo effect. Both of these stages will be discussed in depth below.

5.1 Al Nanoparticles

Figure 5.1 is a representative linear conductance measurement we obtained from our aluminum nanoparticles. The fabrication for this sample follows that described in Chapter 4 with the exception that instead of depositing a Cu-Fe alloy and then an Al layer, we simply deposited a layer of Al for the nanoparticles and oxidized the nanoparticle surface to form the second tunnel junction. Although the data is relatively noisy (fluctuations ± 50 pA), five steps in the Coulomb Staircase are clearly visible. Superimposed on the data in Figure 5.1 is the computer model developed in Chapter 3 with the following input parameters: $C_1 = 1.0$ aF, $C_2 = 2.8$ aF, $R_1 = 6$ M Ω , $R_2 = 143$ M Ω , and $T = 4.2$ K. Using the fitted capacitances and Equation 2.8, we estimate a 2.4 ± 0.2 nm radius for this aluminum nanoparticle. We were not able

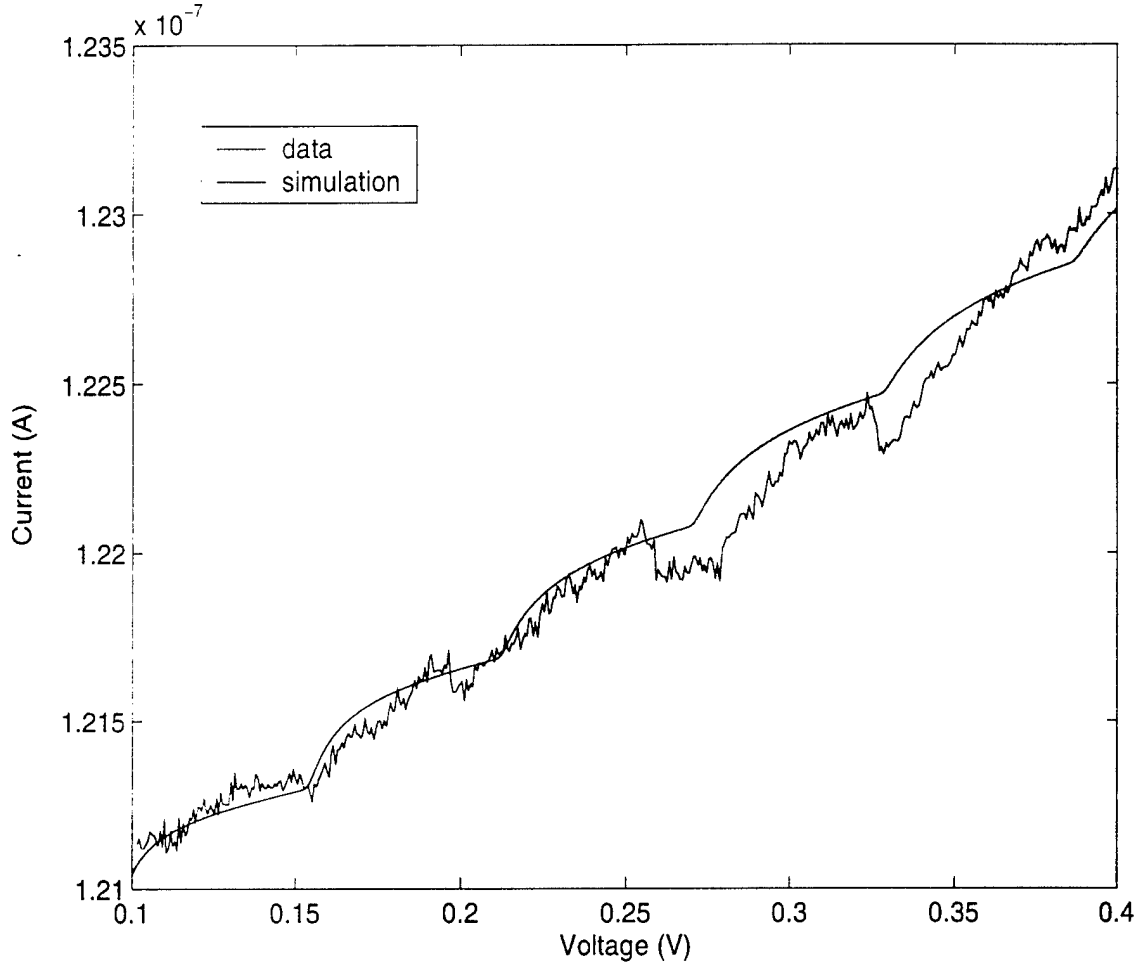


Figure 5.1: Linear conductance from an aluminum nanoparticle. Also plotted is the computer simulation discussed in Chapter 3. The simulation parameters are: $C_1 = 1.0$ aF, $C_2 = 2.8$ aF, $R_1 = 6$ M Ω , $R_2 = 143$ M Ω , and $T = 4.2$ K.

to determine the offset charge, Q_0 , for this device due to a DC offset in both the current and voltage measurements.

As discussed in Chapter 3, the simulation and the experimental data play complementary roles in the analysis process. From the data shown in Figure 5.1, we were able to determine the average voltage step width, $\langle \bar{V} \rangle$, of $57.2 \text{ mV} \pm 8 \text{ mV}$. Using this $\langle \bar{V} \rangle$ and Rule #1 (Equation 3.1) from Chapter 3, we calculate that the larger of the two capacitances, $C_{R>}$, is 2.8 ± 0.4 aF. Now that two of the simulation parameters have been determined, $C_{R>} = 2.8$ aF and $T = 4.2$ K, we can attempt to find values for the other parameters which will most closely fit the experimental data.

Using an iterative process, we select educated but otherwise arbitrary guesses at the four unknown parameters, plot the resulting model against the data, and adjust the parameters accordingly. We continue this process until we get a best, “by-eye”, fit to the data. The purpose of Chapter 3 was to ensure that all of the parameters involved in the single electron tunneling model were well understood so that at this stage, finding the correct parameters in this four-dimensional parameter space was a reasonable task. It should be noted that the nanoparticle parameters given for the data in Figure 5.1 are only approximate. Since the goals of this particular nanoparticle experiment were to a) develop the fabrication technique and b) estimate nanoparticle parameters obtained from this technique, both of these objectives may be fulfilled without getting an exact fit to the data in Figure 5.1. Finally, by examining the effects of changing each parameter separately, we see that each parameter affects the linear conductance differently, and we believe the fit to be unique.

It is also important to note that the data in Figure 5.1 comprises a single sweep in voltage across the nanoparticle. Ideally, the data obtained from these nanoparticle devices is comprised of many sweeps, the data for which are averaged together to form a single, averaged data plot. This was not possible for the sample in Figure 5.1 because, as the direction of the sweep was changed at the top of the sweep, the sample “died”. More care was taken in the future to avoid destroying the sample with rapid changes in voltage or sweep direction.

Another sample which demonstrated a Coulomb staircase structure is shown in Figure 5.2. Unfortunately only one Coulomb step can be resolved in the data and, hence, it is impossible to determine the voltage width of the step. As the voltage width is related to the larger capacitance, $C_{R>}$, which is used to calculate the particle radius, it is not possible to determine the particle size for this sample. Since $\Delta V > 0.7$ V, we can, however, state that the nanoparticle radius is < 1 nm. With our fabrication technique, we do not routinely fabricate nanoparticles with radius < 1 nm. Nevertheless, the linear conductance behavior is distinctive of a Coulomb step and we believe this sample to represent a < 1 nm radius nanoparticle. The parameters used in the computer fit are: $C_1 = 1.0 \times 10^{-3}$ aF, $C_2 = 0.5$ aF, $R_1 = 0.5$ M Ω , $R_2 = 1.0$ M Ω , and $T = 4.2$ K. Note that, for reasons just discussed, these simulation parameters are only rough estimates of the true nanoparticle values. As with the

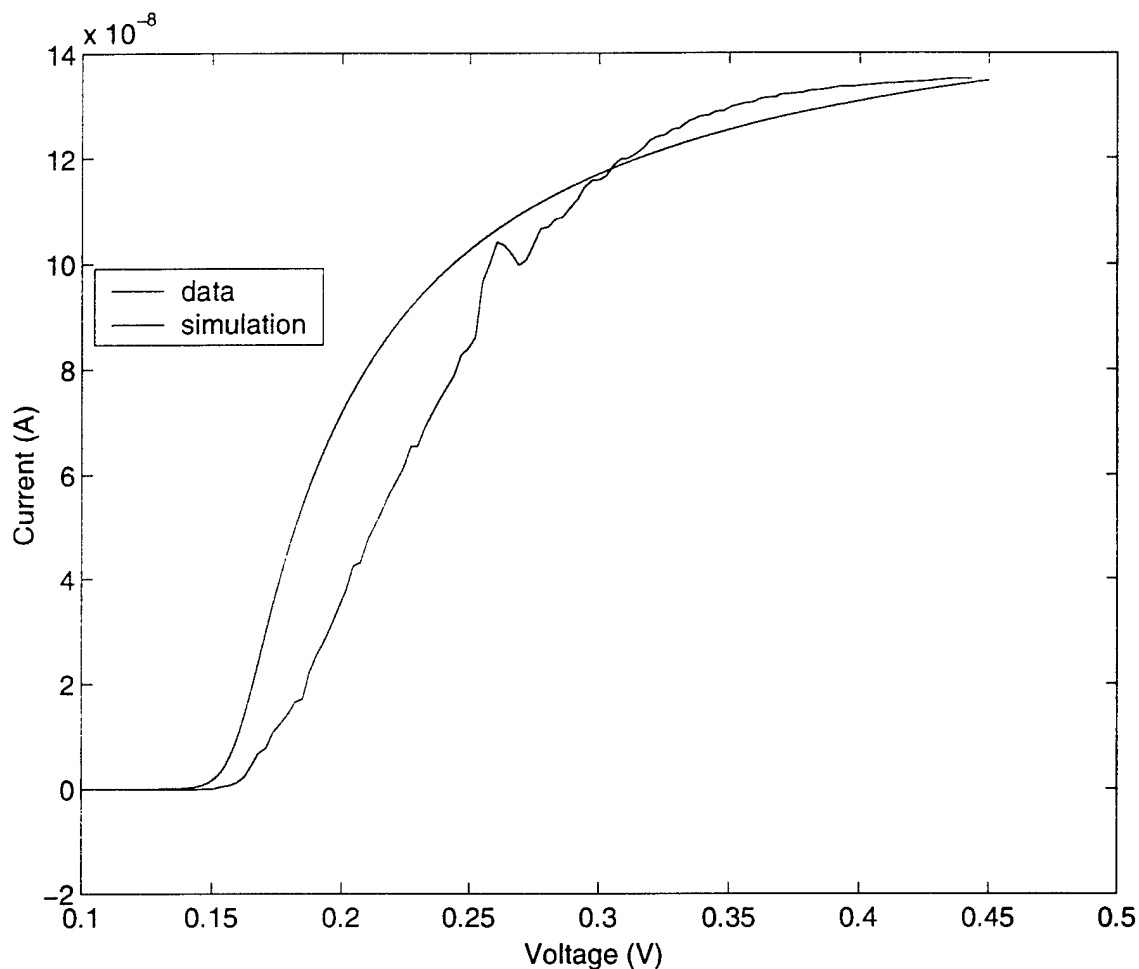


Figure 5.2: Linear conductance from an aluminum nanoparticle at 4.2 K. Also plotted is the computer simulation discussed in Chapter 3. The simulation parameters are: $C_1 = 1.0 \times 10^{-3}$ aF, $C_2 = 0.5$ aF, $R_1 = 0.5$ M Ω , $R_2 = 1.0$ M Ω , and $T = 4.2$ K.

previous sample, we were not able to determine the offset charge, Q_0 , due to DC offsets in the experimental data.

To summarize the data and corresponding fits of Figures 5.1 and 5.2, it is clear that the fabrication process described in Chapter 4 does produce nanoparticles in the size range which we are interested in using for the Kondo experiment.

While the I-V curves in Figure 5.1 and 5.2 are promising, most of the samples did not result in a Coulomb staircase structure. In general, the devices we fabricate fall into four categories according to their conductance behavior - successful devices displaying Coulomb Blockade ($500 \text{ k}\Omega < R < 100 \text{ m}\Omega$), high resistance devices (R

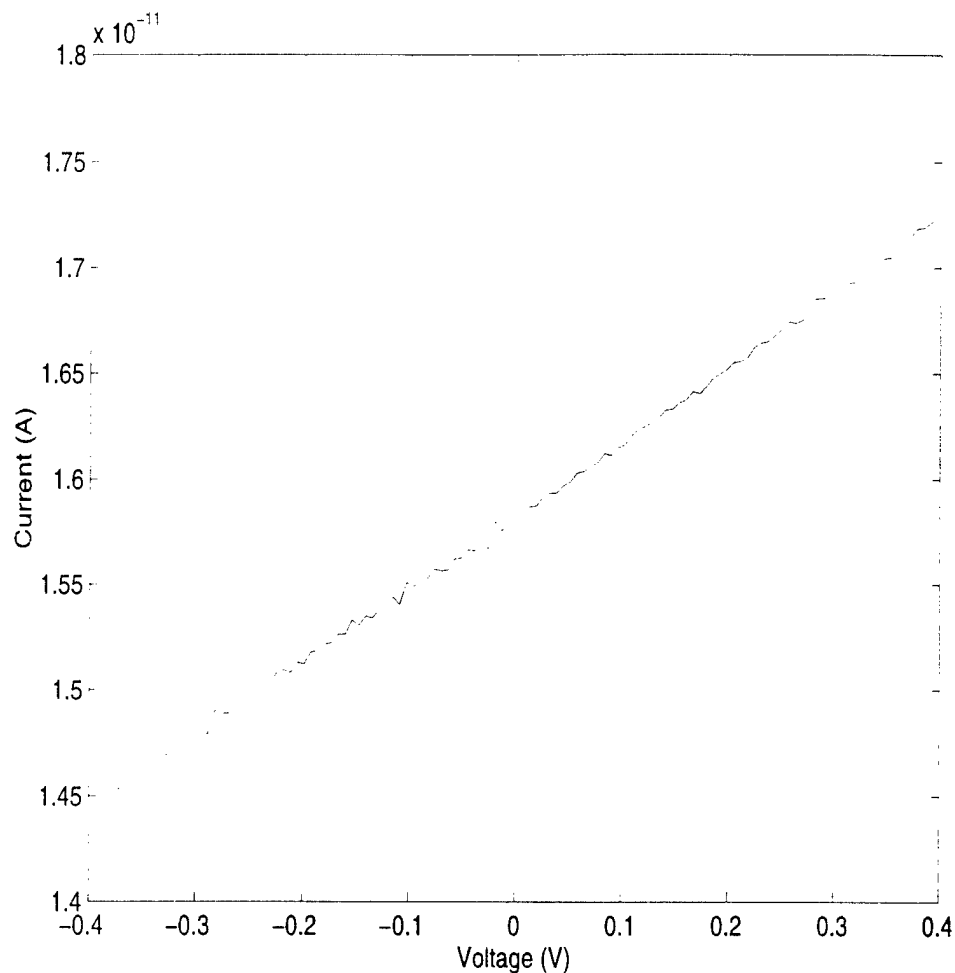


Figure 5.3: Linear conductance at 4K from a high-resistance aluminum nanoparticle.

> 500 M Ω), variable resistance devices displaying unusual temperature dependence, and diode devices displaying rectified behavior¹. The devices demonstrating Coulomb Blockade have already been discussed. The rest of the discussion will be dedicated to understanding what physical mechanisms may be responsible for the unsuccessful devices and what might be changed in the fabrication to eliminate these problems.

The most common types of devices produced in this experiment were high-resistance devices. One example of such a device is shown in Figure 5.3. The resistance of this device is 260 G Ω . There are several possible explanations for these extremely high-resistance devices, and each will be examined separately.

¹Note that the resistance being referred to is R_{Σ} , the larger of the two junction resistances, which is responsible for the overall slope of the Coulomb staircase.

The first possible explanation is that the electron-beam lithography is not fully penetrating through the resist due to poor focusing or insufficient dwell time. Whereas we had originally exposed our samples in the middle of the $500\text{ }\mu\text{m} \times 500\text{ }\mu\text{m}$ window, approximately $250\text{ }\mu\text{m}$ away from where we had last focused the beam, we changed our procedure to define our 40 nm dot at the edge of the window, only $50\text{ }\mu\text{m}$ from the last focus spot. We also ran a test pattern to determine exactly what dwell time would be appropriate to create 40 nm holes in the resist. This particular method consisted of exposing a nitride window to a grid of dots, with dwell times ranging from $200 - 20,000\text{ }\mu\text{s}$. We then cold sputtered $\sim 100\text{ }\text{\AA}$ of AuPd and viewed the resulting pattern using a scanning electron microscope (SEM). Using this method, we determined that a dwell time of $\sim 14,000\text{ }\mu\text{s}$ was appropriate to define a 40 nm diameter hole in the resist. Previous samples, such as that shown in Figure 5.3, were fabricated with a dwell time of only $2000\text{ }\mu\text{s}$. Since the correct dwell time was seven times longer, we can conclude that many of our high-resistance devices were due to poor conduction through a portion of the Si_3N_4 membrane.

Another possible explanation for the high-resistance devices is that the CHF_3 reactive-ion etch (RIE) did not fully etch through the Si_3N_4 membrane window. Once it was determined that $14,000\text{ }\mu\text{s}$ exposure time was sufficient to define the proper hole in the resist, we tried varying the etch time to ensure that we were, in fact, etching fully through the nitride membrane. Since the CHF_3 etch will also etch through the resist (albeit at a slower rate than the Si_3N_4), the etching time is limited by the thickness of the resist which protects the unexposed portion of the nitride membrane. We found that the longest time we could etch the sample without etching completely through the resist was ~ 12 minutes. Since the geometry of the thin membrane limits the amount of Si_3N_4 etching that is possible, we used the maximum amount of etch time allowed by the resist without fear that we would “over-etch” the sample. It is still possible that 12 minutes is not enough time to completely etch through the sample. To explore this possibility it will be necessary to move to a different type of resist.

Yet another possible explanation for the high-resistance devices is the oxide layer. One of the benefits of developing the techniques using aluminum nanoparticles is the relative simplicity of making an oxide with aluminum. The most obvious way to

oxidize the aluminum sample is to expose it to air. For much of this experiment, this was the method which we used. In order to use a more easily reproducible method for oxidizing the samples, we switched to oxidizing our samples in pure O_2 . Other experiments using the same nanoparticle design report oxidizing their samples in 50 mT of pure O_2 for 2 minutes [3]; accordingly, this was the oxide recipe with which we started. It is possible that for the geometry of our system, 50 mT for 2 minutes creates an oxide layer that is too thick. If this is the case, it would explain the predominance of high-resistance devices among our samples.

The final explanation for the high-resistance devices would be that an aluminum island is not forming at the opening in the Si_3N_4 membrane. As discussed in Section 5.2.2 below, the formation of islands during the thin aluminum deposition is a statistical process, and islands will form randomly along the surface of the membrane. It is only by chance that an island will form under the opening of the bowl. Other groups have reported that in 20% of the samples a nanoparticle will form under the bowl opening [14]. It is possible that many of the high-resistance devices that we measure are good devices in which an island did not form under the opening of the bowl. Although there is no obvious method for improving the chances that an island will form at the opening in the nitride membrane, we may produce more successful samples simply by fabricating and testing a large number of samples in parallel.

Several of the samples demonstrated unusual temperature dependence in the linear conductance. In Figure 5.4 we show the linear conductance of an aluminum nanoparticle sample as it warms from 4.2 K to room temperature. As the sample warms, the conductance through the sample increases continuously from being almost zero over the entire voltage range measured to being significant at room temperature. Unfortunately, other than at the end points of the temperature spectrum, the I-V curves in Figure 5.4 are not temperature resolved. In order to study this unusual temperature dependence more carefully, we chose another sample which demonstrated similar behavior and measured the resistance² as a function of temperature. The family of curves for this sample is shown in Figure 5.5. The resistance clearly depends strongly on the temperature, and hence most of the curves in Figure 5.5 cannot be resolved. For this reason, the slopes of these I-V curves, which will be used extensively in the

²The resistance was measured by taking a best fit line to the I-V curve in the range $-10 \text{ mV} < V < 10 \text{ mV}$.

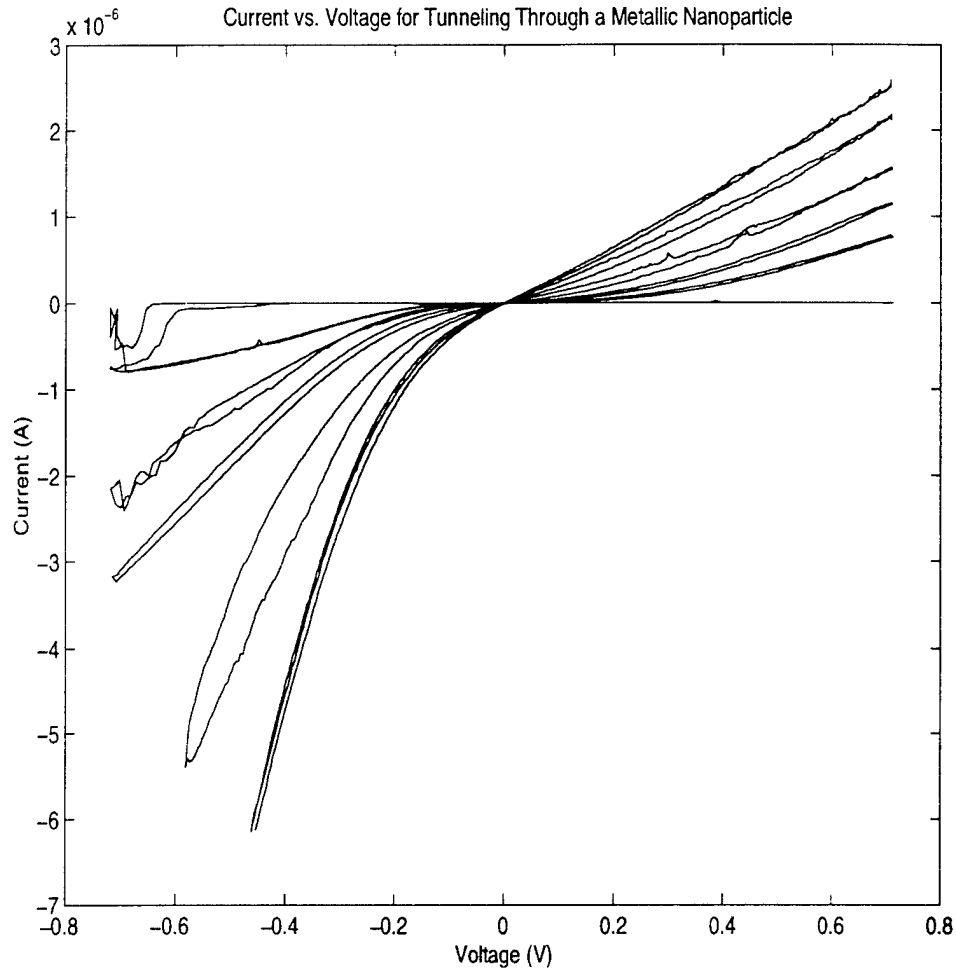


Figure 5.4: Linear conductance from an aluminum nanoparticle as the sample warms from 4 K to room temperature. The lowest current curve is the 4 K curve, and the highest current curve is the room temperature curve. All other curves lie linearly between these two temperatures.

following discussion, are included in Table 5.1.

Ideally, the conduction through our nanoparticle devices is dominated by transport through a metallic nanoparticle. If this is not the case, we can hope to understand what is dominating the transport through these devices by examining the temperature dependence in Table 5.1. By identifying the dominant mechanism by which electrons conduct through our samples, we can hope to correct our fabrication technique in order to increase our yield of successful devices.

The first question to ask is whether or not the conductivity in Table 5.1 may be

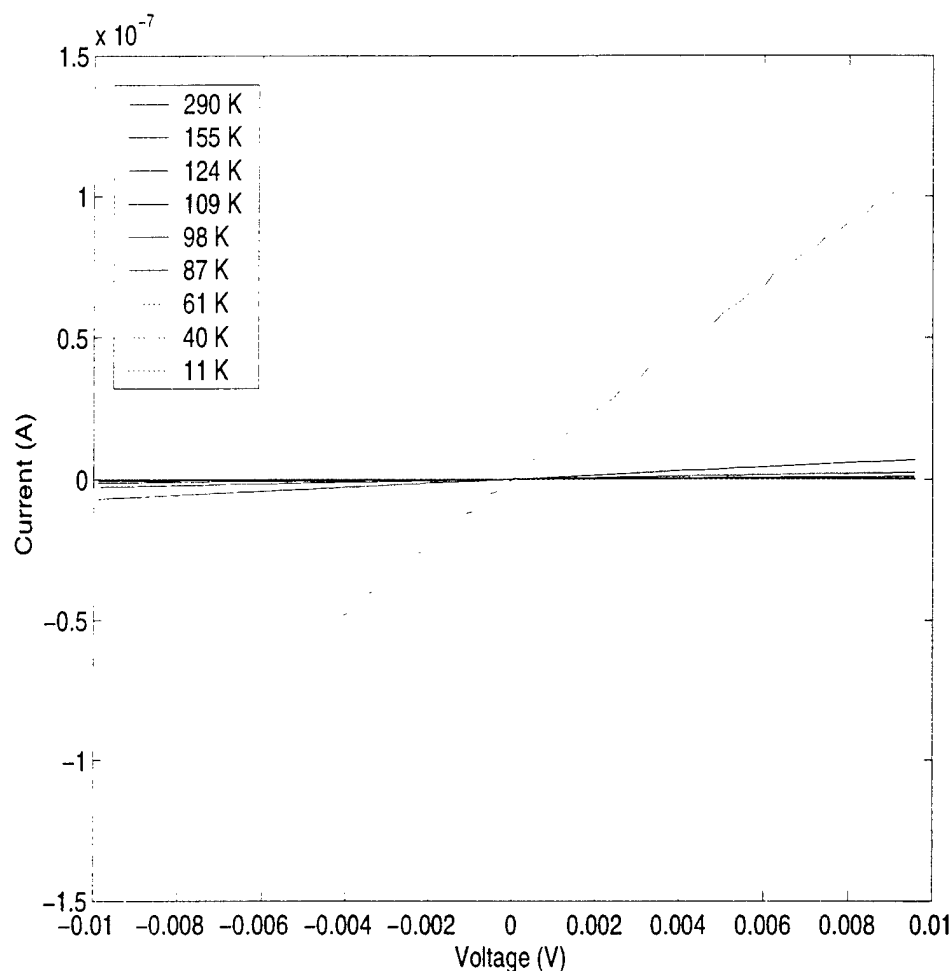


Figure 5.5: Linear conductance from an aluminum nanoparticle for a range of temperatures from 290 K to 11 K.

explained by simple conduction through a metal. It can be shown that resistivity in metals is due entirely to deviations from perfect periodicity of the ions in the lattice [21]. For undoped metals, such as the aluminum nanoparticles we are considering, the greatest contribution to deviations in the lattice is due to thermal vibrations of the ions from their equilibrium positions. As the temperature decreases, the ions have less energy to vibrate about equilibrium. This decreased ion motion at lower temperatures causes the resistivity in metals to decrease with decreasing temperature³. We can see immediately that this behavior does not match that seen in Table 5.1

³It was a logarithmic *increase* in resistivity with decreasing temperature that was the first experimental evidence of the Kondo effect.

temperature (± 1 K)	resistance (Ω)
290	8.54×10^4
155	1.42×10^6
124	3.78×10^6
109	8.53×10^6
98	2.24×10^7
87	5.27×10^7
61	4.56×10^8
40	4.52×10^{11}

Table 5.1: Temperature vs. resistance for aluminum nanoparticle sample. The error in the resistance measurement is negligible compared to the error in the temperature.

and can conclude, therefore, that conduction in metal does not dominate the electron transport through these variable resistance nanoparticle samples.

The second question to ask is whether or not the superconducting behavior of aluminum at very low temperatures could be responsible for the unusual temperature dependence we see in Figures 5.4 and 5.5. However, since the critical temperature T_c for aluminum is 1.2 K, and the unusual temperature dependence is seen at temperatures $T \gg T_c$, we cannot explain our data by considering superconductivity in the aluminum.

As another attempt, we can ask whether or not the unusual temperature dependence can be explained by considering conduction through a semiconductor. Although we do not expect to have any semiconducting materials in our devices, consider the possibility that in our fabrication, we did not etch completely through the Si_3N_4 window. In that case, electrons from the first electrical lead would have to tunnel through a very thin ($\ll 50$ nm) layer of insulating Si_3N_4 before reaching the nanoparticle. Evidence of semiconducting behavior would give us valuable information about the quality of our “insulating” Si_3N_4 layer.

Semiconductors are characterized by a band gap E_g which is small enough that thermal excitations can lead to significant conductivity. The fraction of electrons excited from the valence band across the band gap to the conduction band is directly proportional to the conductivity σ , which is related to the band gap by

$$\sigma \sim \exp \frac{-E_g}{kT} \quad (5.1)$$

where T is the temperature available for thermal excitations and k is the Boltzmann constant. Since the resistance of the sample must then be related by

$$R \sim \exp \frac{E_g}{kT} \quad (5.2)$$

a plot of $\ln R$ vs. $1/T$ should result in a straight line with slope equal to E_g/k , where E_g is the band gap and k is the Boltzmann constant. We have plotted the data in Table 5.1 in this manner; the results are shown in Figure 5.6. We see that $\ln R$ and $1/T$ are, in fact, linearly related with a slope of 686.6 ± 0.2 K. From this slope we calculate the band gap to be 59.22 ± 0.02 meV. Typical semiconductor band gaps range from 100 meV to ~ 5 eV. Since our calculated band gap is significantly out of this range, we conclude that, despite the close linear relationship between $\ln R$ and $1/T$, the conductivity through the sample is not dominated by simple conduction through a semiconductor.

Another possible explanation for this unusual temperature dependence is the phenomenon of “variable range hopping” [22]. Other groups have attributed similar temperature dependence in the resistivity of their nanoparticle samples using this phenomenon [23]. The original calculations by Mott [24] were used to explain unusual temperature dependence in transport through semiconductors, and with few modifications we can hope to explain our own unusual temperature dependence using this phenomenon.

The term hopping is used to describe phonon-assisted tunneling from one localized state in a band-gap to another. Considering the schematic in Figure 5.7, we see in the band gap a number of states which may be accessed by electrons in the valence band. As an insulator, the Si_3N_4 does not have states which will allow the electrons to conduct freely through the sample. However, by “hopping” from one localized state to another within the gap as shown in Figure 5.7, electrons may travel through the thin Si_3N_4 barrier. The following derivation follows closely that in Reference [22].

Phonon-assisted transitions occur when electrons in the valence band absorb or emit a phonon from the bulk. In order for transport through the insulator to be possible, electrons from the valence band must absorb a phonon from the solid, and

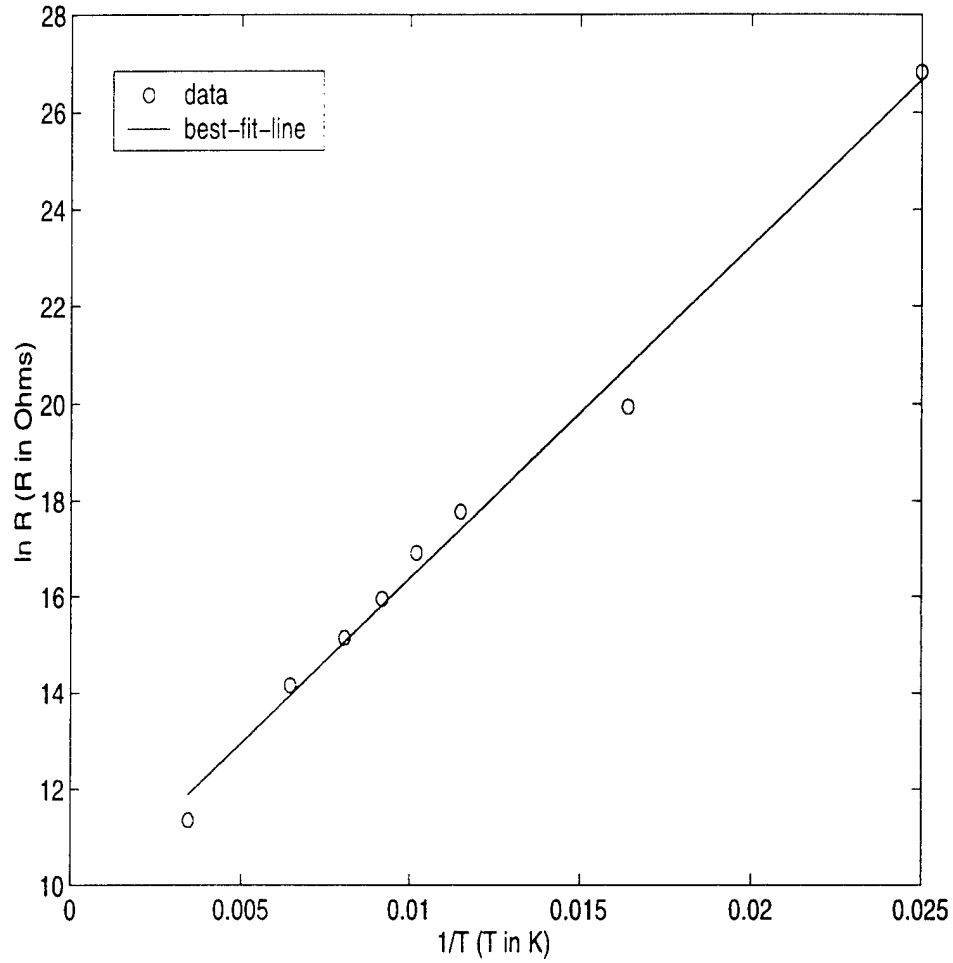


Figure 5.6: $\ln R$ vs. $1/T$ for the data in Table 5.1. The equation of the best-fit line is: $\ln R = 9.52 + 686.6 \frac{1}{T}$.

therefore, the conductivity depends strongly on the temperature. The probability of having a phonon-absorbing hop of distance X and energy W at a temperature T is given by

$$p \sim \exp[-2\alpha X - (W/k_B T)] \quad (5.3)$$

where $\exp[-2\alpha X]$ is the probability that, for a wavefunction $\Psi(r)$ which decays as $\exp[-\alpha r]$, the electron will be found a distance X from the original site, and where $\exp[-W/k_B T]$ is the probability that the electron will absorb a phonon of energy W . Note that Fermi-Dirac statistics require that we limit ourselves to transitions within $k_B T$ of the Fermi energy, and that within this narrow band we assume the localization

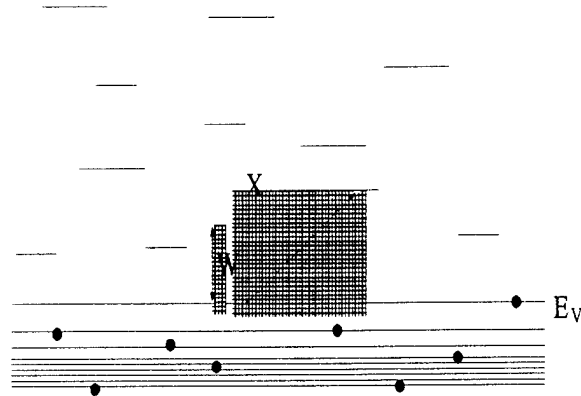


Figure 5.7: Energy schematic of variable range hopping. The solid and the dashed arrows indicate two possible tunneling events. W and X are the energy difference and spatial distance, respectively, involved in the tunneling event represented by the solid line.

length α and the density of localized electron states $n(E_F)$ to be constant.

We have, in Equation 5.3, a trade-off between hops in which the electrons tunnel a long distance spatially or tunnel to a state with a much different energy. Which of these two hopping mechanisms dominates depends on the temperature. The energy difference W and the spatial distance X are related by

$$\pi X^2 W(X) n(E_F) = 1 \quad (5.4)$$

where $n(E_F)$ is the density of localized electron states per unity area per unit energy. If we consider a circle of radius X around the electron, $W(X)$ is defined to be that energy for which the number of states with energy less than $W(X)$ available in that circle is unity. Note that we have explicitly considered the problem to be two dimensional by considering a circle with radius X as opposed to a sphere of radius X . The variable range hopping transport we are considering occurs through an incompletely etched Si_3N_4 membrane. Since the Si_3N_4 membrane is only 50 nm before the RIE, any layer of Si_3N_4 remaining after the RIE will be much thinner than 50 nm, most likely on the order of a typical localization length $\alpha \sim 10 \text{ \AA}$. We therefore consider the variable range hopping transport to occur in only two dimensions.

Solving for $W(X)$ in Equation 5.4 and plugging this back into Equation 5.3, we get that the probability has the following form

$$p \sim \exp[-aX - (b/X^2)]. \quad (5.5)$$

If we minimize the exponent so as to maximize the probability, we get that the most probable hopping distance X is given by

$$X \approx [\alpha k T n(E_F)]^{-\frac{1}{3}} \quad (5.6)$$

where α is the localization length introduced in Equation 5.3. If we assume that the most probable hopping distance dominates, and that the probability for hopping, p , is linearly related to the conductivity, σ , we can simply plug in the X of Equation 5.6 to obtain the following conductivity-temperature relationship

$$\sigma \sim \exp(-A/T^{\frac{1}{3}}) \quad (5.7)$$

or, equivalently, the resistivity-temperature relationship

$$R \sim \exp(A/T^{\frac{1}{3}}) \quad (5.8)$$

where A is given by

$$A \sim \left(\frac{\alpha^3}{k_B n(E_F)} \right)^{\frac{1}{3}}. \quad (5.9)$$

Taking the natural log of both sides of Equation 5.8 we get that

$$T^{\frac{1}{3}} \sim \frac{A}{\ln R} \quad (5.10)$$

and taking the natural log a second time we get that the temperature T and resistance R are related by

$$\ln(\ln R) \sim \ln A - \frac{1}{3} \ln T. \quad (5.11)$$

We see from Equation 5.11 that a plot of the data in Table 5.1 as $\ln(\ln R)$ vs. $\ln T$ should result in a straight line with a slope of $-1/3$. In Figure 5.8 we have plotted $\ln(\ln R)$ vs. $\ln T$. Also included in Figure 5.8 is a best fit line with the following equation: $\ln(\ln R) = 4.77 - 0.42 \ln T$. The correlation coefficient $|r|$ of the data to this best fit line is 0.99, where a correlation of 1.0 is a perfect fit. We see that $\ln(\ln$

R) and $\ln T$ are, in fact, linearly related as predicted in the model of variable range hopping. The slope of -0.420 ± 0.002 , however, is significantly different the predicted value of -0.33 . There are a number of reasons why, even if the correct mechanism for transport is variable range hopping, the slope may deviate from the predicted value of -0.33 . These include, among many others, Coulomb interactions and the precise form of the density of states. $n(E_F)$.

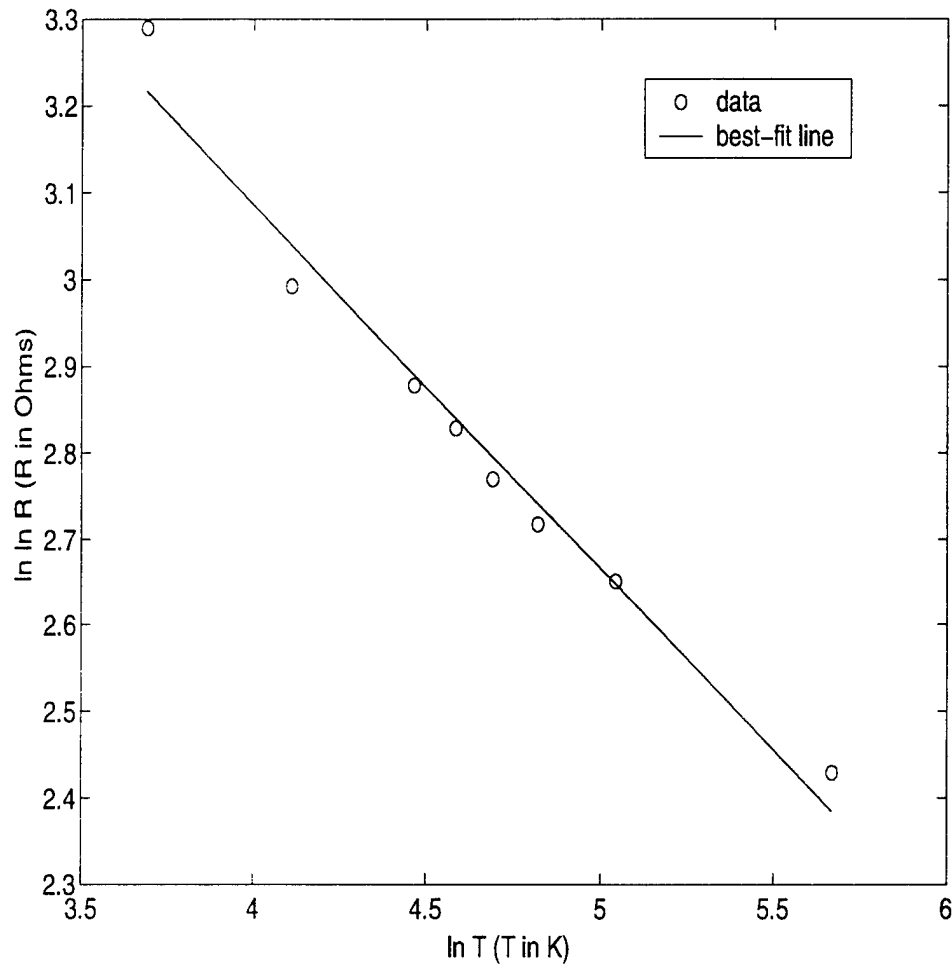


Figure 5.8: Plot of $\ln(\ln R)$ vs. $\ln T$. The equation of the best-fit line is: $\ln(\ln R) = 4.77 - 0.42 \ln T$.

Having eliminated simple conduction through metals, superconductors, and semiconductors as possible mechanisms to explain the unusual temperature dependence of our samples, we conclude that variable range hopping is the most likely explanation for the unusual temperature dependence in our variable range devices. From this

we can tentatively conclude that our variable range devices are the result of having etched incompletely through the Si_3N_4 membrane.

In addition to high-resistance devices and variable resistance devices, many of the samples we fabricated demonstrated rectified behavior indicative of a Schottky diode. The linear conductance of one such device is shown in Figure 5.9. For comparison, a typical Schottky diode I-V curve is included in Figure 5.10.

The physics of Schottky diodes, which occur at a metal-semiconductor interface, may be found in a standard physics textbook and will not be covered here [25]. The important point to be discussed in comparing Figures 5.9 and 5.10 is that the device in Figure 5.9 displays unmistakably rectified behavior. This may be explained by concluding that in this device, we did not etch completely through the Si_3N_4 membrane. Although Si_3N_4 is usually an insulator, impurities in the Si_3N_4 may cause the normally insulating membrane to behave as a semiconductor. The interface between the (semiconducting) Si_3N_4 layer and the metal lead could feasibly result in a Schottky diode, resulting in rectified behavior such as that demonstrated in Figure 5.9. This lends further evidence that a) in these samples we did not etch completely through the Si_3N_4 membrane and b) the Si_3N_4 layer deposited on our substrate is endowed with impurities which result in semiconducting behavior.

In sum, the aluminum nanoparticle experiment has demonstrated a number of important points which we have used in conducting the Kondo experiment described below.

1. Using our technique, we are able to fabricate nanoparticles in the correct size range to investigate the Kondo effect in a confined system.
2. In order to fabricate reproducible oxide layers, it is necessary to oxidize the samples in pure O_2 . The current recipe is to oxidize in 50 mT of pure O_2 for 2 minutes.
3. By moving to a longer electron-beam exposure, and a longer reactive-ion etch, we hope to eliminate the problem of predominantly high-resistance devices.
4. The Si_3N_4 membrane is doped with impurities and acts as a semiconductor rather than an insulator.

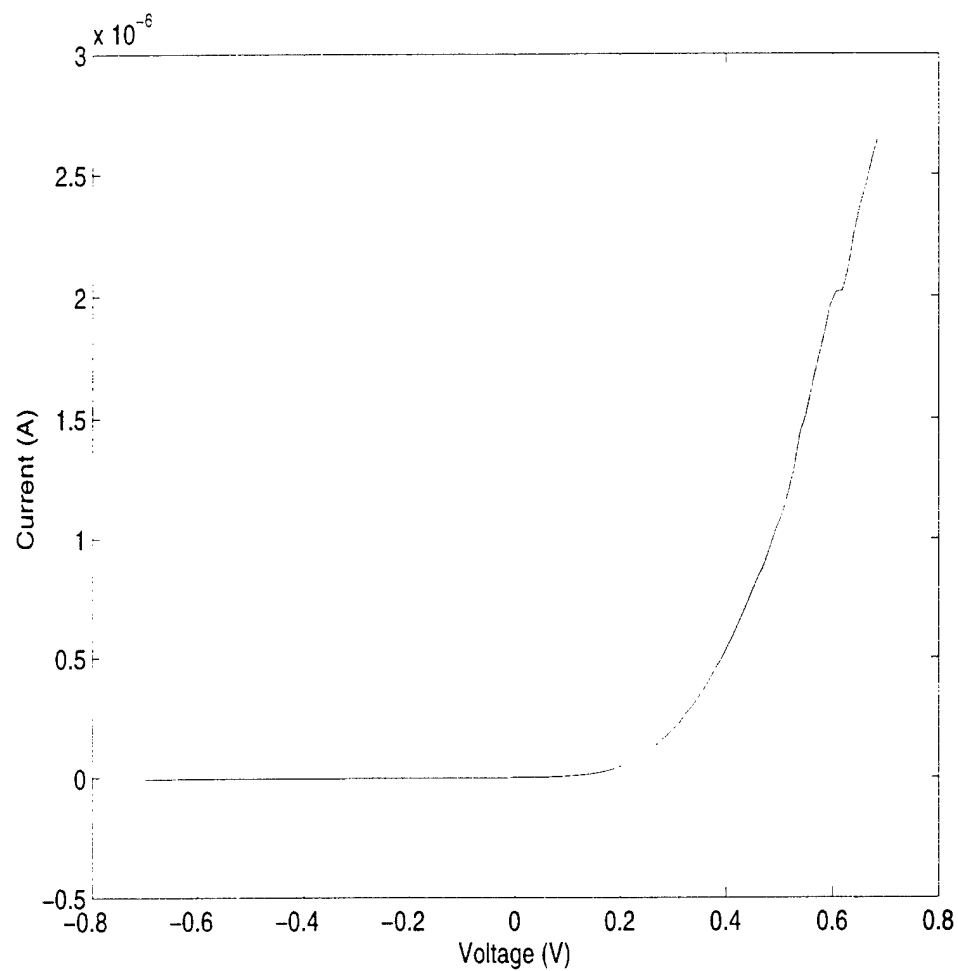


Figure 5.9: Linear conductance from an aluminum nanoparticle at 4 K.

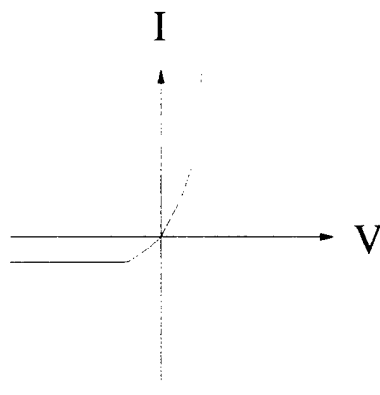


Figure 5.10: Typical I-V curve of a Schottky diode.

5.2 The Cu[Fe] Nanoparticle Kondo Experiment

5.2.1 The Cu[Fe] System

Although the copper-iron system we have chosen to investigate has many advantages, such as a suitable Kondo temperature, it is considerably more complicated experimentally than the aluminum-only system. First, it is not obvious how to fabricate the second oxide junction. One approach would be to oxidize the copper nanoparticle to form a copper oxide tunnel barrier. Another would be to deposit and then immediately oxidize a thin layer of aluminum. Although both methods have been investigated, the latter was chosen and is described in Chapter 4 (see Figure 4.4). The major benefit to depositing and then oxidizing a thin aluminum layer is that aluminum junctions are well characterized, both through our work as presented in Section 5.1 and in other papers [3] [4]. The disadvantage, however, lies in the need to successively deposit two very thin films during fabrication. In order for our samples to represent transport through a nanoparticle instead of a thin film, it is necessary that the Cu-Fe film form islands on the Si_3N_4 surface as shown in Figure 4.4. The next deposited layer is the thin aluminum film which, when oxidized, forms the second tunnel barrier. In order for this aluminum layer to form a spatially homogenous oxide, it is imperative that the aluminum thin film does *not* form islands on the Si_3N_4 surface. In order to successfully fabricate our samples using this two thin film technique, it is important that we understand the mechanisms behind thin film growth on surfaces and the experimental parameters involved in control of these mechanisms. The next section is dedicated to understanding the mechanisms of thin film growth on surfaces.

5.2.2 Thin Film Growth

As mentioned in Chapter 4, there are three mechanisms for thin film growth: layer growth, island growth, and layer followed by island growth. Only the first two will be discussed here; for a more in depth treatment see References [19] and [20].

Island (or Volmer - Weber) growth (illustrated in Figure 5.11) is a process involving mobile adatoms diffusing along a substrate surface. These adatoms diffuse along the surface until they either desorb or collide with other adatoms. These collisions result

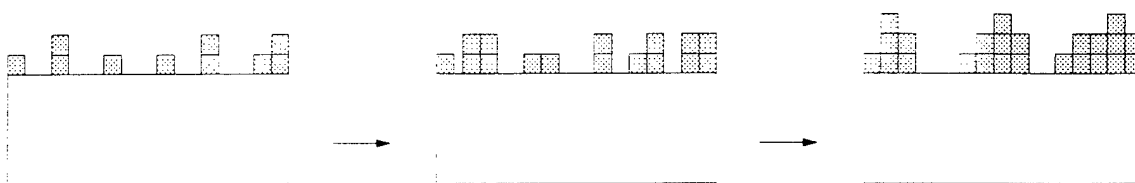


Figure 5.11: Island growth on a substrate.

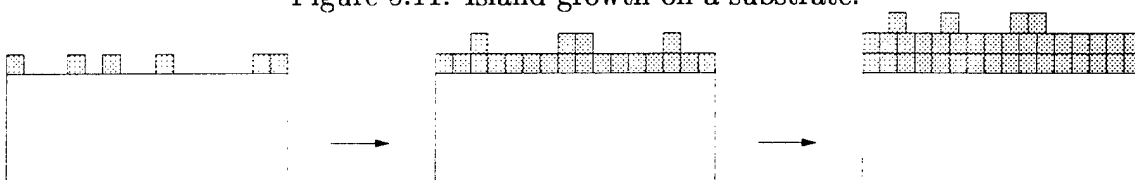


Figure 5.12: Layer growth on a substrate.

in small clusters which themselves diffuse along the surface until they collide with other clusters, forming small islands on the surface. In most cases, only a few atoms are needed to form a nucleus with the critical radius for stable island growth. Once that critical radius has been achieved, island size varies roughly as the square root of the deposition time [19]. As deposition continues, the island size and density become so large that individual islands coalesce to form an unbroken layer on the substrate surface.

Layer (or Frank and van der Merwe) growth (illustrated in Figure 5.12) involves the planar accretion of diffusing adatoms on a substrate surface. Unlike in island growth, the first layer is formed almost entirely before the second layer starts to form.

The two most easily-controlled parameters that determine the dominant growth mechanism are temperature and evaporation rate. As the temperature is increased, the atoms evaporated on the surface have more energy to diffuse along the surface and join up with other atoms, thereby forming clusters and subsequently islands. To reduce surface energy, these islands will be approximately spherical in shape⁴. If the temperature of the surface is much lower, the atoms will not have enough energy to diffuse far from where they land on the substrate surface. If the temperature is much lower still, the atoms will simply stick on the surface where they land. When

⁴In order to reduce the energy associated with surface atoms, which have fewer neighbors than would be most energetically stable, the island will prefer a geometry which maximizes volume while minimizing surface area, i.e. a sphere.

the atoms are not free to move about the surface, no islands can form and layer growth occurs. The same principle applies when considering the effect of evaporation rate on growth mechanism. When the evaporation is slow, the atoms have a lot of time to diffuse and aggregate in clusters and islands. On the other hand, when the evaporation rate is very high, the atoms have no time to move on the substrate surface before the next monolayer of atoms arrives. In this case, layer growth is favored. By controlling the temperature⁵ and the evaporation rate of the two crucial thin films involved in this stage of the fabrication process, we can hope to favor island growth of the copper-iron layer and layer growth for the aluminum layer.

5.2.3 Experimental Data for the Cu[Fe] System

We have yet to fabricate any samples with the copper-iron system that display the Coulomb staircase behavior shown in Figure 5.1. All of the devices so far fabricated display the same high-resistance behavior seen in many of the aluminum-only samples. One example of such a sample is shown in Figure 5.13. This sample has a resistance of 850 M Ω .

Unfortunately, there exist even more possible explanations for the high-resistance behavior in the copper-iron samples than with the aluminum samples. In addition to those mentioned in Section 5.1, there are several possibilities related to the deposition of the two thin films mentioned in Section 5.2.1.

One possible explanation for the unsuccessful Cu-Fe devices is that the aluminum film deposited for the second junction is too thin. If the aluminum film is too thin, or if the temperature during evaporation is too high, the aluminum will “bead up” on the surface to form islands via the island growth mechanism discussed in Section 5.2.2. This would lead to extremely irregular aluminum coverage on the nanoparticle. If an aluminum island forms on top of a Cu-Fe nanoparticle, then oxidation of the sample might create an aluminum junction which is too thick. If, on the other hand, no aluminum remains on the nanoparticle, oxidation of the exposed Cu-Fe nanoparticle may leave insufficient unoxidized metal to form a nanoparticle. For these reasons, it is

⁵There are a number of ways in which the temperature at the sample may be controlled. The easiest method is the use (or absence of) cooling water or liquid N₂ to cool down the sample during evaporation. At this time, it is not clear exactly what range of temperatures may be achieved by this method.

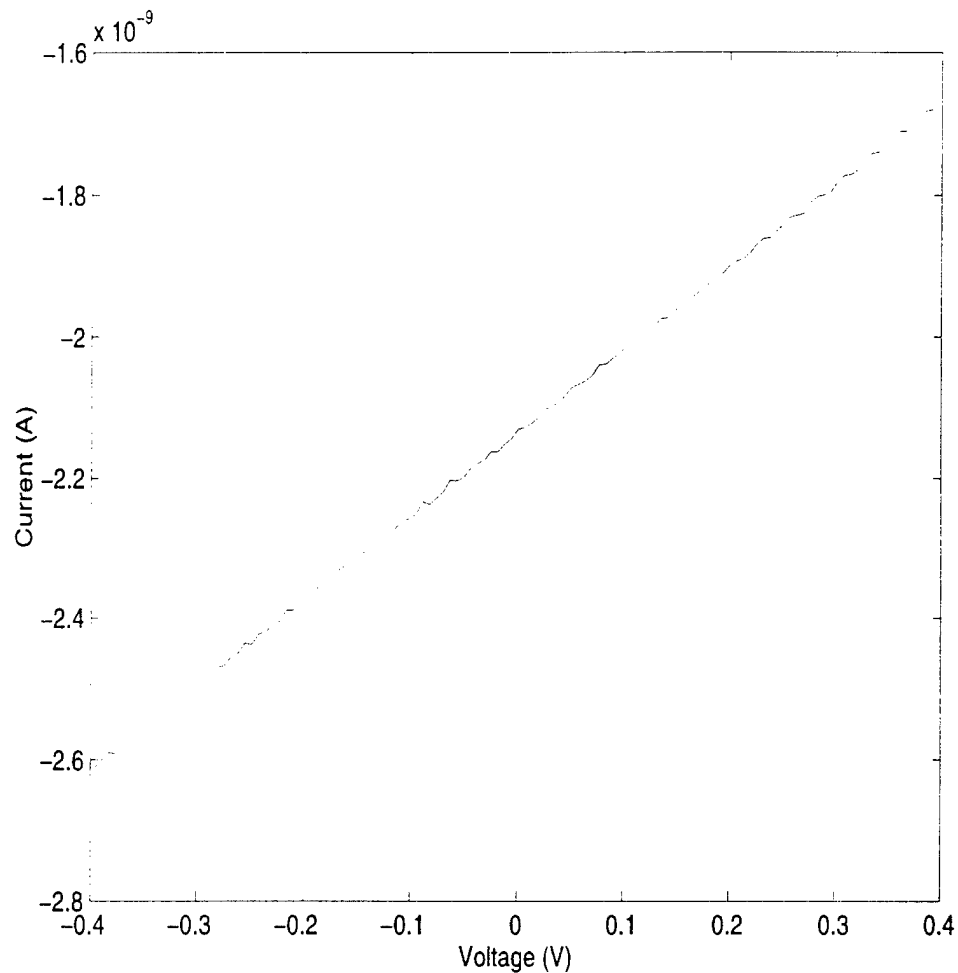


Figure 5.13: Linear conductance for a copper-iron nanoparticle at 4 K.

crucial to the success of our samples that the aluminum layer deposit as a homogenous thin film. In order to promote layer growth over island growth for the aluminum layer, we recently switched from using water to liquid N₂ to cool the sample stage during the aluminum evaporation.

Another explanation for the unsuccessful Cu-Fe samples is that our deposited aluminum layer is not too thin but too thick. An aluminum layer which is too thick will not oxidize completely. In this case, a thin layer of aluminum would connect all of the nanoparticles on the Si₃N₄ membrane. In this scenario, transport through the device would be characterized by transport, not through a single nanoparticle, but through an array of nanoparticles. Although this would not necessarily lead to a high-resistance device, it may explain the absence of Coulomb Blockade in many of

the samples.

In sum, we have found the fabrication of Cu-Fe nanoparticles to be a challenging experimental problem. There are a number of different changes we intent to make in our fabrication technique to eliminate the problems discussed in this chapter. Primarily, we believe that switching from a water cooled system to a liquid N₂ cooled system during the evaporation of the thin aluminum film will eliminate problems involving island growth of the aluminum film. We also hope to eliminate the problem of incompletely etched Si₃N₄ membranes discussed in Section 5.1 by using better focusing techniques and a resist that will allow us to use a longer reative-ion etch. At the time of this thesis, both of these ideas are being pursued.

Conclusion

This experiment represents an ideal opportunity to investigate one of the most interesting systems in nanoscale physics today: the “Kondo Box”. There are, however, a number of problems which need to be addressed before this experiment can reach its full potential.

The largest problem with this experiment has been the difficulty in imaging the nanoparticle at any of the fabrication stages. At the present time, the only method we use to gather information about the nanoparticles is to complete all of the fabrication steps described in Chapter 4 and to measure the sample’s electrical properties. This is not an ideal situation; by measuring only the “end product”, we cannot easily distinguish which of the many steps is causing problems with the devices. Ideally, we would be able to image our samples at different stages of the process. Although, for reasons related to our sample geometry, we are not able to use tunneling electron microscopy to image our completed devices, there are several possible methods we might use to gather information about our fabrication process. One is to use atomic-force microscopy to image our Si_3N_4 membranes after the reactive-ion etch. If we are able to image the 4 nm opening in the membrane, we would have a straightforward method for determining whether or not the etch was complete. Another possibility is to use scanning tunneling microscopy to image the islands that form on the Si_3N_4 membrane after the $\text{Cu}[\text{Fe}]$ deposition. By taking advantage of these techniques, we hope to gain more direct and more rapid feedback about our fabrication process.

One, more difficult, problem with this experiment is the inability to fabricate more than one sample at a time. Even if the rest of the fabrication were perfect, the formation of islands on the nitride window is a statistical process. It is necessary therefore

that many samples be processed in parallel so that statistical failure be separated out from a problem in the fabrication process. To quote from Nobel Laureate Ivar Giaever [26]

... In performing tunneling experiments the sample is the critical link. Therefore it is very important to arrange the experiments such that one can easily test many samples. Recently I tested over 50 samples in one day - and I might add that they were all bad.

There are two stages at which it is not possible, with the present system, to process many samples in parallel. The first roadblock to parallel processing is the electron-beam lithography. The system being used for this experiment cannot pattern images large enough to expose several nitride windows at one time. This requires that each nitride window be processed individually, which significantly increases the time it takes to "debug" the fabrication process. Unfortunately, there are only a few systems capable of writing on a very large area of wafer, and this particular problem is not readily solved. The second roadblock to parallel processing is the evaporation. To avoid contamination of the oxide layer, it is necessary that the entire evaporation process be done without venting the evaporation chamber to atmosphere. In order to evaporate both sides of the sample, we have machined a special stage that attaches to the end of the evaporator manipulator which allows us to evaporate on both sides of a sample with our geometry. As presently designed, this addition allows for us to evaporate on two samples at a time. It may be possible to design a system which would allow us to evaporate on more samples simultaneously although the geometry of the chamber would have to be carefully considered. Nevertheless, until it is possible to do the electron-beam lithography on an array of samples in parallel, there is no major advantage in doing so.

This system is also an excellent opportunity to investigate interimpurity interactions. In most dilute alloy studies, the interimpurity effects are discarded as negligible for an appropriately dilute alloy. It would be interesting to study how two magnetic impurities interact in a Kondo system. By controllably increasing the concentration of iron in the copper-iron alloy, we can hope to study exactly how these interimpurity interactions affect transport through the system. The concentration at which these

effects become measurable would also be another measure of the size of the Kondo “cloud” [16].

In conclusion, we have fabricated 2-3 nm aluminum nanoparticles using the system developed by Dan Ralph et. al. [3]. We have written a computer simulation to model the single electron transport through the system and we have used this simulation to understand the parameters involved in the experiment and to help in the analysis of the data. We have developed a technique for extending this fabrication method to other metal systems and hope to use this system to investigate the Kondo effect in an iron-doped copper nanoparticle, and in doing so, verify the results of Thimm et. al. [2] concerning electron transport through a “Kondo box”.

Appendix A

CALCULATION OF INTEGRAL BETWEEN EQUATIONS 2.13 AND 2.14

The integral to be calculated to get from Equation 2.13 to Equation 2.14 is

$$\int_{-\infty}^{\infty} f(\varepsilon)[1 - f(\varepsilon + x)]d\varepsilon \quad (\text{A.1})$$

where $f(\varepsilon)$ is the Fermi-Dirac distribution function given by

$$f(\varepsilon) = \frac{1}{e^{\varepsilon/k_B T} + 1}, \quad (\text{A.2})$$

T is the temperature, and k_B is the Boltzmann constant. Define $\beta = 1/k_B T$ and $x = eV$. The following relationship

$$f(\varepsilon)[1 - f(\varepsilon + x)] = \frac{f(\varepsilon) - f(\varepsilon + x)}{1 - e^{-\beta x}} \quad (\text{A.3})$$

may be derived with some manipulation and can be used to rewrite the integral in Equation A.1 as

$$\frac{1}{1 - e^{-\beta x}} \int_{-\infty}^{\infty} [f(\varepsilon) - f(\varepsilon + x)]d\varepsilon. \quad (\text{A.4})$$

Define a new function $g(x)$ to be the integrand of Equation A.4.

Since

$$\frac{dg(x)}{dx} = \frac{d}{dx} \int_{-\infty}^{\infty} [f(\varepsilon) - f(\varepsilon + x)]d\varepsilon \quad (\text{A.5})$$

$$= - \int_{-\infty}^{\infty} \frac{d}{dx} f(\varepsilon + x)d\varepsilon \quad (\text{A.6})$$

$$= - \int_{-\infty}^{\infty} \frac{\beta e^{\beta(\varepsilon+x)}}{[e^{\beta(\varepsilon+x)} + 1]^2} d\varepsilon \quad (\text{A.7})$$

$$= 1, \quad (\text{A.8})$$

$g(x)$ must equal x . Note that the initial condition $g(0) = 0$ requires the constant of integration to be zero. Equation A.4 is therefore given by

$$\frac{x}{1 - e^{-\beta x}} \quad (\text{A.9})$$

from which, substituting back in the original variables, we derive that

$$\Gamma_{1 \rightarrow 2} = \frac{4\pi}{\hbar} |T(\varepsilon)|^2 \rho_1(\varepsilon) \rho_2(\varepsilon + eV) \int_{-\infty}^{\infty} f(\varepsilon) [1 - f(\varepsilon + eV)] \quad (\text{A.10})$$

$$= \frac{4\pi}{\hbar} |T(\varepsilon)|^2 \rho_1(\varepsilon) \rho_2(\varepsilon + eV) \left[\frac{eV}{1 - e^{-eV/kT}} \right]. \quad (\text{A.11})$$

Appendix B

DERIVATION OF EIGENVALUES FOR THE ZERO-BAND WIDTH MODEL

The diagonal elements can be derived straightforwardly as follows [27]:

The two diagonal elements to be calculated can be written

$$\langle \Phi_0 | H_V | \Phi_{exc} \rangle \quad (\text{B.1})$$

and

$$\langle \Phi_{exc} | H_V | \Phi_0 \rangle. \quad (\text{B.2})$$

I will only go through the derivation for the latter element. The other element is derived in the same way. We first need to consider what results when H_V is applied to $|\Phi_0\rangle$ where

$$H_V = V_{d,\mathbf{k}} c_{d,\uparrow}^\dagger c_{\mathbf{k},\uparrow} + V_{d,\mathbf{k}}^\dagger c_{\mathbf{k},\uparrow}^\dagger c_{d,\uparrow} + V_{d,\mathbf{k}} c_{d,\downarrow}^\dagger c_{\mathbf{k},\downarrow} + V_{d,\mathbf{k}}^\dagger c_{\mathbf{k},\downarrow}^\dagger c_{d,\downarrow} \quad (\text{B.3})$$

(the first term transfers a spin $\uparrow e^-$ from the metal to the atom, the second term transfers a spin $\uparrow e^-$ from the atom to the metal, the third term transfers a spin $\downarrow e^-$ from the metal to the atom, and the fourth term transfers a $\downarrow e^-$ from the atom to the metal) and $|\Phi_0\rangle$ is the spin singlet state

$$|\Phi_0\rangle = \frac{1}{\sqrt{2}} (c_{d,\uparrow}^\dagger c_{\mathbf{k},\downarrow}^\dagger - c_{d,\downarrow}^\dagger c_{\mathbf{k},\uparrow}^\dagger) |0\rangle. \quad (\text{B.4})$$

Putting Equations B.3 and B.4 together, we get

$$H_V |\Phi_0\rangle = V (c_{d,\uparrow}^\dagger c_{\mathbf{k},\uparrow} + c_{\mathbf{k},\uparrow}^\dagger c_{d,\uparrow} + c_{d,\downarrow}^\dagger c_{\mathbf{k},\downarrow} + c_{\mathbf{k},\downarrow}^\dagger c_{d,\downarrow}) \frac{1}{\sqrt{2}} ((c_{d,\uparrow}^\dagger c_{\mathbf{k},\downarrow}^\dagger - c_{d,\downarrow}^\dagger c_{\mathbf{k},\uparrow}^\dagger) |0\rangle). \quad (\text{B.5})$$

Most of the factors drop out. Each term in H_V only acts on terms in $|\Phi_0\rangle$ with the proper spin. For example, the term $c_{\mathbf{k},\uparrow}^\dagger c_{d,\uparrow} c_{d,\downarrow}^\dagger c_{\mathbf{k},\uparrow}^\dagger$ disappears immediately because the annihilation operator $c_{d,\uparrow}$ cannot operate on the state $c_{d,\downarrow}^\dagger c_{\mathbf{k},\uparrow}^\dagger$ because the d-orbital has only electrons of spin \downarrow . On the other hand, the term $c_{\mathbf{k},\uparrow}^\dagger c_{d,\uparrow} c_{d,\uparrow}^\dagger c_{\mathbf{k},\downarrow}^\dagger |0\rangle = c_{\mathbf{k},\uparrow}^\dagger c_{\mathbf{k},\downarrow}^\dagger |0\rangle$. Each term that would put two electrons on the d-orbital (such as $c_{d,\uparrow}^\dagger c_{\mathbf{k},\uparrow} c_{d,\uparrow}^\dagger c_{\mathbf{k},\downarrow}^\dagger$) have also been dropped because we are taking the $U \rightarrow \infty$ limit.

After some manipulation, we get

$$H_V |\Phi_0\rangle = \frac{V}{\sqrt{2}} (c_{\mathbf{k},\uparrow}^\dagger c_{\mathbf{k},\downarrow}^\dagger - c_{\mathbf{k},\downarrow}^\dagger c_{\mathbf{k},\uparrow}^\dagger) |0\rangle. \quad (\text{B.6})$$

This equation is greatly simplified when we recognize that

$$|\Phi_{exc}\rangle = c_{\mathbf{k},\uparrow}^\dagger c_{\mathbf{k},\downarrow}^\dagger \quad (\text{B.7})$$

and use the anticommutation relationship satisfied by the creation operators

$$[c_{\mathbf{k},\uparrow}^\dagger c_{\mathbf{k},\downarrow}^\dagger, c_{\mathbf{k},\downarrow}^\dagger c_{\mathbf{k},\uparrow}^\dagger]_+ = 0. \quad (\text{B.8})$$

Using relationship B.8 to switch the sign in Equation B.6 and plugging in the definition of the excited state B.7 yields

$$H_V |\Phi_0\rangle = \sqrt{2}V |\Phi_{exc}\rangle. \quad (\text{B.9})$$

Finally, it can be seen that

$$\langle \Phi_{exc} | H_V | \Phi_0 \rangle = \sqrt{2}V. \quad (\text{B.10})$$

Now that we understand where the matrix elements in Equation 2.37 come from, we can proceed to find the eigenvalues [28]. We start with the matrix 2.37

$$\begin{bmatrix} \epsilon_d + \epsilon_{\mathbf{k}} & V\sqrt{2} \\ V\sqrt{2} & 2\epsilon_{\mathbf{k}} \end{bmatrix} \quad (\text{B.11})$$

subtract the eigenvalues from the diagonals and set the determinant to 0

$$\begin{vmatrix} \epsilon_d + \epsilon_{\mathbf{k}} - \lambda & V\sqrt{2} \\ V\sqrt{2} & 2\epsilon_{\mathbf{k}} - \lambda \end{vmatrix} = 0 \quad (\text{B.12})$$

$$(\epsilon_d + \epsilon_{\mathbf{k}} - \lambda)(2\epsilon_{\mathbf{k}} - \lambda) - 2V^2 = 0. \quad (\text{B.13})$$

This yields a quadratic equation in λ

$$\lambda^2 - (3\epsilon_{\mathbf{k}} + \epsilon_d)\lambda + 2\epsilon_{\mathbf{k}}(\epsilon_d + \epsilon_{\mathbf{k}}) - 2V^2 = 0. \quad (\text{B.14})$$

Solving this quadratic equation yields the two eigenvalues we wish to calculate:

$$\lambda_1 = 2\epsilon_{\mathbf{k}} + \frac{2V^2}{\Delta\epsilon} \quad (\text{B.15})$$

$$\lambda_2 = \epsilon_{\mathbf{k}} + \epsilon_d - \frac{2V^2}{\Delta\epsilon} \quad (\text{B.16})$$

where $\Delta\epsilon = \epsilon_{\mathbf{k}} - \epsilon_d$.

Appendix C

COMPUTER SIMULATION CODE

This computer simulation calculates (with no approximations) the linear conductance $I(V)$ for the nanoparticle devices explored in this thesis. The nanoparticle parameters discussed in Chapter 3, C_1 , C_2 , R_1 , R_2 , and T , are modified in the program body. When the program is run, the user will be asked to input the voltage range (in mV) and the step size (in mV) for the simulation.

```
#include <stdio.h>
#include <float.h>
#include <math.h>
#define elec 1.6e-19 /*electron charge*/
#define k_B 1.38e-23 /*Boltzmann constant*/
#define epsilon_0 8.85e-12 /*permittivity of free space*/
#define pi 3.14159

void InitializeArrays(double array[]);

void CalculateE_plus_1(double E_plus_1[], float C_2, float C_tot,
    float V, float E_C, float Q_0, int n, int sign);
void CalculateE_minus_1(double E_minus_1[], float C_2, float C_tot,
    float V, float E_C, float Q_0, int n, int sign);
void CalculateE_plus_2(double E_plus_2[], float C_1, float C_tot,
    float V, float E_C, float Q_0, int n, int sign);
void CalculateE_minus_2(double E_minus_2[], float C_1, float C_tot,
    float V, float E_C, float Q_0, int n, int sign);

void CalculateTunnelOn_1(double tunnel_on_1[], double E_plus_1[],
    float R_1, float T, int n);
void CalculateTunnelOff_1(double tunnel_off_1[], double E_minus_1[],
    float R_1, float T, int n);
void CalculateTunnelOn_2(double tunnel_on_2[], double E_plus_1[],
```

```

        float R_2, float T, int n);
void CalculateTunnelOff_2(double tunnel_off_2[], double E_minus_1[],
        float R_2, float T, int n);

void CalculateSigma(double A[], double sigma[], int n, double factor[]);

main()
{
    /* C_1 and C_2 are the capacitances of the two tunnel junctions;
    R_1 and R_2 are the resistances of the two tunnel junctions;
    Q_0 is the offset charge on the particle, radius is the radius of the particle,
    T is the temperature that the simulation is being run at,
    V_min and V_max are the limits for the simulation and V_step is the step size;
    I is the current obtained for each voltage */

    float C_1, C_2, R_1, R_2, Q_0, radius, T, E_C, C_tot, C_self, V_min, V_max,
        V_step, V_min2, V_max2, V_step2, sigma_n_max;
    double I, sigmasum;

    double E_plus_1[50]; /*define arrays to hold all values used to calculate I */
    double E_minus_1[50]; /*array must be larger than largest n in calculation */
    double E_plus_2[50];
    double E_minus_2[50];

    double tunnel_on_1[50];
    double tunnel_off_1[50];
    double tunnel_on_2[50];
    double tunnel_off_2[50];

    double A[50];
    double sigma[50];
    double factor[50];

    float k; /*main loop variable*/
    double sum;
    double CurrentSum;
    double double_n;
    int n, z, h, l;
    int sign;
    double temp, temp2;

    FILE *smltn; /*pointer to simulation file*/

    printf("\nV_min (in mV) = ");
    scanf("%f", &V_min2);

```

```

printf("\nV_max (in mV) = ");
scanf("%f", &V_max2);
printf("\nV_step (in mV) = ");
scanf("%f", &V_step2);

V_min = V_min2/1000;    /* converts input in mV to V */
V_max = V_max2/1000;
V_step = V_step2/1000;

/* input for the simulation below*/

C_1 = 1e-18;           /* capacitance of lead 1 */
C_2 = 3e-18;           /* capacitance of lead 2 */
R_1 = 10e6;            /* resistance of lead 1 */
R_2 = 100e6;           /* resistance of lead 2 */
Q_0 = 0.0*elec;        /* offset charge on the nanoparticle */
radius = 2.4e-9;       /* radius of the nanoparticle - DOES NOT GET USED IN SIMULATION */
T = 4.2;               /* temperature */

C_self = (elec*elec)/(8*pi*epsilon_0*radius); /*self-capacitance of the particle*/

C_tot = C_1+C_2;                /*sum of the two tunnel capacitances*/

E_C = (elec*elec)/(2*C_tot);     /*electrostatic charging energy*/

/* *****main loop***** */

smltn = fopen("I.dat","w");
for (k=V_min; k < V_max; k = k + V_step)
{
    if (k<=0)
    {
        double_n = (1/elec)*((C_2*k) + Q_0 - (elec/2));
        /* calculates the number of extra electrons on the nanoparticle */

        temp = double_n;           /* gets only the integer part of n*/
        n = temp-1;
        printf("\n n = %d", n);

        sign = -1;
    }
    else
    {

```

```

double_n = (1/elec)*((C_2*k) - Q_0 + (elec/2));
/* calculates the number of extra electrons on the nanoparticle */

temp = double_n;          /* gets only the integer part of n*/
n = temp+1;
printf("\n n = %d", n);

sign = +1;
}

sigma_n_max = 0.0;
sum = 0.0;

InitializeArrays(E_plus_1);
InitializeArrays(E_minus_1);
InitializeArrays(E_plus_2);
InitializeArrays(E_minus_2);

InitializeArrays(tunnel_on_1); /*initializes all arrays back to zero*/
InitializeArrays(tunnel_off_1);
InitializeArrays(tunnel_on_2);
InitializeArrays(tunnel_off_2);

InitializeArrays(A);
InitializeArrays(sigma);

CalculateE_plus_1(E_plus_1, C_2, C_tot, k, E_C, Q_0, n, sign);
CalculateE_minus_1(E_minus_1, C_2, C_tot, k, E_C, Q_0, n, sign);
CalculateE_plus_2(E_plus_2, C_1, C_tot, k, E_C, Q_0, n, sign);
CalculateE_minus_2(E_minus_2, C_1, C_tot, k, E_C, Q_0, n, sign);

CalculateTunnelOn_1(tunnel_on_1, E_plus_1, R_1, T, n);
CalculateTunnelOff_1(tunnel_off_1, E_minus_1, R_1, T, n);
CalculateTunnelOn_2(tunnel_on_2, E_plus_2, R_2, T, n);
CalculateTunnelOff_2(tunnel_off_2, E_minus_2, R_2, T, n);

A[0] = 1;

if (k<=0)
{
for (z = 1; z < (abs(n)+1); z++)          /* ratio of tunneling rates */
{
factor[z] = (tunnel_off_1[z-1]+tunnel_off_2[z-1])/(tunnel_on_1[z]+tunnel_on_2[z])
}
}

```



```

}

if (k>0)
{
for (z = 1; z < (n+1); z++)          /* ratio of tunneling rates */
{
factor[z] = (tunnel_on_1[z-1]+tunnel_on_2[z-1])/(tunnel_off_2[z]+tunnel_off_1[z])
}
}

for (z=1; z < (abs(n)+1) ; z++)
{
/* calculates the fraction A that relates sigma[n] and sigma[n-1] */

A[z] = A[z-1]*factor[z];
}

for (z=0; z < (abs(n)+1) ; z++)
{
sum = sum + A[z];          /* sums all the fractions for normalization */
}

sigma[0] = 1/sum;

CalculateSigma(A, sigma, n, factor);
/* with sigma[0] calculates all probabilities sigma*/

sigmasum = 0.0;

for (l = 0; l<(abs(n)+1); l++)
{
sigmasum = sigmasum + sigma[l];
}

CurrentSum = 0.0;

for (l = 0; l<(abs(n)+1); l++)
/* sums all occupation probabilities multiplied by tunneling rates */
{
CurrentSum = CurrentSum + sigma[l]*(tunnel_off_2[l]-tunnel_on_2[l]);
}

```

```

        I = elec*CurrentSum;                /* calculates I */

        fprintf(smltn,"%f  %E\n", k, I);
    }
fclose(smltn);
}
/* *****end of main loop***** */
/* *****Initialize Arrays***** */

void InitializeArrays(double array[])
{
    int i;

    for (i = 0; i < 50; i++) /* initializes all arrays to 0.0 */
        array[i] = 0.0;

}

/* *****end of InitializeArrays***** */
/* ***** CalculateE_plus_1 ***** */

void CalculateE_plus_1(double E_plus_1[], float C_2, float C_tot,
                      float V, float E_C, float Q_0, int n, int sign)
{
    int j;
    for (j = 0; j < (abs(n)+1); j++) /* energy to add electron through lead 1 */
    {
        E_plus_1[j] = -elec*(C_2/C_tot)*V + E_C*((2*sign*j)+1+2*(Q_0/elec));
    }

}

/* ***** end of CalculateE_plus_1 ***** */
/* ***** CalculateE_minus_1 ***** */

void CalculateE_minus_1(double E_minus_1[], float C_2, float C_tot,
                      float V, float E_C, float Q_0, int n, int sign)
{
    int j;

    for (j = 0; j < (abs(n)+1); j++) /* energy to subtract electron through lead 1 */
    {
        E_minus_1[j] = elec*(C_2/C_tot)*V + E_C*((-2*sign*j)+1-2*(Q_0/elec));
    }
}

```

```

    }

}

/* ***** end of CalculateE_minus_1 ***** */
/* ***** CalculateE_plus_2 ***** */

void CalculateE_plus_2(double E_plus_2[], float C_1, float C_tot,
    float V, float E_C, float Q_0, int n, int sign)
{
    int j;

    for (j = 0; j < (abs(n)+1); j++) /* energy to add electron through lead 2 */
    {
        E_plus_2[j] = elec*(C_1/C_tot)*V + E_C*((+2*sign*j)+1+2*(Q_0/elec));
    }

}

/* ***** end of CalculateE_plus_2 ***** */
/* ***** CalculateE_minus_2 ***** */

void CalculateE_minus_2(double E_minus_2[], float C_1, float C_tot,
    float V, float E_C, float Q_0, int n, int sign)
{
    int j;

    for (j = 0; j < (abs(n)+1) ; j++) /* energy to subtract electron through lead 2 */
    {
        E_minus_2[j] = -elec*(C_1/C_tot)*V + E_C*((-2*sign*j)+1-2*(Q_0/elec));
    }

}

/* ***** end of CalculateE_minus_2 ***** */
/* ***** CalculateTunnelOn_1 ***** */

void CalculateTunnelOn_1(double tunnel_on_1[], double E_plus_1[],
    float R_1, float T, int n)
{

```

```

int j;

for (j = 0; j < (abs(n)+1); j++)          /* tunneling rate on through lead 1 */
{
    tunnel_on_1[j] = (1/(elec*elec*R_1))*(-E_plus_1[j]/(1-exp(E_plus_1[j]/(k_B*T))));
}

}

/* *****end of CalculateTunnelOn_1***** */
/* *****CalculateTunnelOff_1 ***** */

void CalculateTunnelOff_1(double tunnel_off_1[], double E_minus_1[],
    float R_1, float T, int n)
{
    int j;

    for (j = 0; j < (abs(n)+1) ; j++)      /* tunneling rate off through lead 1 */
    {
        tunnel_off_1[j] = (1/(elec*elec*R_1))*(-E_minus_1[j]/(1-exp(E_minus_1[j]/(k_B*T))));
    }
}

/* *****end of CalculateTunnelOff_1***** */
/* *****CalculateTunnelOn_2 ***** */

void CalculateTunnelOn_2(double tunnel_on_2[], double E_plus_2[],
    float R_2, float T, int n)
{
    int j;

    for (j = 0; j < (abs(n)+1); j++)        /* tunneling rate on through lead 2 */
    {
        tunnel_on_2[j] = (1/(elec*elec*R_2))*(-E_plus_2[j]/(1-exp(E_plus_2[j]/(k_B*T))));
    }
}

/* *****end of CalculateTunnelOn_2***** */
/* *****CalculateTunnelOff_2 ***** */

void CalculateTunnelOff_2(double tunnel_off_2[], double E_minus_2[],
    float R_2, float T, int n)
{

```

```

int j;

for (j = 0; j < (abs(n)+1) ; j++)      /* tunneling rate off through lead 2 */
{
    tunnel_off_2[j] = (1/(elec*elec*R_2))*(-E_minus_2[j]/(1-exp(E_minus_2[j]/(k_B*T))));
}
}

/* *****end of CalculateTunnelOff_2***** */
/* ***** CalculateSigma ***** */

void CalculateSigma(double A[], double sigma[], int n, double factor[])
{

int h;

for (h = 1; h < (abs(n)+1) ; h++)
{
    sigma[h] = sigma[h-1]*factor[h];    /* calculates probability of occupation sigma */
}

}

/* ***** end of CalculateSigma ***** */

```

Appendix D

FABRICATION RECIPES

FABRICATION OF Si_3N_4 MEMBRANE WINDOWS

1. Take a Si wafer with 50 nm LPCVD Si_3N_4 on both sides and deposit 50 nm layer of Si_3N_4 on the “window” side of the wafer. This layer will protect the Si_3N_4 membrane during photolithography and will be etched completely away in the KOH.
2. Spin AZ 3318 photoresist at 4000 rpm for 30 s.
3. Bake for 1 min at 90° C.
4. Expose for 2 min.
5. Bake for 1 min at 110° C.
6. Develop with MF300 developer (full strength) for 2 min.
7. 13 min RIE etch (O_2 at 0.50 SCCM, CHF_3 at 36.0 SCCM, pressure 40 mT) to remove the native oxide layer on the silicon wafer.
8. Etch wafer in a 30% (by weight) solution of KOH at 80-85°. To ensure a constant, homogenous KOH solution, cover beaker to reduce evaporation and periodically remove wafer and stir solution. The etch is very sensitive to KOH concentration and hotplate temperature and can take anywhere from 2-5 hours to complete.

FABRICATION OF Si_3N_4 MEMBRANE WINDOWS

1. On the “window” side of the silicon wafer, spin PMMA/MMA 10% by weight electron-beam lithography resist at 3000 rpm for 45 sec.
2. Bake for 2 hrs at 180° C.
3. On the same side, spin 1.5% 950K PMMA electron-beam lithography resist at 7000 rpm for 30 sec.

4. Bake for 2 hrs at 180° C.
5. Carefully break apart the grid of windows into individual units. Care should be taken not to touch the Si_3N_4 windows themselves as they can easily break.
6. Using electron-beam lithography on each unit separately, expose the Si_3N_4 window to a single pixel dot pattern.
7. Develop with MIBK/IPA for 1 min.
8. Stop development by dunking in IPA for 15 s.
9. Carefully dry window with N_2 .
10. 12 min RIE (same parameters as above) etch.
11. Insert sample into evaporator for thermal evaporation. The sample must not be exposed to atmosphere between any of the evaporations. It is therefore necessary that the sample holder be designed to allow for evaporation on both sides of the sample.
12. Deposit $\sim 1000 \text{ \AA}$ of pure Al onto the "bowl" side of the wafer, i.e. the first layer of Al must fill the bowl etched in the window during the 12 min RIE etch in Step 10.
13. Oxidize sample using 50 mT of O_2 for 2 min.
14. Flip sample in chamber and evaporate $\sim 20 \text{ \AA}$ of the 0.01% Fe in Cu alloy.
15. Deposit $\sim 15 \text{ \AA}$ of Al.
16. Oxidize sample using 50 mT of O_2 for 2 min.
17. Deposit a final layer of $\sim 1000 \text{ \AA}$ of Al.

Bibliography

- [1] D.V. Averin and K.K. Likharev. Single electronics. In B.L. Al'tshuler, P.A. Lee, and R.A. Webb, editors, *Mesoscopic Phenomena in Solids*. Elsevier, 1991.
- [2] Wolfgang B. Thimm, Jahann Kroha, and Jan von Delft. Kondo box: A magnetic impurity in an ultrasmall metallic grain. *Physical Review Letters*, 82(10), 1999.
- [3] D. C. Ralph. C. T. Black, and M. Tinkham. Spectroscopic measurements of discrete electronic states in single metal particles. *Physical Review Letters*, 74(16), 1995.
- [4] D. C. Ralph. C. T. Black, and M. Tinkham. Gate-voltage studies of discrete electronic states in aluminum nanoparticles. *Physical Review Letters*, 78(21), 1997.
- [5] S. Gueron, Mandar M. Deshmukh, E.B. Myers, and D.C. Ralph. Tunneling via individual electronic states in ferromagnetic nanoparticles. *Physical Review Letters*, 83(20), 1999.
- [6] Fabian Braun, Jan von Delft, D.C. Ralph, and M. Tinkham. Paramagnetic breakdown of superconductivity in ultrasmall metallic grains. *Physical Review Letters*, 79(5), 1997.
- [7] C.T. Black, D.C. Ralph, and M. Tinkham. Superconducting gap in individual nanometer-scale aluminum nanoparticles. *Physical Review Letters*, 76(4), 1996.
- [8] D. G. Salinas, S. Gueron, D. C. Ralph, C. T. Black, and M. Tinkham. Effects of spin-orbit interactions on tunneling via discrete energy levels in metal nanoparticles. *Physical Review B*, 60(8), 1999.
- [9] Jun Kondo. Resistive minimum in dilute magnetic alloys. *Progress of Theoretical Physics*, 32(1):37, 1964.
- [10] P.W. Anderson. Localized magnetic states in metals. *Physical Review*, 124(1):41, 1961.
- [11] Gert-Ludwig Ingold and Yu. V. Nazarov. *Single Charge Tunneling*, chapter 2. Plenum Press, 1992.

- [12] Hermann Grabert and Michel H. Devoret, editors. *Single Charge Tunneling*. Plenum Press, 1991.
- [13] A.C. Hewson. *The Kondo Problem to Heavy Fermions*. Cambridge University Press, 1993.
- [14] Charles Black. *Tunneling Spectroscopy of Nanometer-Scale Metal Particles*. PhD thesis, Harvard University, 1996.
- [15] Peter Fulde. *Electron Correlations in Molecules and Solids*. Springer-Verlag, 1991.
- [16] V. Madhavan, W. Chen, T. Jamneala, M. F. Crommie, and N. S. Wingreen. Tunneling into a single magnetic atom: Spectroscopic evidence of the kondo resonance. *Science*, 280:567, 1998.
- [17] George T. Rado and Harry Suhl, editors. *Magnetism*. Academic Press, 1973.
- [18] A. E. Hanna and M. Tinkham. Variation of the coulomb staircase in a two-junction system by fractional electron charge. *Physical Review B*, 44(11), 1991.
- [19] Richard W. Vook. Theories of nucleation and growth of thin films. In William R. Hunter, editor, *Thin Film Technologies and Special Applications*. SPIE - The International Society for Optical Engineering, 1982.
- [20] Aicha A. R. Elshabini-Riad and Fred D. Barlow. *Thin Film Technology Handbook*. McGraw Hill, 1997.
- [21] Neil W. Ashcroft and N. David Mermin. *Solid State Physics*. Harcourt Brace College Publishers, 1976.
- [22] Richard Zallen. *The Physics of Amorphous Solids*. John Wiley and Sons, 1983.
- [23] Dan Ralph. personal correspondence.
- [24] N.F. Mott. *Philosophical Magazine*, 19(2), 1969.
- [25] Robert F. Pierret. *Semiconductor Device Fundamentals*. Addison-Wesley, 1996.
- [26] E. Burnstein and S. Lundquist, editors. *Tunneling Phenomena in Solids*. Plenum Press, 1969.
- [27] Chad Sosolik. personal correspondence.
- [28] Chad E. Sosolik. The classical kondo effect and the kondo effect in atom-surface scattering. Master's thesis, Cornell University, 1998.